Centre for Geo-Information

Thesis Report GIRS-2009-17

MONITORING VEGETATION STRUCTURE IN A RIVER FLOODPLAIN ECOSYSTEM USING MULTI-ANGULAR CHRIS-PROBA DATA

Erika Romijn

September 2009

WAGENINGEN UNIVERSITY
WAGENINGEN UR

Photo on front page: river floodplain area of Millingerwaard during the winter of 2008/2009.
(photography: Erika Romijn)

Monitoring vegetation structure in a river floodplain ecosystem using multi-angular CHRIS-PROBA data

J.E. (Erika) Romijn

Registration number 80 04 30 703 020

Supervisors:

dr. ir. Lammert Kooistra
ir. Jochem Verrelst

A thesis submitted in partial fulfilment of the degree of Master of Science
at Wageningen University and Research Centre,
The Netherlands.

September, 2009
Wageningen, The Netherlands

Thesis code number: GRS-80436
Thesis Report: GIRS-2009-17
Wageningen University and Research Centre
Laboratory of Geo-Information Science and Remote Sensing

Foreword

I have learned a lot during the thesis process, both about the research topic and about how to work independently on a big research project. In the beginning I did not really know where to start and how to handle the topic. I started out with literature research and bit by bit it became clear what is common knowledge in the remote sensing research world. In this way I got some ideas of how to work on the thesis research. I have studied about river floodplain ecosystems and management, classification processes and different remote sensing models, in particular the model FLIGHT. I have learned how to model the vegetation and how this vegetation can be simplified into a few structure properties. The research has taken more time than initially planned, but I have been able to fulfil all the research objectives. I enjoyed working on the research and I am very happy with the final results.

Acknowledgements

I could not have done this thesis research without the help and support of many people.
First of all, I would like to thank my supervisors Lammert Kooistra and Jochem Verrelst. Lammert Kooistra, for his guidance through the whole thesis process and for keeping an eye on the overall planning. He was very fast in giving comprehensive feedback on my work and gave many ideas on how to improve the research and the report. Jochem Verrelst, for helping me with the FLIGHT modelling process and for his patience explaining it to me. I was completely blank on this topic and I learned really much about how to work with Linux, python scripts, IDL scripts and MySQL. It is great that he took the time to create a new model inversion script for the purpose of my research. The long discussions with both of my supervisors were very interesting and gave me many new ideas for my research. They were always very enthusiastic and provided me with up to date information and new articles. I would like to thank Willy ten Haaf and Antoinette Stoffers for the organizational part of the last MGI (master Geo-Information Science) year.
Furthermore, I want to thank the students in the thesis room for creating a nice working atmosphere, supporting each other and having nice (table tennis) breaks. Many thanks to my tennis friends from “Walhalla”, the tennis club where I spent a lot of my free time during the thesis. I needed this to compensate for the long working days behind the computer! I would like to thank my corridor mates for listening to whatever was on my mind about my thesis progress. And last but not least, I would like to thank my family and friends for their moral support during the whole thesis process.

Abstract

To safeguard rivers from flooding, river floodplains in the Netherlands have been enlarged to accommodate the water discharge. Many floodplains however are also developed for nature rehabilitation, resulting in natural processes of vegetation succession. Remote sensing is seen as an important tool to map and monitor the vegetation structure in order to provide river managers with up-to-date information on hydraulic roughness of the vegetation.
The objective of this study was to develop a methodology for monitoring the location and structure properties of vegetation structure types in a river floodplain ecosystem using multi-directional hyperspectral data. In this study data were used from the CHRIS sensor onboard the PROBA satellite acquired in 2005 over the test site Millingerwaard, a river floodplain ecosystem along the river Waal in the Netherlands. CHRIS data are particularly suitable for mapping vegetation structure because of its high spatial resolution (~17m*17m), spectral coverage (18 bands from 400 nm to 1050 nm) and angular sampling (5 viewing angles).
First, the CHRIS images were classified into eight major land use classes, using different classification techniques. Best results were obtained from the CHRIS nadir classification, using the maximum likelihood classifier and multiple angular images for determining the regions of interest.
After classification, relevant vegetation structure properties such as leaf area index (LAI) and fractional cover (fCover) were quantified on a pixel-by-pixel basis by using the canopy reflectance model FLIGHT. FLIGHT is a physical based radiative transfer model that simulates canopy bidirectional reflectance by using Monte Carlo ray tracing. LAI and fCover maps were computed through model inversion of the CHRIS data for the three main classified vegetation structure types "herbaceous", "shrubs" and "forest". All three vegetation classes were modelled as a 1D turbid medium, the forest class was additionally modelled with explicit 3D canopy geometry. The outcomes were validated with in situ LAI and fCover measurements that were collected using hemispherical photography and TRAC measurements.
Although physically simplified, the 1D modelling approach provided superior results compared to the 3D approach, probably due to the less extensive parameterization process. LAI and fCover maps were computed for the CHRIS viewing angles in nadir direction, backscattering direction (view zenith angle of -36°) and forward scattering direction (view zenith angle of +36°). The backscattering direction gave the best results, and showed most variation in LAI and fCover values. Further research is needed in order to find out if the inferred vegetation structure maps can be related to hydraulic roughness values and thereby provide relevant information to river managers.

Keywords: *CHRIS/PROBA, multi-angular, vegetation structure types, maximum likelihood (ML) classification, Leaf area index (LAI), fractional cover (fCover), radiative transfer (RT) model, FLIGHT*

Table of contents

List of figures

List of tables

Abbreviations

ASCII	American Standard Code for Information Interchange
ASD Fieldspec FR	Analytical Spectral Device Field Spectrometer Full Range
AVNIR	Advanced Visible and Near Infrared Radiometer
BRDF	Bi-directional Reflectance Distribution Function
BRF	Bi-directional Reflectance Factor
CASI	Compact Airborne Spectrographic Imager
CFR	Cyclic Floodplain Rejuvenation
CHRIS	Compact High-Resolution Imaging Spectrometer
Db	Database
ENVI	ENvironment for Visualizing Images
ESA	European Space Agency
fAPAR	Fraction of Absorbed Photosynthetic Radiation
fCover	Fractional cover
FLIGHT model	Forest LIGHT interaction model
FR	Forest
GCP	Ground Control Point
GH	Grasses and Herbs
GIS	Geo-Information Science / Geographic Information System
GO model	Geometrical-Optical model
HCRF	Hemispherical-Conical reflectance Factor
HDRF	Hemispherical-Directional Reflactance Factor
HDS	Hotspot-Darkspot index
IDL	Interactive Data Language
LAD	Leaf angle distribution
LAI	Leaf Area Index
LiDAR	LIght Detection And Ranging
LUT	LookUp Table
MC	Monte Carlo
ML	Maximum Likelihood
MODIS	Moderate Resolution Imaging Spectroradiometer
NDVI	Normalized Difference Vegetation Index
NIR	Near InfraRed
NPP	Net Primary Production
PCA	Principal Component Analysis
PROBA(-1)	Project for On-Board Autonomy
PV	fraction of Photosynthetic Vegetation
RBG	Red Blue Green
RD new	Rijksdriehoekstelsel
RMSE	Root Mean Square Error
ROI	Region Of Interest
RS	Remote Sensing
RT models	Radiative Transfer models
RWS	Rijkswaterstaat
SGM	Simple Geometric Model
SH	Shrubs
SLC model	Soil-Leaf-Canopy model
SQL	Structured Query Language
SVM	Support Vector Machine
TOC	Top-Of-Canopy
TRAC	Tracing Radiation and Architecture of Canopies
UTM	Universal Transverse Mercator
VI	Vegetation Index
VIS	Visible
VZA	View Zenith Angle
WDVI	Weighted Difference Vegetation Index
WGS 1984	World Grid System 84

1. Introduction

1.1 Background

Perhaps even in the Netherlands few people realise that about 65% of the Dutch land area would be submerged by sea or river water, if all dikes were removed. Dike building started in the Middle Ages in the Dutch Delta which was drowned gradually under influence of a relative rise of the mean sea level. The relative mean sea level rise amounted during the last centuries to 10-15 cm per century. Moreover, the land surface subsided locally due to compaction of peat and clay layers, caused by drainage, making dike building even more important to keep dry feat (Van de Ven, 1993). Each century, catastrophic floods damaged sea and river dikes several times, the last being the storm surge of 1953 in the Southwest part of the Netherlands. After each event dikes were rebuilt and strengthened, but after the flood of 1953, the Dutch Deltaplan was set up, which aimed at reaching a much higher protection against flooding. The coastal zones were protected by shortening of the coastline from 1300 to 600 km and heightening of the sea dikes with 1.5 to 2 m, thus realising a lower flooding risk of only 1% per century (Van de Ven, 1993; Groen & Schmeink, 1981). For rivers, the Delta plan aimed at a flooding risk of 3% per century for the 800 km of river dikes, with a design peak flow of 18.000 m^3/s. But this was eventually lowered to 8% per century, with a design peak flow of 16.500 m^3/s at Lobith (Groen & Schmeink, 1981).

The Rhine is a highly managed river system in the Netherlands. During the 18th, 19th and 20th century, regulation, normalization and canalization measures have been implemented to improve both discharge and navigation of the river. These measures, together with the agricultural development in the floodplains caused the Rhine to loose its natural meanders and parts of its floodplain system (Van de Ven, 1993; Groen & Schmeink, 1981).
The near-floods of the river Rhine in 1993 and 1995 reactivated river dike building. At the same time, global warming was recognized as a main problem, with its influence on sea level change and rainfall (IPCC, 2007). Recent climate studies show that the temperature in the Netherlands will increase during the 21st century. Also, a rise of 35-85 cm of the absolute mean sea level in 2100 compared to 1990 is expected, which means that river water levels will also rise. In winter, precipitation will increase in Northern Europe leading to higher peak flows in the Rhine. These effects lead to an increased flood risk for the floodplains and its hinterland (KNMI, 2006; Ministerie van V&W, 2005). In 2007 the Dutch government decided to follow a complete new approach to river management, called "Space for the River" (PKB "Ruimte voor de Rivier"; Ministerie van V&W 2005; 2007). *The Netherlands will suit itself more to the water instead of the other way around.* Giving the river more space involves besides diminishing flood risks, multidisciplinary spatial planning in which economic, landscape and ecological values will be improved, with special attention to nature conservation and development (Ministerie van V&W, 2007). Space for peak flows is sought in creating a larger water discharge capacity by widening and deepening the river beds and not in heightening the dikes even more.

1.2 Problem definition

The Millingerwaard is a river floodplain ecosystem next to the river Waal near Nijmegen where nature development has taken place on former agricultural land. The Millingerwaard is one of the places where space for the river is created for extra water storage in times of high water level in the river (Ministerie van V&W, 2007). This means that when the water discharge of the river is high, the water surplus will flow into the side channels and river floodplains of Millingerwaard. Since Millingerwaard is part of a nature rehabilitation project where spontaneous vegetation development occurs in this ecosystem, natural succession has taken place and softwood forests have developed. Softwood (e.g. willow) trees however, with their broad structure (figure 1), and other vegetation types hamper the river discharge. This vegetation causes resistance to the water flow through the floodplain ("Nederland Leeft met Water", 2008). Moreover, floods cause sedimentation processes, especially in softwood forests. This accumulation of material decreases the flood flow velocities

and increases the water surface (Geerling et al., 2008). Monitoring of these river floodplains is necessary to see how vegetation develops in the different floodplain ecotopes. In case there is too much vegetation that causes problems for water discharge, river managers have to take adequate measures by removing this vegetation.

To intervene with the spontaneous vegetation growth, Cyclic Floodplain Rejuvenation (CFR; Duel et al. 2001, cited in Geerling et al., 2008) has been introduced for the Rhine river systems. It implies periodic artificial disturbance of the floodplain ecosystems, like removal of climax vegetation. Pioneer stages reappear and ecological succession starts again. In order to know where to remove this climax vegetation, data about the distribution of vegetation stages and the magnitude of resistance it causes to the water flow are needed. Accurate monitoring of location and structure properties of different vegetation structure types is important information for river managers with respect to river flooding. For this purpose Rijkswaterstaat (RWS) has made an ecotope classification for the Rhine system. It is part of the biological monitoring of the Dutch fresh waters (Rijkswaterstaat, 2008-2), a commitment for the European programme "Kaderrichtlijn Water". The ecotope map is the starting point for hydraulic calculations. It is used to derive water resistance values of the vegetation in a floodplain with high water levels.
The process of creating the ecotope classification took three years. The first classification was ready in 1997 and the second in 2008. In future RWS strives to make the classification every 6 years. It is a very time-consuming and expensive way of monitoring the Dutch river and floodplain ecosystems. The +/- 70 classified RWS ecotopes are more or less homogeneous ecological units of which the composition is determined by geomorfological, hydrological, vegetation, land use and anthropogenic aspects. First, digital false colour aerial photographs are made. Then the photographs are interpreted and ecotopes (polygons and lines) are determined. With an overlay procedure using GIS software the ecotopes are combined with data on flood duration, management, water depth and morfodynamics. The outcome is a rough ecotope file. After translating it into standards the final ecotope map is created. This combination of methods causes some problems and uncertainties in the ecotope maps. First, the overlay procedures generated a (too) large amount of small areas. Those areas had to be re-distributed to the adjacent areas, which is a cause of uncertainty. It offers a very detailed classification, but for determining ecotopes that are relevant for flooding, so much detail is probably not needed. A validation of the RWS ecotope map was made in the field, but the amount of field samples was not large enough to be able to make statistical judgements with enough confidence. For a good quality of the ecotope maps more validations still have to be done. Furthermore there are geometric and thematic uncertainties in the maps. The overall thematic accuracy of the classification is 71%. The rough areas and bushes scored relatively low with respectively 65% and 46% of accuracy (Rijkswaterstaat, 2008-2). Those two ecotopes are very important to map for flooding events, because they have a large influence on the water flow (Geerling et al., 2008). And finally, there is no information on spatial variability (e.g. information on structure properties) within the units.

Remote sensing gives the opportunity to observe the earth from a distance and to obtain information about an object or an area by means of a sensor on board of a satellite or airplane. This makes large scale data acquisitions possible and therefore remote sensing is a promising tool to monitor vegetation development and vegetation structure because it can cover a large area and methods can be automated (Lillesand et al., 2004).

Figure 1: Willow trees next to the river Waal in Millingerwaard (photography: Erika Romijn)

Remote sensing is a promising tool for monitoring floodplain vegetation development. When remote sensing can be used to monitor the vegetation structure types of river floodplains and their structure properties, it could be a fast and cheap method for monitoring, compared to the traditional monitoring of RWS. From just one remote sensing image the necessary data can be derived and no overlay procedures, which are a cause for uncertainty, have to be done. However, there is spatial heterogeneity in river floodplains and this requires detailed spectral information to distinguish different vegetation structure types from each other. Also, mixing of different vegetation structure types within a pixel can be a problem. Apart from the location of the vegetation structure types, quantitative structure properties like leaf area index (LAI) and fractional cover (fCover) within these units are of importance for river managers. They show the variability within ecological units and indicate the places with the highest accumulation of biomass, which cause resistance for the water in flooding events. LAI is an important structure property of the vegetation, because by using photosynthesis models an estimation of the net primary production (NPP) and vegetation biomass can be derived from it (Kooistra et al., 2008). If a model could be developed with the remote sensing image as input and the variability of the vegetation structure as output, than monitoring becomes an automated process.
Multi-angular data give the opportunity to observe the land surface under different angles. This can have an added value compared to one-directional remote sensing images or aerial photographs. They only give a view on the top of the canopy. This makes it difficult to distinguish for example bushes from trees. Multi-angular data could have an improvement for this aspect, because a combination of images under different angles can give information on the woody parts of the vegetation, which can only be observed under an angle. Nevertheless, not much research has been done so far to prove that multi-angular data are appropriate for this purpose. It has been argued that multi-angular data can be used for mapping vegetation structure properties (see paragraph 2.3.3 & 2.3.4). Radiative transfer models, geometric optical models and ray-tracing models are often used to estimate vegetation properties.

1.3 Research objectives and research questions

The objective of this research is to develop a methodology for monitoring the location and structure properties of vegetation structure types in a river floodplain ecosystem using multi-angular hyperspectral CHRIS-PROBA data.

Research questions

1. How can different vegetation structure types in a river floodplain ecosystem be classified using multi-angular CHRIS-PROBA imagery?
2. How can the canopy structure properties leaf area index, fractional cover and fraction of photosynthetic vegetation (LAI, fCover and PV) be derived from multi-angular CHRIS-PROBA data using the radiative transfer, monte carlo ray tracing model FLIGHT (North, 1996)?
3. Are results still accurate when the methods from the first 2 questions are extrapolated to a larger floodplain area, namely from Millingerwaard to the complete area of the Gelderse Poort?

1.4 Report outline

The next chapter consists of literature review on the main topics of this research: river floodplain ecosystem management, monitoring of vegetation structure properties, remote sensing models for monitoring the vegetation structure and the scope of this research. Chapter three comprises information about the study site and data, and the methodology that is followed for this thesis research. In chapter four the results are presented. In chapter five these results are discussed with respect to the research objective and research questions, and in the light of the theoretical framework, using scientific literature. Chapter six contains the conclusions and recommendations for further research on the topic.

2. Literature review

2.1 Dutch river floodplain ecosystems

Natural river systems

Natural river systems in the lower part of Northern Europe are not fixed to one place, but are moving freely through the landscape. Erosion and sedimentation processes remove sand from one side of the riverbanks and deposit it on the other side. This creates circumstances for rejuvenation of the vegetation. The river system in Biebrza National Park in Poland is an example of a natural river system (Bierbza National Park, 2008). In the Netherlands such natural river systems do not occur any more. Dutch rivers are regulated for shipping and river management purposes. The required measures have resulted in rivers that are not meandering any more; bends are cut off and rivers have a fixed streambed.

Increasing flood risk

The consequences of the regulation measures are that aquatic and floodplain ecology deteriorated and floodplain areas became smaller. Regulation also increased the flood risk in Dutch rivers, such as the Rhine system (Ministerie van V&W, 2005). Other human interventions like the construction of dams, drainage systems, and changes in land use such as deforestation also have an impact on the water cycle and water discharge, thereby contributing to the flood risk of rivers (Chuvieco, 2008). In a more general context, humans contribute to the continuing increase in greenhouse gases in the atmosphere which have an impact on the global climate system and consequently on the hydrological cycle (IPCC, 2007). Especially in parts of the world where climate became warmer, the thermodynamic effects changed the hydrological cycle. As a result glaciers are shrinking and snow starts melting earlier and more intensive during winter and spring. This together with prolonged rainstorms and heavy thunderstorms are some of the causes that create risks of flooding. The west and the north of the Netherlands are especially vulnerable for flooding events because of the rise in sea level, while the east and south of the Netherlands can be in danger because of large amounts of water discharge in the rivers (Rijkswaterstaat, 2008-1). For this century a rise in river water discharge of approximately 3.000 m^3/s for the Rhine near Lobith, resulting in peak flows up to 18.000 m^3/s, and a rise in mean sea level of approximately 60 cm are expected. Two major events which happened in the Rhine system in 1993 and 1995 showed that the river system did not have enough capacity to accommodate all the water (Geerling et al., 2008). Protection against flooding is therefore a very important issue in the Netherlands. The Dutch government and river management organizations are working hard on solving future water surplus problems.

Dutch policy and management of river floodplain ecosystems

Rijkswaterstaat (RWS) is the Dutch organisation that implements the policy of the ministry for traffic and public works department (Ministerie van Verkeer en Waterstaat). Their goals are, amongst others, to ensure smooth and safe traffic over roads and waterways; to provide enough and clean water; to provide reliable and usable information; and to prevent rivers, lakes, channels and the sea from flooding. RWS carries out the plans of the Dutch government on water management.
The Dutch government has published a statutory report in which they decide to anticipate on the consequences of climate change and the imminent high water levels by giving Dutch rivers more space (Ministerie van V&W, 2005). A few zones are selected for expansion of the rivers. The plan aims at guaranteeing safety for the inhabitants and improving the spatial quality of the river-areas. Conservation and development of landscape, ecological, geophysical and cultural values are important. As a first step the Dutch government has determined an amount of measures for river restoration which should be met before 1015. In some areas the measures will go together with nature development plans. The plans involved the creation of side-channels, lowering levees and restoring nature. In many cases this means that agricultural land will be altered into nature areas for water storage and nature development. Ecological succession takes place in these newly developed nature areas. However, this results in an increase in biomass which means that there is less water storage capacity available in case of flooding. The woody vegetation biomass hampers the river

discharge and smooth storage of water. Because of this, a new management strategy was adopted: Cyclic Floodplain Rejuvenation (Duel et al. 2001, cited in Geerling et al., 2008). This involves periodic removal of climax vegetation, in order to keep nature areas in a pioneer stage with continuous ecological succession (Geerling et al., 2008). In this way, complex vegetation structures that cause the most hydraulic resistance are being kept out of the floodplain ecosystems.

2.2 Monitoring of vegetation structure

Hydraulic resistance of vegetation has a large influence on the maximum water discharge capacity. Therefore, monitoring of river floodplain ecosystems is necessary in order to receive up-to-date information about vegetation structure and development in floodplains. River managers need these data to be able to reach the goals of flood protection and nature development. Monitoring vegetation development can be done by field work, but this is very laborious.

Another option is to use remote sensing data to make classifications of different vegetation structure types. These classifications can be made each year with an automated monitoring process of vegetation development. Verrelst et al. (2009) used spectral data from Compact Airborne Spectrographic Imager (CASI) and structural information from LiDAR (LIght Detection And Ranging) to create vegetation classes for the Dutch floodplain area Millingerwaard. Spectral signatures (the characteristic reflection of radiation obtained by remote sensing techniques) of vegetation types were combined with structural characteristics from LiDAR (vegetation height) to get the necessary information for the vegetation classes. Figure 2 shows different vegetation structure types that are present in Millingerwaard.

However, mapping plant communities into different small vegetation classes (like the Braun-Blanquet system) is difficult when using remote sensing techniques. Spectral signatures of narrow defined plant communities can look very similar. Verrelst et al. (2009) demonstrated that clustering the vegetation types into combined classes, higher on the hierarchic scale of Braun-Blanquet, hereby discriminating in elevation and soil moisture parameters, gives superior results. When this segmentation technique is automated, monitoring of vegetation types can be easily done.

Vegetation structure properties that can be derived from remote sensing data are leaf area index (LAI), fraction of photosynthetic fraction (PV), crown diameter and fractional cover (fCover). These properties can function as measures for the amount of woody vegetation or biomass in a pixel, which causes resistance to the water flow in case of flooding events. LAI is a measure for the structure within one tree. It is the total of one-sided area of photosynthetic tissue (green leaves) per area (m^2/m^2) (Jonckheere et al., 2004). It is an important property, because by using photosynthesis models an estimation of the net primary production (NPP) and vegetation biomass can be derived from it (Kooistra et al., 2008). Leaf angle distribution (LAD) and leaf clumping effects are factors that influence the LAI outcome. They can both lead to errors of up to 50% in LAI determination (Roujean and Lacaze, 2002). Fractional cover (fCover) is much less sensitive to clumping effects. fCover indicates the fraction of a pixel that is covered by vegetation and thus it specifies the horizontal extent of vegetation (Roujean and Lacaze, 2002). PV is a measure for the total amount (volume-fraction) of green vegetation within the vegetation. The other fraction is the non-photosynthetic, woody, vegetation.

Figure 2: Different vegetation structure types in Millingerwaard (photography: Erika Romijn)

2.3 Remote sensing models for monitoring of vegetation structure and development

2.3.1 Radiative transfer models

Radiative transfer models (RT models) are physical based models that aim at understanding the interaction (reflection, transmission and absorption) between solar radiation and vegetation properties. RT models describe the transfer and interactions of solar radiation inside the canopy based on physical laws and thus provide an explicit connection between the chemical and physical characteristics of vegetation elements and the canopy reflection. The basis for these models is the bi-directional reflectance distribution function (BRDF) which calculates the reflection of an object.
PROSPECT is a RT model that simulates spectral reflectance and transmittance from leaf properties of a plant at leaf level (Jacquemoud & Baret, 1990). PROSPECT idealizes the leaf as a pile of elementary plates composed of absorbing and diffusing constituents. It is based on the plate model of Allen, et al. (1969) where the leaf has a structure of plates and voids. PROSPECT adds parameters to the plate model such as water content, chlorophyll content and number of leaf layers. It contains an incidence angle and a transmission coefficient. By model inversion leaf characteristics can be estimated.

The simulated leaf reflectance and transmittance output of PROSPECT can be used as input for the SAIL model that simulates canopy reflectance as a function of canopy parameters (Verhoef, 1984). Apart from the optical properties of a single leaf, the leaf area index (LAI) and the leaf inclination distribution are input for the SAIL model. This means that LAI can be obtained by model inversion. Some variations of SAIL are SAILH, SAIL++ and 4-SAIL. The combination of PROSPECT and SAIL is called ProSail. There are some extensions on the PROSPECT and SAIL model. There is the model GeoSail (Huemmrich, 2001) which is the SAIL model combined with the Jasinski geometric model. It simulates canopy spectral reflectance and fraction of absorbed photosynthetically active radiation (f_{APAR}) for discontinuous canopies. Cylinders and cones describe the different tree shapes. The model consists of three components: illuminated canopy, illuminated background and shadowed background. The coupled model PROSPECT & SAILH uses two approaches for simulating the BRDF (D'Urso et al., 2004). With LookUp Tables (LUT) the spectral profile is generated for each combination of canopy parameters. And using the PEST ASP Tool (non-linear parameter estimation software) the optimized parameters are determined according to a pre-defined cost-function. D'Urso et al. (2004) use the model to asses the capability to estimate LAI from CHRIS data for alfalfa and potato crops. Another model is the coupled PROSPECT & SAILH & CLAIR model (Vuolo et al., 2005). This is a simple empirical model coupled with a RT model. The semi-empirical relationship between WDVI (Weighted Differences Vegetation Index) and LAI is used as a priori information to get initial parameters for the model.

2.3.2 Definitions of reflectance quantities

"Natural irradiance is composed of a direct component (non-scattered radiation) and a diffuse component scattered by the atmosphere (gases, aerosols, and clouds), and the surroundings of the observed surface" (Schaepman-Strub et al., 2006).
The conceptual quantities that are derived by RT modelling are defined by the BRDF. The bidirectional reflectance factor (BRF) can not be measured. It is a theoretical concept and includes only direct irradiance of incident light from one direction in the hemisphere that is scattered into another direction in the hemisphere.
Measurable quantities include irradiance from the entire hemisphere. They include pure diffuse or a combination of direct and diffuse irradiance. This concept is called the Hemispherical-Directional Reflactance Factor (HDRF) (Schaepman-Strub et al., 2006). The measured values of the CHRIS sensor in this study can be approximated by HDRF values, but these are also theoretical reflectance values.

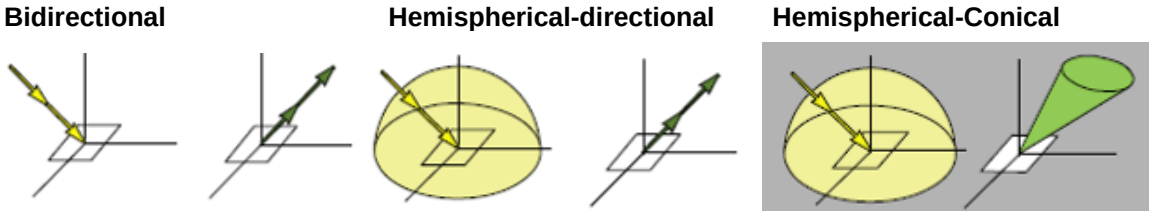

Figure 3: On the left side: the bidirectional reflectance (a directional incoming beam and a directional reflected beam), in the middle: hemispherical-directional reflectance (hemispherical incoming radiance and a directional reflected beam), on the right side: hemispherical-conical reflectance (hemispherical incoming radiance and conical reflected radiance) souce: Schaepman-Strub et al., 2006.

In fact, CHRIS measurements are Hemispherical-Conical reflectance Factor (HCRF) measurements, because the observation of the satellite includes, apart from the direct measured reflected radiance beam also some diffuse components. This means that CHRIS measurements are not exactly the same as modelled bidirectional reflectance quantities, but approximate the BRF. These concepts are made clear in figure 3.

2.3.3 Added value of using multi-angular CHRIS-PROBA data

Multi-angular data give the opportunity to simultaneously observe the land surface under different angles. This can have an added value compared to one-directional remotely sensed data which only give a view on the top of the canopy (nadir view). Multi-angular data can improve on this aspect, because a combination of images under different angles provides information on the woody parts of the vegetation, which can only be seen under angles which differ from nadir. Therefore, multi-angular measurements could improve the classification of different vegetation types and the estimation of vegetation structure properties. The use of different configurations of multi-spectral, multi-angular and multi-temporal measurements can provide a better discrimination between vegetation classes. Duca and Del Frate (2008) improved their classification accuracy with 7% with the use of +36 and -36 VZA (View Zenith Angle) images next to the nadir VZA image. Chuma (2008) explored the usefulness of different angles and vegetation indices of multi-angular CHRIS-PROBA data for classification of heathland habitat types. He concluded that certain bands and indices with combined multi-angular data (especially -36 VZA and -55 VZA) can be useful for vegetation classification.

The rich content of multi-angular imagery provides information on how structure impacts the portioning of solar energy between vegetation canopy and the underlying surface. This facilitates ecological issues and improves the use of physical modelling. It increases the accuracy of the information content. LAI and f_{APAR} (fraction of absorbed photosynthetic radiation) are measures for vegetation canopy structure and its energy absorption capacity. Estimates of LAI and f_{APAR} can be improved by the use of multi-angular data, because it accounts for vegetation structure characteristics that have an impact on the angular reflectance (Diner et al., 1999; Diner et al., 2005).

Crown clumping

Off-nadir view angles of CHRIS data could help to improve the LAI estimation because it can account for clumping effects. The clumping effect is a measure for the amount of leaves that are clustered together. This alternates the top-of-canopy (TOC) reflectance signal. Clumping effects are mostly present in nadir views (Koetz et al., 2007). When leaves are more clumped the amount of sunlit leaves decreases and the amount of shaded leaves increases. This changes the final model outcome of canopy photosynthesis and therewith the estimate of NPP. So, the clumping index elucidates the differences of vegetation canopies with a different architecture.

2.3.4 RT Models using multi-angular data

Verhoef and Bach (2007) used a coupled soil-leaf-canopy model (SLC) to derive LAI from TOC reflectance. It consists of the Hapke soil BRDF model, which is a combination of a soil and Prospect model, and the 4Sail2 model, which incorporates crown clumping. The model accommodates vertical heterogeneities (leaf colour gradients) and horizontal heterogeneities related to crown clumping.
Chen et al. (2003) also incorporated clumping index into a sunlit/shaded leaf model. They used the effective LAI, which is a product of LAI and the clumping index. The clumping index can be linearly related to the Hotspot-Darkspot index (HDS), using values from the BRDF curve. In the BRDF curve the reflectance in a spectral band is plotted against the scattering angle (the difference between the sun angle and the view angle to the ground target). The series of equations used to derive the effective LAI are:

$$\Omega = a + b*HDS \quad (1)$$

$$HDS = (\rho_{HS} - \rho_{DS}) / (\rho_{DS}) \quad (2)$$

$$\text{Effective LAI} = LAI * \Omega \quad (3)$$

Ω	= clumping index
a & b	= coefficients determined by linear regression
HDS	= Hotspot-Darkspot index
ρ_{HS}	= reflectance at hotspot
ρ_{DS}	= reflectance at darkspot
Effective LAI	= effective leaf area index
LAI	= leaf area index

There are also other models than RT models that can use multi-angular data. An example is the geometrical-optical model (GO model). The SGM (non-linear simple geometric model) was inverted against multi-angle reflectance data from CHRIS-PROBA (Chopping et al., 2006). This model can be used to estimate woody shrub abundance by separating background and upper canopy contributions. The first attempts with this method were promising. However, the method was tested in a semi-arid environment and not in a floodplain ecosystem. The vegetation differs much in those two environments and this could affect the results when trying this method for a floodplain ecosystem. The separation of background and upper canopy contributions might already cause difficulties, because there is a lot of understory in a river floodplain ecosystem.

2.3.5 PROFLIGHT

FLIGHT

Another RT modelling approach is the ray-tracing approach. These models follow the propagation of rays of light and how they interact with optical surfaces. FLIGHT (North, 1996) is a hybrid three dimensional ray tracing model based on Monte Carlo (MC) simulations of photon transport. The model is hybrid because of the combination of a GO model and a RT model. MC simulations are flexible and give the opportunity for accurate canopy representations. However, it has a large processing time for simulation. FLIGHT is accurate in accounting for forest dynamics, almost on a photon-by-photon basis. FLIGHT models the vegetation as a complex structure, which is represented by geometric primitives defined by crown shape and size, tree height, position and distribution, as in figure 4.

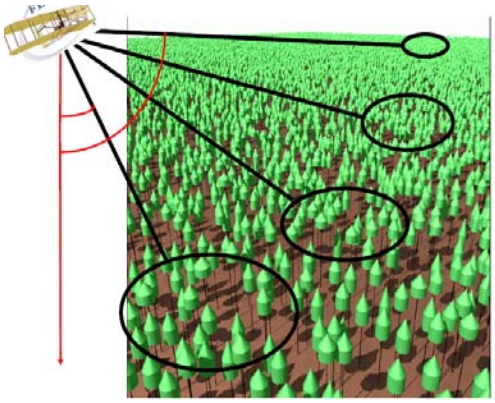

Figure 4: 3D canopy representation of a FLIGHT forest scene

The model incorporates shadowing effect, crown overlapping and multiple scattering between crowns. The model outcomes are TOC BRF values.
FLIGHT simulates photon trajectories, starting from a solar source, through successive interactions with the vegetation, to a predetermined sensor view angle. The model incorporates the probability of free path, absorption and scattering. Within the crown, photons are scattered based on probability density functions. The individual photons are followed until they are either absorbed or exited by the canopy. The model outcome is the result of a unique stand configuration, solar illumination direction (Θs,Φs), surface reflection direction (Θr,Φr) and spectral wavelength (λ).
There is also a 1D mode available in which the vegetation is modelled as turbid medium. This turbid medium can be seen as a canopy layer that contains a mix of different elements that represent the vegetation structure characteristics.

PROFLIGHT
PROFLIGHT is a coupled RT model of PROSPECT and FLIGHT (Verrelst et al., 2008). Verrelst et al. (2008) applied PROFLIGHT to assess the underlying driving factors governing angular signatures. Both foliage optical properties and woody optical properties are needed as model input. Foliage optical properties were modelled by PROSPECT and coupled with FLIGHT. FLIGHT parameterization for woody parts and understory was done with field measurements taken in a test forest. FLIGHT simulations showed that the structural variability (variations in woody and foliage parts) is important for explaining the angular signatures.

In another study the model PROFLIGHT was used to assess the effects of woody elements on forest canopy chlorophyll content retrieval (Verrelst et al., 2009 (unpublished work)). The contribution of crown wood cover, crown LAI and crown coverage on the chlorophyll content retrieval was assessed on the basis of modelled reflectance BRF data. The data that were needed to parameterize the model PROFLIGHT were foliage parameters for PROSPECT, canopy structure parameters and optical properties of background, bark and foliage for FLIGHT (Koetz et al., 2004; Verrelst et al., 2008). In order to reduce processing time a LUT approach was used and processing parallelization was implemented.

The PROSPECT part was parameterized on:
- chlorophyll content
- dry matter content
- leaf water content
- effective nr. of leaf layers.

The output reflectance and transmittance of foliage from PROSPECT were used as input foliage spectra for FLIGHT. For the FLIGHT simulations parameters from a field campaign were used to fill the LUT. The model was run by sending one million rays in an experimental canopy.

2.4 The scope of this research

Since the launch of the PROBA satellite in 2001 (Barnsley et al., 2004) not much has been reported in literature on making classifications using multi-angular CHRIS data. Huber (2008) made use of support vector machines (SVMs) to classify multi-angular and hyperspectral CHRIS images. SVMs produced better results than the traditional methods using the maximum likelihood (ML) classifier (Huber, 2008). Both methods will be explored in this thesis research.

A quantitative, physical based RT model with 3D canopy architecture provides the most logical linkage between the physics and biochemicals of canopy features and satellite observations. Therefore, the model PROFLIGHT seems to be very suitable for exploring the added value of multi-angular CHRIS data to monitor vegetation structure properties. Multi-angular data can be used in the model and the model contains structural parameters, which can be derived by model inversion. Furthermore, the implementation of the model has been developed in the RS/GIS department of Wageningen University so there is experience and expertise with the model. For this research, only the FLIGHT part of the model will be used, because leaf reflectance and transmittance data are already available from a field campaign and earlier studies in Millingerwaard (Liras, 2005).

3. Materials & Methods

3.1 Study site

The methods in this thesis research have been developed for Millingerwaard and the Gelderse Poort, a nature reserve located in the east of the Netherlands with a surface area of 6700 ha. The Gelderse Poort consists of several connected nature areas. One of them is Millingerwaard, a river floodplain ecosystem of 700 hectares near Nijmegen next to the Waal, the main branch of the river Rhine in the Netherlands (figure 5). Several remote sensing and field datasets have been obtained for Millingerwaard as it is an extensively studied area.

In the last decades Millingerwaard has undergone different measures for river and nature restoration. In former times Millingerwaard used to be a floodplain area with a river and some side streams meandering in-between sand dunes. Softwood forest grew on the river banks. In later centuries the forests were logged and clay was dug from pits. In the 20th century, Millingerwaard was formed into an agricultural area with intensively managed grassland and maize. During the 1980's this came to an end when the project called "Plan Ooievaar" (the Black stork plan) started (De Bruin et al., 1987). Spontaneous nature development played a central role in this project. By digging out clay, following the relief, the old pattern of side streams, natural levees and isles returned. Agricultural land has been restored into its former state of natural vegetation. Right now the nature development in Millingerwaard sets an example for the rest of the country.

Millingerwaard consists of sandy river dunes with natural grassland, old river streams, clay pits with swamps and softwood forest. Konik horses and Galloway cows have been introduced for natural grazing. They prune and trim plants and trees, manure the area, create paths and make the landscape more varied with a mosaic of grass lands, roughs, bushes and woods. The vegetation is very divers with more than 250 different species occurring on soils ranging from dry and nutrient poor to moist and rich of nutrients. It provides a habitat for fauna like red deer, roe deer, mice, birds and insects. Also beavers have been introduced into the swampy area. They eat bark, gnaw branches and create open spots in the softwood forest. Their population is quite stable (ARK Natuurontwikkeling, 2008).

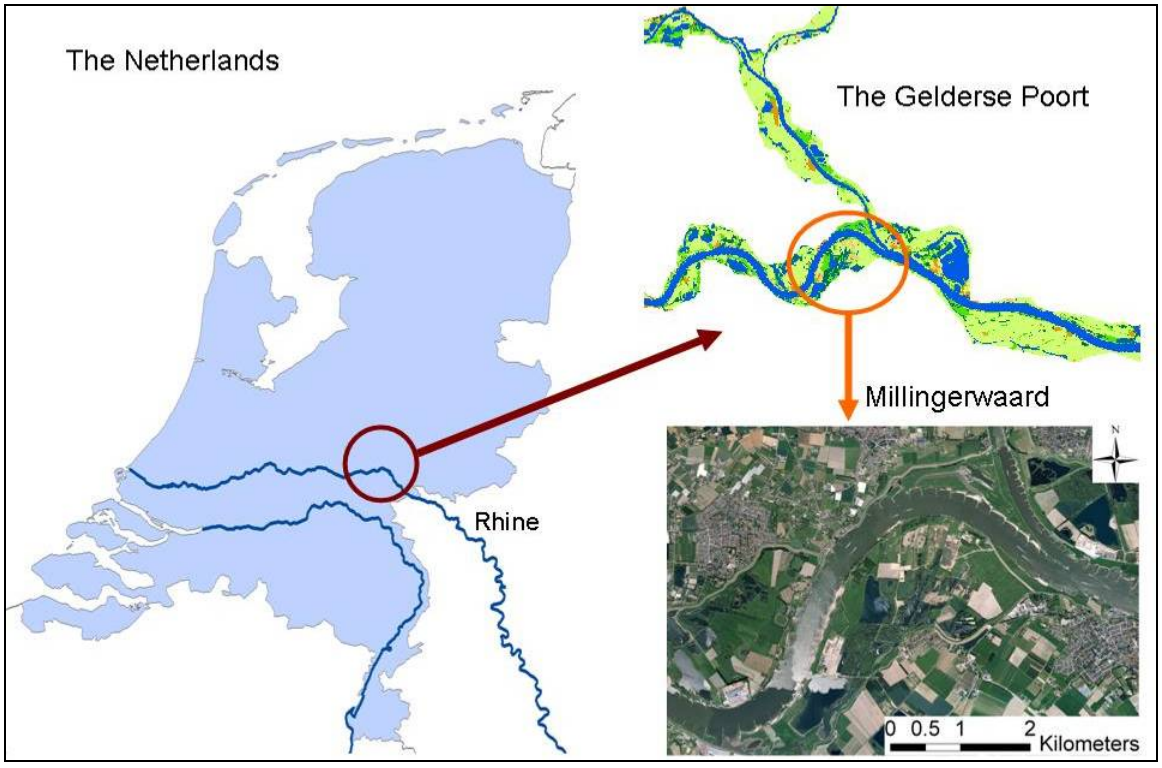

Figure 5: Location of the study site Gelderse Poort & Millingerwaard

Figure 6: Excavations to create more space for the river in Millingerwaard (photography: Erika Romijn)

The Dutch government has set up a project for this floodplain area to create more space for the rivers and to reduce the risk of flooding (Ministerie van V&W, 2005). For Millingerwaard, the project aims at reducing the water level with 9 cm. Excavations and lowering of the floodplains are planned and implemented (figure 6). This includes digging side river streams for permanent water storage and lowering dams and riverside walls (Ministerie van V&W, 2007) to create an overflow area when water levels are high. The river is given an open connection with the floodplains.

While Millingerwaard is still a nature development area, the problem occurs that spontaneous vegetation growth hampers the water discharge of the river. Measures, like CFR (chapter 2), are taken to create more space for the water to flow (ARK Natuurontwikkeling, 2008).

3.2 Data

Multi-angular CHRIS-PROBA data (2005)

The most important data that are used for this research are multi-angular data from the CHRIS (Compact High-Resolution Imaging Spectrometer) sensor, onboard of the PROBA-1 (Project for On-Board Autonomy) satellite. The PROBA-1 satellite was launched on October 22, 2001 in India. PROBA-1 is a demonstration satellite of the European Space Agency (ESA) on which ESA performs tests to investigate if satellite missions can be more autonomous, without interference of a ground station. There is one ground segment with many automated functions. The PROBA-1 was initially a one year mission, but the satellite is still active at the moment. The satellite has a polar, sun synchronous orbit and operates on a height of 553-676 km.

CHRIS is the main earth imaging payload for land areas on board of the PROBA-1. CHRIS is a hyperspectral, multidirectional sensor with a spectral range of 415-1050 nm in the visible (VIS) and near infrared (NIR) part of the electromagnetic spectrum. It can measure spectral reflectance from 5 different viewing angles: 0˚, +/-36˚ and +/-55˚. Further in the text they will be referred as: VZA (viewing zenith angle), for example: nadir VZA, -36 VZA. VZA -36 and -55 are defined as backscattering direction, VZA +36 and +55 as forward scattering direction. It has 5 different modes in which it can measure water bodies, land surfaces and atmospheric aerosols and chlorophyll. In this study mode 3 is used. This mode is intended for land surface and atmospheric aerosols and has a spatial resolution of approximately 17m*17m at nadir VZA (Barnsley et al 2004; European space agency, 2008). In mode 3 CHRIS has a spectral resolution of 5-12 nm and measures in 18 bands. Apart from the multi-angular aspect of the data, the advantage of using CHRIS data is that CHRIS has a large ground coverage of one image, compared to other imaging spectrometers like HyMap. The multi-angular CHRIS images used for this study were acquired on 6 September 2005. They contain the Millingerwaard and part of the Gelderse Poort.

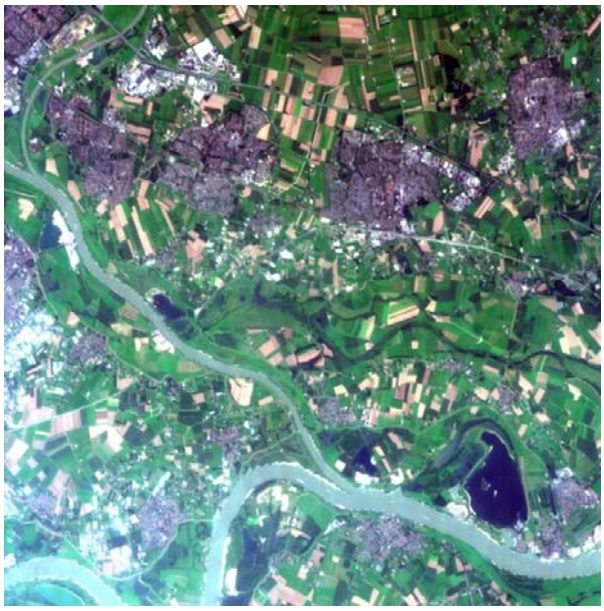

Figure 7: RBG-composition (bands 2,4,8) of CHRIS nadir image of the Gelderse Poort

Figure 7 shows the CHRIS nadir image after atmospheric correction. Appendix I contains more information about the PROBA satellite, the CHRIS sensor and image acquisition.

RWS ecotope map (2005)

RWS has made an ecotope classification for the Rhine system to be used for biological monitoring of the Dutch fresh waters (Rijkswaterstaat, 2008-2). This monitoring is a commitment for the European Water Framework Directive. The classified ecotopes are more or less homogeneous ecological units of which the composition is determined by geomorfological, hydrological, vegetation, land use and anthropogenic aspects. RWS started in 2005 with making digital, false colour, aerial photographs. In 2006, an interpretation of the photographs was made and ecotopes (polygons and lines) were determined. In the same year a field validation was made. In 2007 RWS made an overlay procedure using GIS software in which they combined the ecotopes with data on flooding duration, management, water depth and morfodynamics. The outcome was a rough ecotope file. After translating it into standards the final ecotope map was created. The ecotope map is amongst others the starting point for hydraulic calculations.

Field data

Reflectance data of leaves were collected during a field campaign in August 2004 using an ASD Fieldspec FR (field spectrometer). The processed data from this campaign from *Calamagrostis epigejos, Salix alba* and *Rubus caesius* (Liras, 2005) were used for this thesis research. Additional reflectance data from different bark and background types were obtained during the thesis work on the 2nd of April 2009 using the ASD FieldSpec FR. These reflectance data are used for the modelling part of the research.

Other datasets

Reference datasets:

- Aerial photograph of the Gelderse Poort (2006)
- Topographic data of the Gelderse Poort: 1:250.000 & 1:10.000 (2006)

Datasets for validation

- LAI field data of Millingerwaard, obtained with a combined methodology of hemispherical photography and TRAC measurements in 2005 (Gonsamo, 2006).
- LAI field data of Millingerwaard, obtained in 2004 with the hemispherical camera (Mengesha, 2005).
- fCover field data of Millingerwaard, obtained in 2004 with the hemispherical camera (Mengesha, 2005).

3.3 Methodology

3.3.1 Overview

Figure 8 shows the overall flowchart of the thesis research. It gives a simplified overview of the complete methodology that was followed. In short, the first part of the research deals with making the classification, based on multi-angular CHRIS images. This part is explained in detail in paragraph 3.3.3. The second part comprises running the model FLIGHT to derive LAI, fCover and PV maps, based on the previously derived CHRIS classification and the multi-angular CHRIS images and is explained in paragraph 3.3.4. First, in paragraph 3.3.2 the pre-processing methods are described. Thereafter, in paragraph 3.3.3 and 3.3.4 the detailed flowcharts with explanations are given.

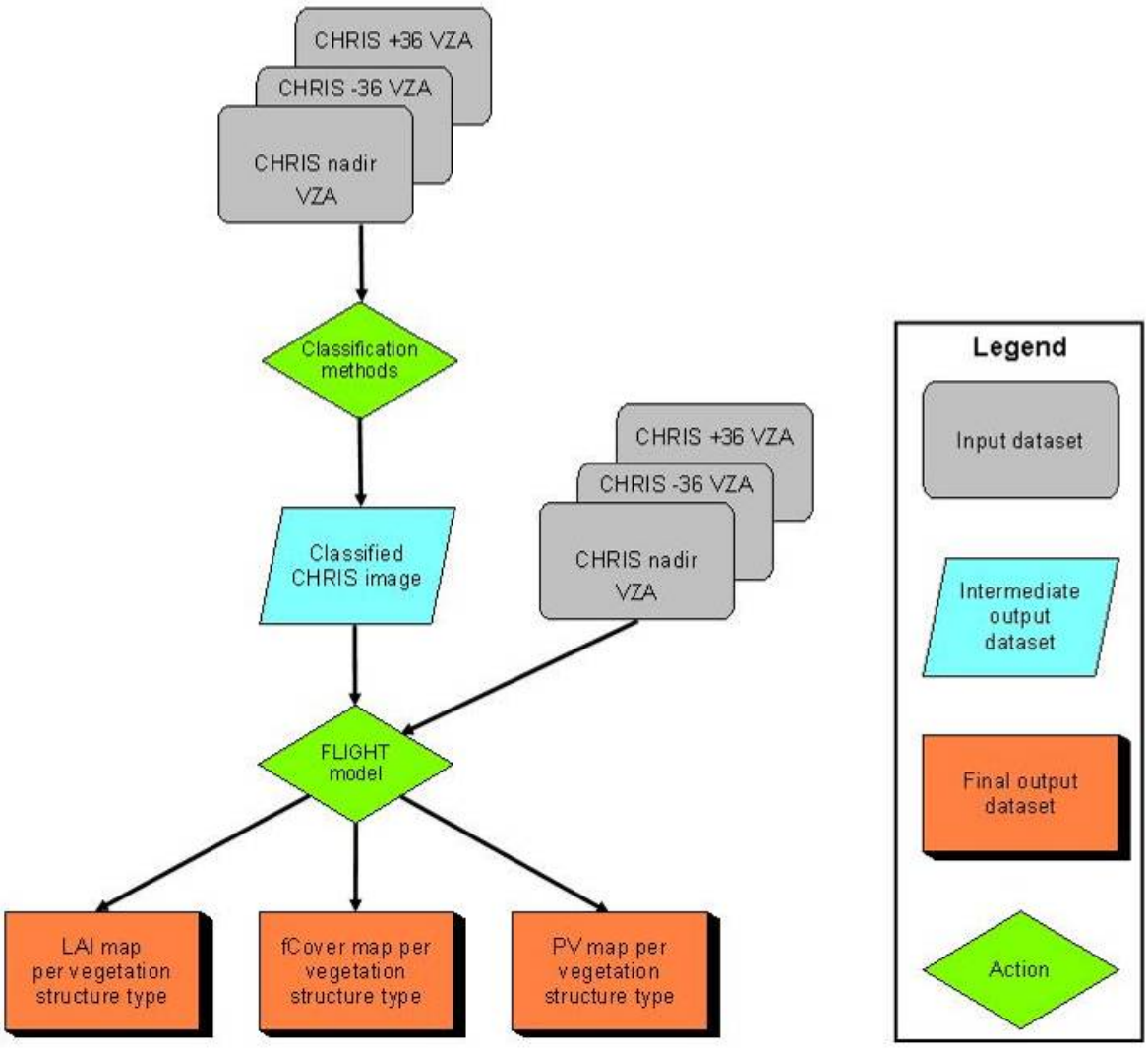

Figure 8: Overall flowchart showing a simplified version of the methodology that is followed in this thesis research.

3.3.2 Preprocessing

Atmospheric correction

The CHRIS images were already atmospherically corrected according to the method of Guanter et al. (2005). This method is widely accepted and has been taken up in the open source BEAM toolbox. BEAM is a toolbox for viewing, analysing and processing of remote sensing data from sensors such as MODIS, AVNIR, PRISM and CHRIS/Proba (European Space Agency, 2008). An atmospheric correction algorithm, which is a combination of radiative transfer and empirical line approaches, was used to remove the atmospheric distortion and artifacts due to miscalibration (Guanter et al., 2005). After this preprocessing step the CHRIS images contain HDRF data. The spectral signatures of objects in the corrected CHRIS images did not show any irregularities which means that the atmospheric correction had good results. Only some atmospheric noise can be observed in the first band, the blue band (442.6000 nm), but this is normal in this range of wavelengths. This band can be left out for further calculations.

Image registration

Thereafter, image registration was performed for the five angular images according to the method derived by Ma et al. (2009). With this method the five separate images were referenced to each other, so they precisely overlap each other. This allows automatic selection of a specific location in all five images at the same time. They used an automatic registration scheme for this, consisting of two methods for collecting control points.

Geometric correction

The next step was to perform geometric correction. Systematic distortions in remote sensing images due to scan skew, platform velocity, earth rotation etc. had already been removed when the images were obtained. No correction was done yet for unsystematic geometric distortions. The method for doing this is called geometric registration or georeferencing. It involves taking ground control points of clearly discernable objects in the satellite image. The same ground control points are collected on a map with a coordinate system or in an image that is already georeferenced. After that, a resampling method is applied to calculate the new pixel values in the satellite image. The following steps were taken to geometrically correct the CHRIS images.

1. Creation of a spatial subset (in ENVI)

The largest part of the CHRIS images cover the same area, but some parts do not overlap. The images with VZA -55 and +55 could not be used, because Millingerwaard is not included in these images. For the nadir, -36 and +36 VZA images a spatial subset was taken, in order to have the same extent for these images.

2. Geometric correction of the nadir image (In Erdas Imagine)

First the nadir image was georeferenced. The model properties were:

- Polynominal order: 2
- Projection: Bessel – Amersfoort 1

The aerial photograph of 2006 was used as reference image. 34 ground control points (GCP's) were selected in both images. Most GCP's were located in the river floodplains, the other GCP's were spread over the whole image.

Image resampling was performed, with the following parameters:

- Resample method: nearest neighbor
- Projection: double stereographic
- Output cell size: 17 m^2

The control point error of the nadir image after registration was: X (0.1954); Y (0.2450). The total RMS error was 0.3134.

3. Geometric correction of the other images (In Erdas Image)

Geometric correction was done for the -36 and +36 VZA images with use of the same GCP's. This was possible because the images were coregistrated well.
The control point error and RMS error for these 2 images was the same as for the nadir image.

4. Change of the coordinate system (In ArcGIS)

The spatial reference is Rijksdriehoekstelsel (RD new), because the aerial photograph was in this coordinate system. For further use with the image analysis and processing software ENVI, the coordinate system was changed into UTM projection (WGS 1984 UTM Zone 32N.prj).

3.3.3 Classification of vegetation structure types

3.3.3.1 Definition of classes

The classes that are chosen for classification are based on the vegetation structure classes described in Geerling et al. (2008). Five classes are given as a minimum for estimating hydraulic resistance for river management purposes: bare and pioneer communities; grasses and herbaceous vegetation; herbaceous ad low woody vegetation; bush; and forest.
For this research, the classes "water", "built-up" and "arable land" have been added to be able to classify the whole CHRIS image. In table 1 all classes are summarized, with the main characteristics of each class.

Table 1: Classes used for classification of RWS and CHRIS image

	Class name	Class characteristics
1	Bare soil & pioneer vegetation	mainly sand
2	Grasses and low herbaceous vegetation	vegetation < 1m
3	Higher herbaceous vegetation	vegetation between 1 m and 2 m
4	Shrubs	shrubs and trees < 5 m
5	Forest	trees > 5 m
6	Water	water
7	Built-up	streets, houses
8	Arable land	maize

During the first classification attempt the class of "arable land" was not included, resulting in arable land being classified as "shrubs". Shrubs and arable land have similar HDRF reflectance values, especially in the visible part of the spectrum. This is reasonable because agricultural crops may have some vegetation characteristics comparable to shrubs. Full grown maize for example has the same height as some shrubs. Arable land can not be included in the shrub class, because of the seasonal variation. On the aerial photograph, arable land can be discerned as bare soil. This is because the crops are harvested in Autumn and the aerial photograph was taken in early Spring. So by the time the photo was taken the land was still barren. The seasonal variation of arable land is different from shrubs. Therefore, to prevent arable land from getting mixed up with the shrub class, the new class "arable land" was created. In appendix II the spectral signatures from all classes are displayed for VZA -36, nadir and +36. The graphs contain HDRF values obtained from the angular CHRIS images.

3.3.3.2 Classification of RWS ecotopes

The legend that RWS used for the ecotope classification in 2005 is much more detailed, with around 70 ecotope classes. Because the RWS ecotope map will be compared with the classification outcome of the CHRIS image, the two classifications must consist of the same classes. Therefore the RWS ecotopes were reclassified into the 8 classes of table 1. First, an attempt was made to describe the species composition per ecotope class of the RWS dataset and then link this to the species composition of the ecotopes of the classes of Geerling et al. (2008). Background literature of the RWS ecotope map (Lorenz 2001; van der Molen et al., 2000; Willems et al., 2007) and of the classes of Geerling et al. (Schaminée et al., 1995-1999) have been used for this. But it appeared

not feasible to establish a link between the two classifications, because the same species groups occurred in more than one class of both classifications. It was too hard to decide which class of RWS could be linked to which class of Geerling et al.
Therefore, a simpler approach was used. The classes of RWS were subdivided under the 8 classes (table 1), based on their ecotope description. Appendix III contains the division of the RWS classes into the 8 new classes. In ArcGIS an extra column for the new class names was added to the attribute table and the detailed classes of RWS have been reclassified into the 8 new classes. A map was drawn in ArcGIS containing the new classes.

3.3.3.3 Classification of the CHRIS image

In figure 9 the flowchart of the methodology for the classification of the CHRIS image is presented. Most classification steps were performed in ENVI, some additional steps were taken in ArcGIS. In short the following steps, according to the numbers in figure 9 were taken:

1. A spectral subset is taken from the nadir image.
2. The layers of CHRIS nadir VZA, CHRIS -36 VZA and CHRIS +36 VZA are stacked.
3. Principal component analysis (PCA) is performed on the stacked layers image.
4. Maximum likelihood (ML) classification is performed on the nadir image. (= classification 1)
5. Support vector machine (SVM) classification is performed on the nadir image. (= classification 2)
6. ML classification is performed on the stacked layers image. (= classification 3)
7. ML classification is performed on the stacked layers image with PCA bands. Only the PCA bands 1, 2 and 3 are used. (= classification 4)
8. ML classification is performed on the stacked layers image with PCA bands. Only the PCA bands 1-4 are used. (= classification 5)
9. ML classification is performed on the stacked layers image with PCA bands. Only the PCA bands 1-5 are used. (= classification 6)
10. Each classified CHRIS image is transformed into an ENVI vector file.
11. Each ENVI vector file is saved as an ArcGIS shapefile.
12. Each ArcGIS shapefile is clipped with the RWS ecotope map.

The final maps contain the classification of the river floodplains of the Gelderse Poort. The next part contains a detailed explanation of the methodology. The different steps in-between brackets refer to the steps mentioned above.

Different input images were used for the classification. First, a spectral subset was taken from the nadir image, consisting of bands 2-18 (*step 1*). Band 1 (442.6 nm) was left out because it consisted of some atmospheric noise. Next, an image with stacked layers, consisting of the nadir, -36 and +36 VZA layers was prepared (*step 2*). This image consisted of 51 bands, three times bands 2-18. To reduce the dimensionality of the dataset, PCA has been performed on the stacked layers image (*step 3*).

Layer stacking (*step 2*)
The three layers of the nadir, 36 and +36 VZA were stacked, resulting in an image with 51 bands. Once the layers were stacked, the header information did not contain the right wavelengths, it only showed band 1, band 2, and so on until band 51. The right wavelengths were inserted by means of importing an ASCII file. The stacked layers image is one of the images that was used for classification.

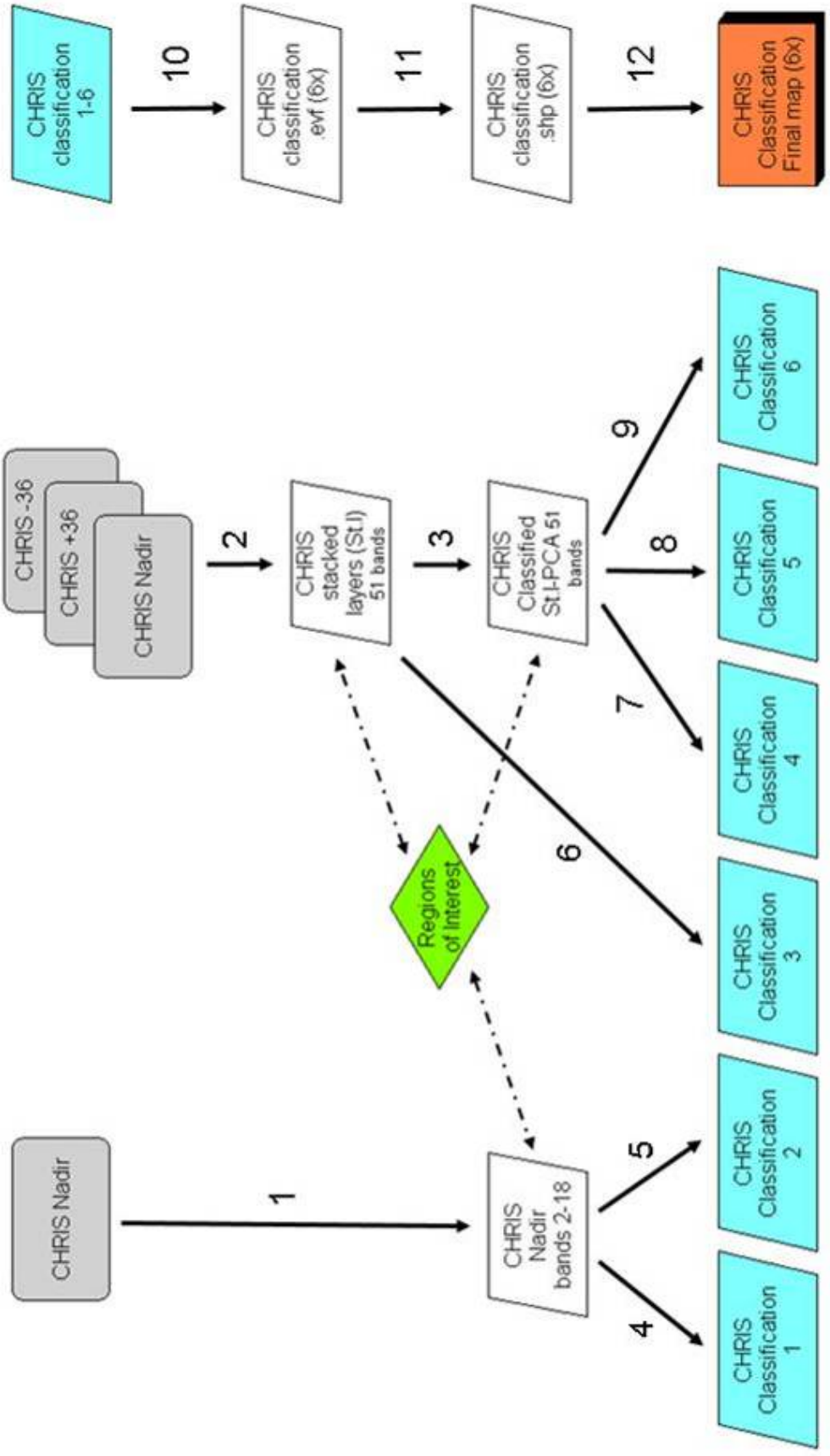

Figure 9: Flowchart methodology CHRIS classification

PCA (*step 3*)
With PCA, the often highly correlated multispectral bands are transformed into uncorrelated output bands, with maximized data variance. The output bands are linear combinations of the multispectral bands. The first PC band has the highest percentage of data variance, the second PC band the second highest, etc. A colour composite of PCA bands shows more colourful images than the colour composite of normal spectral bands. This is because the PCA data are uncorrelated and have a high variance (Richards & Xiuging, 1999). This PCA dataset has 51 bands, but only the first 3, 4 or 5 bands have been used for classification. They consist of > 95% of all variation in the data.

ROIs
For each of the 8 classes, regions of interest (ROIs) were selected. In this case, they were selected graphically, but they can also be selected by methods such as tresholding. Here, the ROIs consist of a combination of several polygons of the same class, for example 10 polygons of forested area. Each ROI should contain more than 51 pixels, otherwise the classification with the stacked layers image (consisting of 51 bands) is not possible. Appendix IV contains a map with the ROIs in Millingerwaard. More ROIs have been selected in other parts of the Gelderse Poort area.

The nadir image was used to roughly discriminate between classes. The aerial photograph of Spring 2006 and field knowledge were used as reference for finding the right ROIs. The PCA bands of the stacked layers image were used to identify sharp differences between classes. Certain combinations of PCA bands gave a good opportunity to distinguish certain classes from each other. For example the PCA bands combination of: Red - PCA band 1, Green - PCA band 3, Blue - PCA band 2 shows a very bright green colour for all the water parts which makes it easy to choose water ROIs. Other combinations like: Red - PCA band 3, Green - PCA band 5, Blue - PCA band 7 made it easy to choose arable land and to distinguish it from grasses or shrubs; they received a bright orange colour. Figure 10 shows those bright colour combinations and the locations of different ROIs.

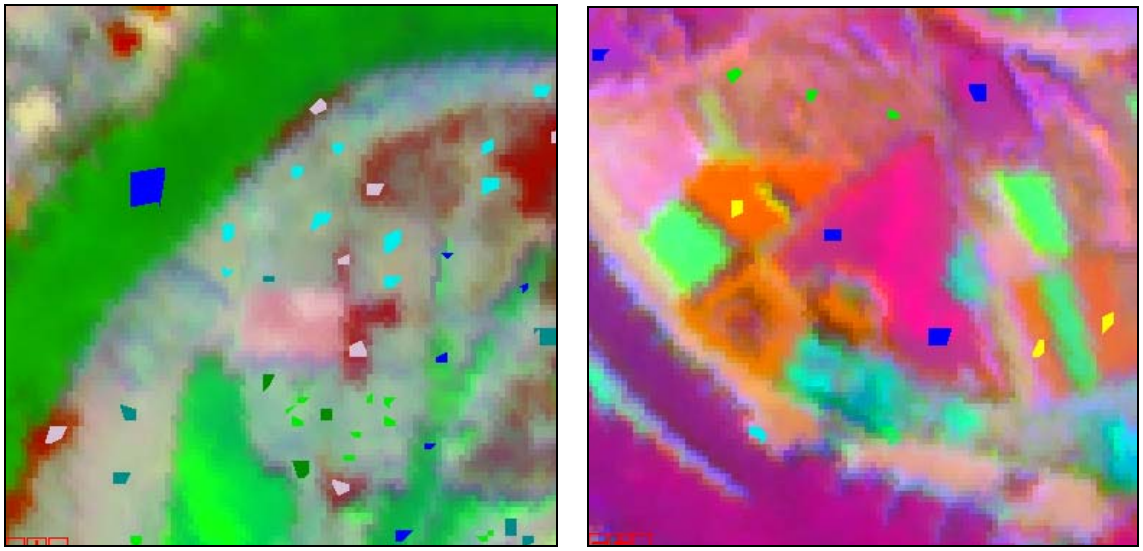

Figure 10: ROIs on different parts of the image Stacked layers with PCA bands. On the left side: Red-PCA band 1, Green-PCA band 3, Blue-PCA band 4; the bright green colour indicates water, the red colour indicates bare soil. On the right side: Red-PCA band 3, Green-PCA band 5, Blue-PCA band 7; the pink colour indicates water, the orange colour indicates arable land.

Classification methods
After ROI-selection, the classification of the CHRIS image was performed in ENVI, using two different methods: Maximum Likelihood (ML) and Support Vector Machine (SVM).

Maximum likelihood classification
With ML classification the assumption is made that the reflectance values for pixels of each class are normally distributed in each spectral band. For every pixel the probability is calculated that it belongs to a certain class. The pixel is then assigned to the class for which it has the highest probability (the maximum likelihood). The discriminant functions for each pixel in the image are calculated with the following formula (Richards & Xiuping, 1999):

$$g_i(x) - \ln p(\omega_i) - \tfrac{1}{2} \ln|\Sigma_i| - \tfrac{1}{2} (x - m_i)^t \Sigma_i^{-1} (x - m_i) \quad (4)$$

i = class
x = n-dimensional data (where n is the number of bands)
$p(\omega_i)$ = probability that class ω_i occurs in the image and is assumed the same for all classes
$|\Sigma i|$ = determinant of the covariance matrix of the data in class ω_i
$\Sigma i\text{-}1$ = its inverse matrix
mi = mean vector

Support Vector Machine classification
SVM classification works well with complex and noisy data. It uses a statistical approach. Each class is separated with a decision surface: a hyperplane. The data that lie closest to the hyperplane are called support vectors. For each pixel the decision values for each class are calculated. These values are used to make probability estimates. Every pixel is assigned to the class with the highest probability. A function to use for the kernel type has to be chosen: radial basis function, linear, polynomial, sigmoid. For this research, the default radial basis function was used, this works well in most cases (Wu et al., 2004). The mathematical representation is as follows:

$$K(xi, xj) = \exp(-g\|xi - xj\|2), g > 0 \quad (5)$$

g = the gamma term in the kernel function

The gamma in the kernel function has to be indicated. The default value of 0.056 was taken; this is the inverse of the number of bands in the input image. One can choose the number of pyramid levels used for classification. This sets the number of hierarchical processing levels. Here the value was set to 0 (default), this means the image is processed at full resolution. A penalty parameter can be used to account for misclassifications. It allows for training errors, so it allows for some training points on the wrong side of the hyperplane. It forces to create a more accurate model (Wu et al., 2004). For this research, first the SVM classification was performed without penalty parameter. The second time a penalty parameter of 100 was used, this is the default setting. Furthermore, a classification probability threshold (probability that is required to classify a pixel) can be indicated. This option was not used, because the whole image had to be classified.
As the processing time of the support vector machine is high, the software uses a hierarchical, reduced-resolution classification process. This process is most effective in areas that contain homogeneous features, like water bodies and fields. The more pixels in the ROIs, the better the classification results are.

Both methods have been performed on the nadir image, as well as on the stacked layers image and the stacked layers PCA images. Only a selection of the outcomes is presented in the results sections of this report, namely: nadir/ML (*step 4*); nadir/SVM (*step 5*) without penalty parameter; stacked layers/ML (*step 6*); stacked layers+PCA with 3,4 and 5 bands and ML classification (*step 7, 8, 9*) (see figure 9). This selection gives the best results of all the methods that were compared.

The classified images had to be transformed into an ENVI vector file (.evf) (*step 10*) and than exported to a shapefile (.shp) (*step 11*). This shapefile can be opened in ArcGIS and has an attribute table containing the 8 classes. In ArcGIS the classified CHRIS image was clipped with the RWS ecotope polygon (*step 12*), so both images have the same shape which makes it easier to validate them with the aerial photograph.

3.3.3.4 Validation of classification results

Validation of ROIs
The ROIs were validated by computing the ROI separability. This is a statistical measure of distance between the spectral signatures of ROI pairs for a given input file. Both the transformed divergence and the Jeffries-Matusita Distance were calculated. These values range from 0 to 2.0 and indicate how well the selected ROI pairs are statistically separated. Values greater than 1.9 indicate that the ROI pairs have good separability. Between 1.7 and 1.9, the separation is fairly good. Below 1.7 there is poor separation. ROI pairs with a separability value lower than 1 might be combined into a single ROI.

Transformed divergence
The transformed divergence gives an exponentially decreasing weight to increasing distances between the classes.

$$D_{ij} = \tfrac{1}{2}\mathrm{tr}\left(\left(C_i - C_j\right)\left(C_i^{-1} - C_j^{-1}\right)\right) + \tfrac{1}{2}\mathrm{tr}\left(\left(C_i^{-1} - C_j^{-1}\right)\left(\mu_i - \mu_j\right)\left(\mu_i - \mu_j\right)^T\right) \quad (6)$$
$$TD_{ij} = 2000\left(1 - \exp\left(-D_{ij}/8\right)\right)$$

i and j = the two signatures (classes) being compared
Ci = the covariance matrix of signature i
μi = the mean vector of signature i
tr = the trace function (matrix algebra)
T = the transposition function

Jeffries-Matusita Distance
The Jeffries-Matusita distance is calculated with the following formula:

$$\alpha = \frac{1}{8}\left(\mu_i - \mu_j\right)^T \left(\left(C_i + C_j\right)/2\right)^{-1}\left(\mu_i - \mu_j\right) + \frac{1}{2}\ln\left(\left|\left(C_i + C_j\right)/2\right| / \sqrt{|C_i|x|C_j|}\right) \quad (7)$$
$$JM_{ij} = \sqrt{2\left(1 - e^{-\alpha}\right)}$$

i and j = the two signatures (classes) being compared
Ci = the covariance matrix of signature i
μi = the mean vector of signature i
ln = the natural logarithm function
|Ci| = the determinant of Ci (matrix algebra)

The outcome is a listing of the computed divergence for every class pair and one band combination. In this case the band combination is RBG (Red: band 8, Blue: band 4, Green: band 2) from the CHRIS nadir image. The listing contains the transformed divergence and the Jeffries-Matusita distance for every possible pair of signatures (Richards & Xiuping 1999).

Validation of classification results with random sample points
First the classification results have been roughly checked in the field. This was done in the month of March, 2009. After field validation the CHRIS classifications and the RWS classification have been validated with the aerial photograph of early Spring 2006 as ground truth map. Twenty random sample points were taken for each class in the CHRIS nadir image, using the Hawth's

toolbox in ArcGIS. To prevent the points from being too close to each other, a rule was implemented that the distance between two random points must be more than 100 meter. In total 160 sample points were selected. For each point the class in the CHRIS classification, the class in the RWS classification and the class visible in the aerial photograph were registered. It was not possible to see the differences between "low grasses & herbaceous vegetation" and "higher herbaceous vegetation" on the aerial photograph. Based on field knowledge, and the idea that in a river floodplain ecosystem the patches of grass with a natural shape (not a square) will probably contain higher grasses and herbaceous vegetation, the assumption was made that those patches belong to the class of "higher herbaceous vegetation". Confusion matrices were made for the CHRIS classifications and for the RWS classification with the aerial photograph classes as ground truth. A confusion matrix is a table that shows the classes for each sample point in the classified image and in the validation image. Misclassifications become clear in this table.
The accuracy (user accuracy) and reliability (producer accuracy), the error of omission, the error of commission have been calculated for the CHRIS nadir ML classification, using the following formulas:

$$\text{Accuracy} = \frac{\text{Correctly classified pixels}}{\text{Total of pixels in ground truth class}} * 100\% \quad (8)$$

$$\text{Error of omission} = \text{1-Accuracy} \quad (9)$$

$$\text{Error of commission} = \frac{\text{wrongly classified pixels}}{\text{total of pixels in classified class}} * 100\% \quad (10)$$

$$\text{Reliability} = \text{1 – Error of commission} \quad (11)$$

$$\text{Overall accuracy} = \frac{\text{sum of correctly classified pixels on the diagonal in the confusion matrix}}{\text{total of classified pixels}} * 100\% \quad (12)$$

The accuracy indicates the extent to which the processing method correctly identifies the selected classes. The reliability shows what percentage of a particular ground truth class was correctly classified. The overall accuracy is the percentage of correctly classified pixels. The error of omission is a measure for the pixels that are incorrectly excluded from a particular class. The error of commission is a measure for the pixels that are incorrectly assigned to a particular class, but actually belong to an other class.

The kappa coefficient is a statistical measure of agreement, beyond chance, between the two maps. It is calculated with the following formula (Carletta, 1996):

$$K = (P(A) - P(E))/(1 - P(E)) \quad (13)$$

P(A) = the proportion of times that the coders agree and
P(E) = the proportion of times that we would expect them to agree by chance

Equation 14 is the more formal definition of the kappa value.

$$\hat{K} = \left(N\sum_{i=1}^{r} x_{ii} - \sum_{i=1}^{r} (x_{i+} * x_{+i}) \right) / \left(N^2 - \sum (x_{i+} * x_{+i}) \right) \quad (14)$$

R = the number of rows in the confusion matrix
x_{ii} = the number of observations in row i and column i (on the major diagonal)
x_{i+} = the total observations in row i

x_{+1} = the total of observations in column i
N = the total number of observations included in the matrix
(Canada Centre for Remote Sensing, 2009)

For the other classification methods of the CHRIS image, only the overall accuracy has been calculated.

3.3.4 Estimation of vegetation structure properties using the model FLIGHT

3.3.4.1 Choice of classes to use for the model

The CHRIS classification resulted in 5 vegetation structure classes. Table 2 shows how these classes are linked to the classes that are used in Geerling et al. (2008). Geerling et al. used the first 5 classes as a minimum for estimating hydraulic resistance for river management purposes.

As can be seen in table 2, the hydraulic roughness does not differ very much between the lower herbaceous and higher herbaceous vegetation groups. The ranges are from (0.25-0.73) - (1.07-1.45). These values lie close to each other compared to the 24.41 and 12.84 of the shrubs and forest classes. The herbaceous classes were hard to separate with the classification of the CHRIS images, so those 2 groups could form 1 group as input for the model. The first class of bare soil and pioneer vegetation has low water resistance values of 0.15-0.30. This class was left out for modelling purposes because it does not have a big influence on the hydraulic resistance. The vegetation structure groups that will be used as input for the model FLIGHT are noted in table 3.

Table 2: Relation between the different vegetation structure classes

Geerling et al. (p.76)	**Geerling et al. (p.55) & hydraulic roughness indication** (k at 4m waterdepth)	**CHRIS classification**
Bare and pioneer communities	Dry bank / sand (0.15)	Bare soil & pioneer vegetation
	Pioneer vegetation (0.28)	
	Groin (0.30)	
Grasses & low herbaceous vegetation	Production grassland (0.25)	Grasses & low herbaceous vegetation
	Natural grassland (0.39)	
	Mixed grassland & herbaceous (0.73)	
Higher herbaceous vegetation	Herbaceous levee (1.07)	Higher herbaceous vegetation
	Dry herbaceous vegetation (1.45)	
Bush	Softwood bush / bush (24.41)	Shrubs
Forest	Softwood forest (12.84)	Forest

Table 3: Vegetation structure classes as input for the model FLIGHT

Class name	**Hydraulic resistance values**
Herbaceous vegetation	0.25-1.45
Shrubs	24.41
Forest	12.84

3.3.4.2 Processing steps for running the model FLIGHT

General overview of the FLIGHT modelling procedure

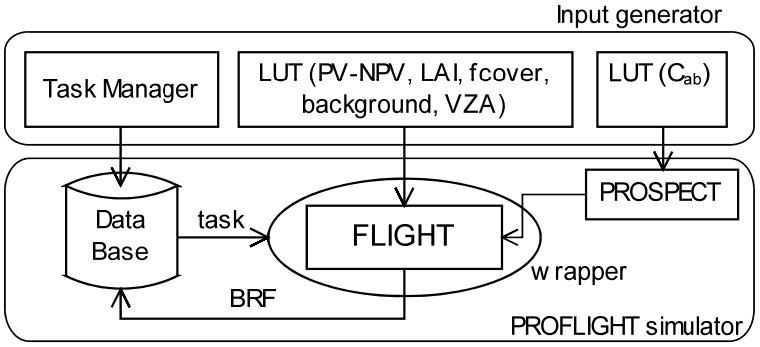

Figure 11. Schematic diagram showing the modelling procedure of (PRO)FLIGHT

Figure 11 shows that the modelling procedure of PROFLIGHT is built up by two independent modules. For this thesis research, the PROSPECT part (on the right side of the figure) is not used. The first procedure comprises an interface where the user can fill the LUTs with input files for PROSPECT and FLIGHT. Parameter values of leaf biochemicals and 3D canopy structure have to be entered. For the variables, only the boundaries and LUT steps need to be filled in. Tabular data of the requested scenarios are then automatically generated. Also, a task manager file is created that consists of all the tasks that have to be executed. Each task represents a forest scenario. The tasks are stored in a relational database.
The second module is the PROFLIGHT simulator. It executes the tasks in the task manager by feeding FLIGHT with the right input files from the database. It flags the tasks with "pending", "in progress", "finished" or "error occurred". When an error occurs, the system automatically proceeds with the next task. When a task is finished, the simulated BRF result is stored in a database. This automated process results in a large dataset. With SQL queries the desired subsets from the generated database can be extracted.

FLIGHT processing steps
The flowchart in figure 12 shows the processing steps for running the model FLIGHT and deriving the final results of leaf area index (LAI), fractional cover (fCover) and fraction of photosynthetic vegetation (PV) per pixel in the CHRIS image. The numbers in the figure correspond to the numbers of the steps listed below. Further on the steps are explained in more detail.

1. Run IDL/ENVI script for LUT generation.
2. Run IDL/ENVI script for spectral resampling.
3. Create database and tableformats (TASKLIST & output_FLIGHT) using MySQL.
4. Copy "inflight_data" to Linux using WinSCP.
5. Fill tables (TASKLIST) with "inflight_data" using MySQL.
6. Copy resampled spectra to Linux using WinSCP.
7. Run the FLIGHT model using python scripts.
8. Copy .csv output files to desktop pc using WinSCP.
9. Run IDL/ENVI inversion script for generation of LAI, fCover, PV and minimum RMSE maps.

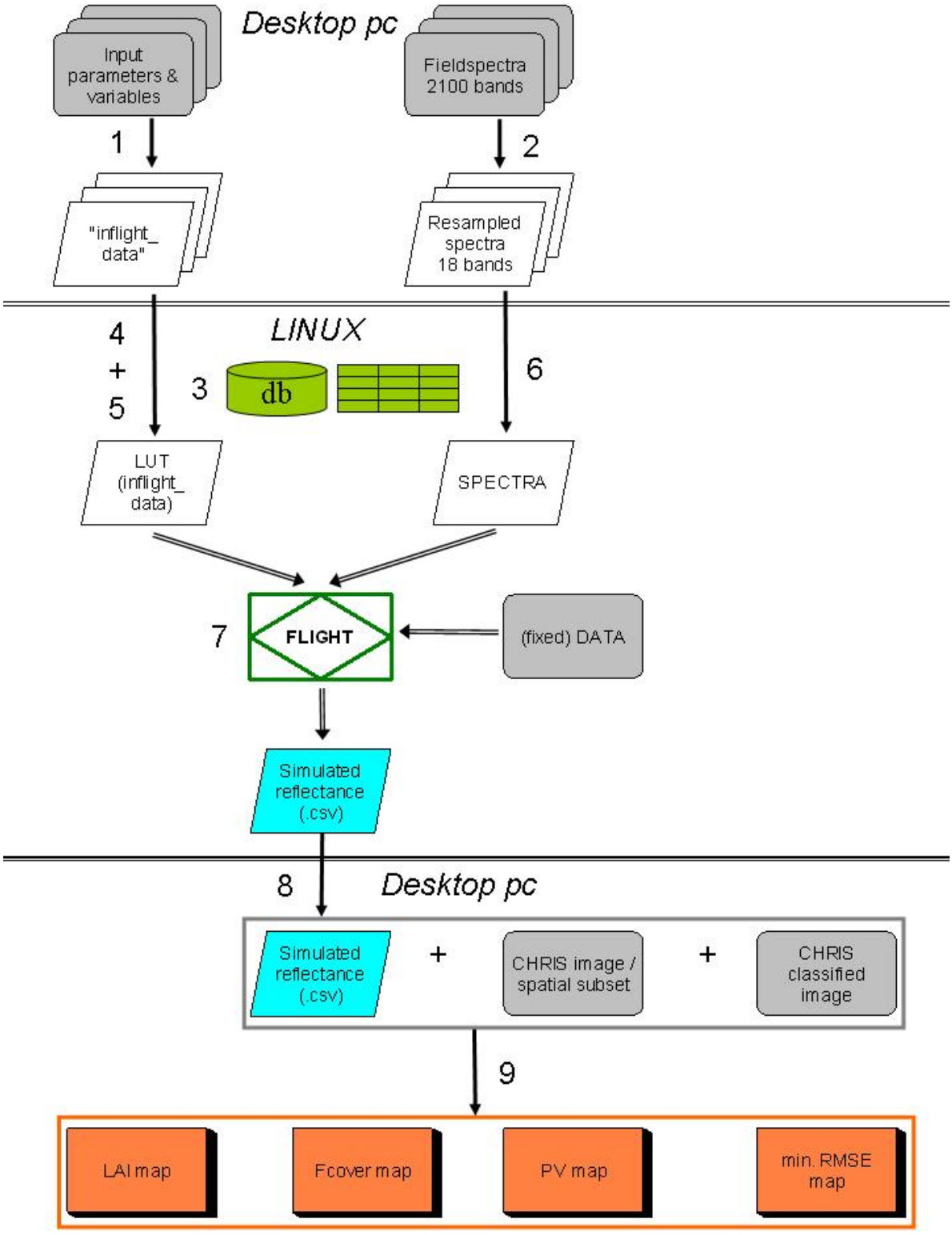

Figure 12: Flowchart showing the steps that need to be taken to run the FLIGHT model and derive the vegetation structure properties maps.

Several python scripts were used to run the model. The scripts were modified to the data from the forest, shrubs or herbaceous class. All the python and IDL/ENVI scripts, as well as some MySQL commands are taken up in appendix A and B on the cd-rom that has been added to this thesis report. To explain them, the names of the scripts created for the "forest class" are used in the next section.

Generation of LUT

1. Run IDL/ENVI script for LUT generation.

First a LUT was created for each of the vegetation structure classes. The LUT consists of all the model parameters and variables. Most model and vegetation structure parameters had a fixed value. There are three variables in the model: LAI, fCover and fraction PV. They each received a range of values in-between which they may vary. This means that many combinations of the different model parameters and variables are possible and that the LUTs have a big extent. Each vegetation structure class has its own characteristics and thus needed its own LUT. In table 4 the ranges of values for the variables for the first model run are indicated. A large range for each variable is first used to keep on the safe side. For the second model run the ranges were reduced and refined. For the herbaceous class for example the LAI values range from 0.5 – 7. The values increase with 0.5 until the value of 5 is reached, and then the values increase with 1 until the value of 7 is reached.

Table 4: Ranges of values for the variables fCover, LAI and PV for the 1st model run

Vegetation structure class	Fcover	LAI	PV
Herbaceous	0.6-1; step: 0.05	0.5-7; step: 0.5 until 5; step: 1 until 7	0.5-1; step: 0.1
Shrubs	0.5-1; step: 0.05	0.5-7; step: 0.5 until 5; step: 1 until 7	0.5-1; step: 0.1
Forest	0.2-1; step: 0.05	0.5-10; step: 0.5 until 5; step: 1 until 10	0.3-1; step: 0.1

Appendix V contains all the model and vegetation structure parameters and variables that filled the LUT, together with a description of them.

The LUT was created by running a script in IDL/ENVI (prospect_flight_soil.pro) (appendix A.1 on cd-rom). The script "textbox.pro" needs to be open too, to be able to run LUT script. When executing this script popup-windows appear and the numbers and ranges of values for each of the parameters can be filled in. The output of the script is stored in data files that are called "inflight".

Spectral resampling

2. Run IDL/ENVI script for spectral resampling.

Leaf reflectance and transmittance, bark reflectance and background reflectance spectra are needed as model input for each vegetation structure class.
Leaf spectra were already obtained and processed (Liras, 2005) during the field campaign in 2004 with the Fieldspec Pro. Fr.® (portable spectro-radiometer). This equipment measures in 2100 bands, ranging from 350 to 2450 nm with steps of 1 nm in-between the bands. The spectra showed atmospheric noise around 1350-1400 nm and 1800-1950 nm. Those parts have been deleted. Some spectra showed a few values above 1. These values have been deleted too. Measurements were taken with white and black backgrounds.
The following formulas have been used to calculate leaf reflectance and transmittance.

$$\text{Leaf reflectance} = \mu\,(\text{reflectance spectra with a black background}) \quad (15)$$

$$\text{Leaf transmittance} = \mu\,(\text{reflectance spectra with white background}) - \text{leaf reflectance} \quad (16)$$

With a black background, no transmitted radiance is reflected back, so only the "real" reflectance is measured. Using a white background, this transmitted radiance is reflected back to the Fieldspec, together with the leaf reflectance. So the transmittance can be obtained by substracting the reflectance with a black background from the reflectance with a white background.

Field spectra of different bark and background types have been collected during the thesis research in the beginning of April 2009 with the Fieldspec Pro. Fr.®, near Alterra in Wageningen. Table 5 shows the spectra that were chosen as model input for the 3 vegetation structure classes for the 1st model run.

Table 5: Measured input spectra for the 1st model run

Spectra	Herbaceous	Shrubs	Forest
Leaf	*Calamagrostis epigejos*	*Salix alba*	*Salix alba*
Bark	-	*Salix alba*	*Salix alba*
Background	Sand	The average of grass + water and a forest background	Forest background

Salix alba is the most representative species for both the shrubs and forest class. The only available leaf measurements for grasses and herbaceous vegetation were from *Calamagrostis epigejos*. This species can grow quite high, so it can represent the herbaceous class, that consists of both small and higher herbaceous vegetation. The forest background is a mixture of leaves, branches and moss. Most shrubs in Millingerwaard grow on a wet underground, but the background is also covered by twigs and leaves. That is why those two measured background types were combined for this class. Sand was taken as background for the herbaceous class, because it approximates the soil that is present underneath the herbaceous vegetation in Millingerwaard.

The spectra were resampled to the CHRIS bands in order to have suitable model input spectra using a script in IDL/ENVI (spectral_resampling.pro) (appendix A.2 on cd-rom). The script "textbox.pro" needs to be open too. With spectral resampling the number of bands from the Fieldspec has been reduced to the number of bands from the CHRIS image, which is 18. The new bands of the spectra fit exactly to the wavelengths of the CHRIS bands. The output is a text file with the reflectance (and transmittance) values for each CHRIS waveband.

3. Create database and tableformats (TASKLIST & output_FLIGHT) using MySQL.

The next steps were taken with the LINUX computer, via a connection in the WUR-network, because of the big computational load of the model. A shell was used to connect to the MySQL database and to execute python scripts. The input and output data for the model needed to be stored in a database. So, first a new database "erika" was created with MySQL. Table formats for the inflight-data (called TASKLIST) and for the flight output data (called output_FLIGHT) were created; 1 for each vegetation structure class. The TASKLIST contains the LUT values with a unique task_id for each combination of parameters and variables to run the model.

The following MySQL commands were used to create the table formats (Appendix B.1&2 on cd-rom):

- TASKLIST_forest

```
CREATE TABLE IF NOT EXISTS TASKLIST_forest
( task_ID INT NOT NULL,
  status VARCHAR (15),
  HOSTNAME VARCHAR (50),
  background VARCHAR(15),
  VZA_label VARCHAR(15),
  VZA VARCHAR(5),
  LAI DECIMAL(4,1),
  PV DECIMAL(3,2),
  fcover DECIMAL(3,2),
  scene VARCHAR (2),
  PRIMARY KEY (task_ID));
```

- Output_FLIGHT_forest

```
CREATE TABLE IF NOT EXISTS flight_output_forest
( task_ID INT (11) NOT NULL,
  bandnumber INT (11) NOT NULL,
  wavelength INT (11) NOT NULL,
  fdif float NOT NULL,
  wrefl float NOT NULL,
  PRIMARY KEY (task_ID, wavelength));
```

4. Copy “inflight_data” to Linux using WinSCP.

The “inflight_data” were copied to the LINUX computer with a programme called WinSCP.

5. Fill tables (TASKLIST) with “inflight_data” using MySQL.

Then the tables “TASKLIST” (TASKLIST_forest, TASKLIST_shrubs and TASKLIST_herbaceous) were filled with the “inflight_data” (compressed text-files) for the LUT, using MySQL statements (Appendix B.3 on cd-rom).

```
LOAD DATA LOCAL INFILE 'compressed_LUT_prospect_FLIGHT_forest.txt'
INTO TABLE TASKLIST_forest
FIELDS TERMINATED BY ","
OPTIONALLY ENCLOSED BY """;
```

6. Copy resampled spectra to LINUX using WinSCP.

The resampled spectra were copied to the LINUX computer.

7. Run the FLIGHT model using python scripts.

Now the model FLIGHT can be run. A python script (PROFLIGHT_forest.py) was used to run the (PRO)FLIGHT.exe model (North, 1996) based on the LUTs. Within this python script there is a link to another python script (Taskmanagercl_forest.py) which stores al the output .txt files into the database table “output_FLIGHT” (Appendix A.3 on cd-rom). All combinations in the LUT are used for the model runs and FLIGHT generates outputs belonging to all these combinations. The model has been run in the so-called “reverse” mode. This means that the outputs are TOC BRF reflectance values for a specified view direction and for any combination of LUT values. The resampled spectra were taken from the folder “SPEC” and some fixed data were taken from the folder “DATA”. These folders need those specific names, because the model refers to them. Then the data in the output tables were written to .csv files (which can be opened for example in excel). This was done by running another python script “getMySQLforest.py” (Appendix A.4 on cd-rom). In the script there is an inner join of the output table and the tasklist table on the field (task_ID) to couple the generated BRF values back to the LUT-information. The output consists of combined columns of those 2 tables: task_ID, background type, VZA-label, VZA, LAI, PV, Fcover, wavelength and wrefl.

The innerjoin is written as follows:

```
SELECT task_ID, background, VZA_label, VZA, LAI, PV, fcover, wavelength, wrefl
        FROM flight_output_forest inner join TASKLIST_forest using (task_ID);
```

Some useful shell and MySQL commands have been taken up in appendix B.4 on the cd-rom. They have been used to keep track of the modelling process and the database creation.

8. Copy .csv output files to desktop pc using WinSCP.

The output .csv files were copied to the desktop pc for further use.

9. Run IDL/ENVI inversion script for generation of LAI, fCover, PV and minimum RMSE maps.

The final script is the IDL/ENVI script: chris_inversion.pro (Appendix A.5 on cd-rom). The CHRIS image (with a certain angle), the classified image (created in 3.2) and the .csv file are needed as input files. The script allows refinement of the simulations by narrowing the ranges of values for LAI, fCover and PV. For example, the forest class is chosen. The script calculates the best match for the simulated BRF spectra and the CHRIS HDRF spectra, which is determined based on a cost-function. Three cost-functions were implemented in the script: the RMSE (17), the relative RMSE (18) (Weiss et al., 2000) and an other cost function (19) (Gobron et al., 1997):

$$\text{RMSE} = \sqrt{\left(\sum \frac{(\text{CHRIS reflectance} - \text{simulated reflectance})^2}{\text{N° of bands}}\right)} \quad (17)$$

$$\text{Relative RMSE} = \sqrt{\left(\sum \frac{((\text{CHRIS reflectance} - \text{simulated reflectance}) / \text{CHRIS reflectance})^2}{\text{N° of bands}}\right)} \quad (18)$$

$$x = \sqrt{\left(\sum \frac{((\text{CHRIS reflectance} - \text{simulated reflectance}) / (\text{CHRIS reflectance} + \text{simulated reflectance}))^2}{\text{N° of bands}}\right)} \quad (19)$$

The script generates maps with the variables LAI, Fcover, PV, according to the LUT values that go with the minimum of the cost-function. In case of an ill-posed problem (same RMSE, different variables) the script writes away extra info (SD, min, max) and calculates the average for the variables. The maps are created for one certain class, a certain angle and a certain LUT range.
For the 1st model run, Millingerwaard was used as spatial subset. The maps of the three classes were combined, using band-math expressions in ENVI, to show the LAI, Fcover or PV for herbaceous, shrubs and forest together in one map.
The created LAI and fCover maps had the rectangular shape from the CHRIS subset, so afterwards a new spatial subset from those maps was taken for only the river floodplain areas. This was done by subsetting the data via ROIs with the RWS vector file (.evf) as ROI. Histograms of LAI and fCover values were made by exporting them to ASCII files and adjusting them in Excel. The histograms contain LAI and fCover values for each angular map, summarized per vegetation structure type, and also summarized for all vegetation structure types together. All maps and histograms were created for the Millingerwaard and later for the whole Gelderse Poort area.

3.3.4.3 Model refinement for the 2nd model run

After looking at the first modelling results the values for the 3 LUT variables have been refined. Most LAI values for the herbaceous and shrub classes had received the highest available value of 7, so the herbaceous and shrubs LAI ranges were extended until 10 and 12 respectively. The minimum for these classes was shifted up a little bit, because there were no LAI values smaller than 1 and 2.5 respectively. For the forest class, the LAI range was also extended until 12. This was done based on the LAI measurement results in 2005 (Gonsamo, 2006), where the highest LAI values of the *Salix* species did not exceed 12. The minimum for this class was set at 2.5, because there were no LAI values lower than that.
The ranges for FCover have been reduced, based on the first inversion results. Most values for herbaceous, shrubs and forest were above 0.5 and 0.7 respectively. The new ranges were set to a minimum 0.6 for herbaceous, 0.7 for shrubs and 0.8 for forest. These new ranges seem more realistic when looking at the vegetation coverage on the aerial photograph for a CHRIS pixel.
The ranges for PV were adjusted as well. The value for the herbaceous class was set to 1, because herbaceous vegetation does not contain non-photosynthetic material: it does not contain bark or other woody elements. The ranges for shrubs and forest were set to 0.7-0.95. These values are estimated based on similar values found in literature (Broadbent, et al., 2006; Gensuo, et al., 2006; Guerschman, et al., 2009). The new ranges of values for the variables, used for the 2nd model run, are presented in table 6.

Table 6: Ranges of values for the variables fCover, LAI and PV for the 2nd model run

Vegetation structure class	fCover	LAI	PV
Herbaceous	0.7-1; step: 0.05	1-10; step: 0.5 until 7; step: 1 until 10	1
Shrubs	0.6-1; step: 0.05	2.5-12; step: 0.5 until 7; step: 1 until 12	0.7-0.95
Forest	0.8-1; step: 0.05	2.5-12; step: 0.5 until 7; step: 1 until 12	0.7-0.95

For the 2nd model run, first the Millingerwaard was used as spatial subset. Second, results were obtained for the Gelderse Poort, using the complete CHRIS image as spatial subset.

3.3.4.4 Validation of structure properties

Validation of modelled LAI values was done with ground measurements from 2004 (Mengesha, 2005) and 2005 (Gonsamo, 2006). In 2004 LAI measurements were obtained by means of hemispherical photography and in 2005 a combined method of hemispherical photography and TRAC measurements, adjusting the LAI outcome of the hemispherical photography for clumping index, was used. Two sets of validation points with measured LAI values were loaded into ArcGIS (appendices VI and VII). The LAI maps were overlaid by these validation points to obtain the modelled LAI for the validation points.
The modelled LAI values were compared with the measured LAI values from 2004 and 2005 by means of scatter plots. Outliers were excluded and linear regression functions were calculated. The R^2 values (coefficient of determination) give an indication of how good the validation results are.

fCover validation data were available from the same ground measurements from 2004. Modelled fCover was validated using the same methodology as for LAI.

4. Results

4.1 Classification of vegetation structure types

4.1.1 RWS classification

Figure 13 shows the RWS ecotope map for the river floodplains in the Gelderse Poort after classification into the 8 classes. The total area of forest is small; most of it is located in the Millingerwaard. Also, most of the bare soil parts are present in Millingerwaard as bare land and sand dunes along the river Waal. Furthermore the largest part of the Gelderse Poort consists of grasses and low herbaceous vegetation. These can be agricultural or natural grasslands and vegetations. Arable land takes up a large part of the Gelderse Poort as well. Some of those agricultural fields lie within Millingerwaard. Water is present almost everywhere in the image, apart from the river, sometimes as small lakes, sometimes as side streams of the river.

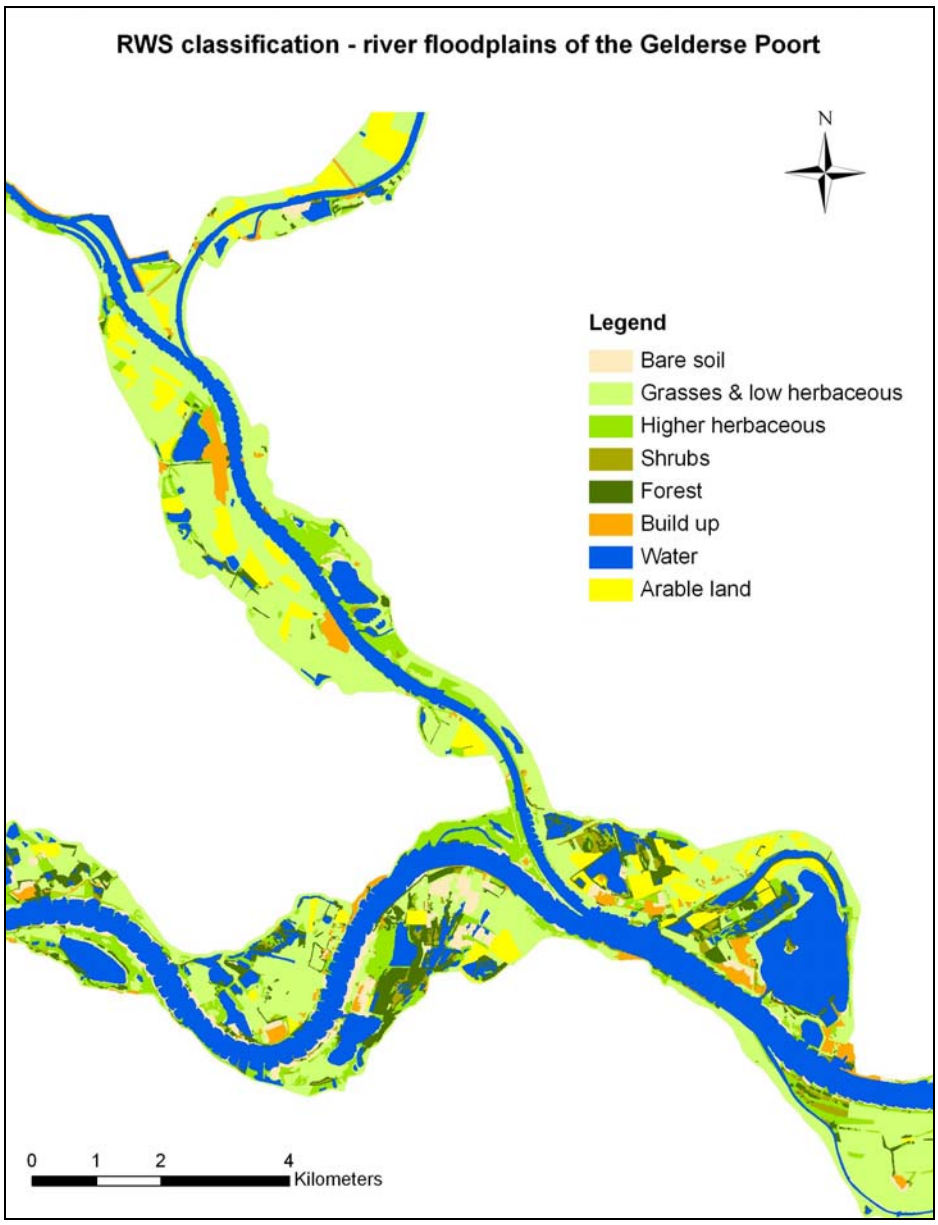

Figure 13: Classified RWS ecotope map of the Gelderse Poort

Validation

Table 7: Confusion matrix RWS classification

Ground truth	Bare soil	Grass & low herbaceous	Higher herbaceous	Shrubs	Forest	Arable land	Water	Build up	Total
Bare soil	7	3				1	3	3	17
Grass & low herbaceous		34				4	1		39
Higher herbaceous	1	4	6						11
Shrubs			2	8	2				12
Forest			1	1	23			1	26
Arable land		1				18			19
Water		1					22		23
Build up	1	1						11	13
Total	9	44	9	9	25	23	26	15	160

Table 8: Accuracy RWS classification

Classes	Accuracy (%)	Error of omission (%)	Error of commission (%)	Reliability (%)
Bare soil	41,18	58,82	22,22	77,78
Grass & low herbaceous	87,18	12,82	22,73	77,27
Higher herbaceous	54,55	45,45	33,33	66,67
Shrubs	66,67	33,33	11,11	88,89
Forest	88,46	11,54	8,00	92,00
Arable land	94,74	5,26	21,74	78,26
Water	95,65	4,35	20,00	80,00
Build up	84,62	15,38	26,67	73,33

Table 7 contains the confusion matrix for the RWS classification and table 8 the corresponding accuracy measures. The overall accuracy is 80.63%. The Kappa coefficient is 0.66. The accuracies of the classes “grasses and low herbaceous vegetation”; “forest”, “arable land” and “water” are high. The accuracy of bare soil is the lowest. Bare soil is often wrongly classified as water or built-up area. The reliability (producer’s accuracy) is highest for the forest class.

4.1.2 CHRIS classification

Figure 14 shows the feature space plot with a cloud of points from the CHRIS nadir dataset. On the Y-axis is the NIR band (band 14), on the x-axis the Red band (band 8). The coloured circles contain the pixels from the ROI classes. The water class has a low HDRF in both the Red and the NIR band. The bare soil class has a high reflectance in Red. The vegetation classes and the arable land class lie close to each other, but they do not really overlap. They have high reflectance values for the NIR wavelengths and quite low values in the Red band. The built-up class lies somewhere in-between the other classes.
In figure 15 the spectral signatures of the 8 classes are plotted. The signatures belong to a pixel that lies within the ROI class in the feature space plot (figure 14). The signatures for “water” and “grasses and low herbaceous vegetation” are plotted twice, because those classes cover a large area in the feature space plot. It probably concerns different kinds of grasses, e.g. natural grassland and agricultural grassland.

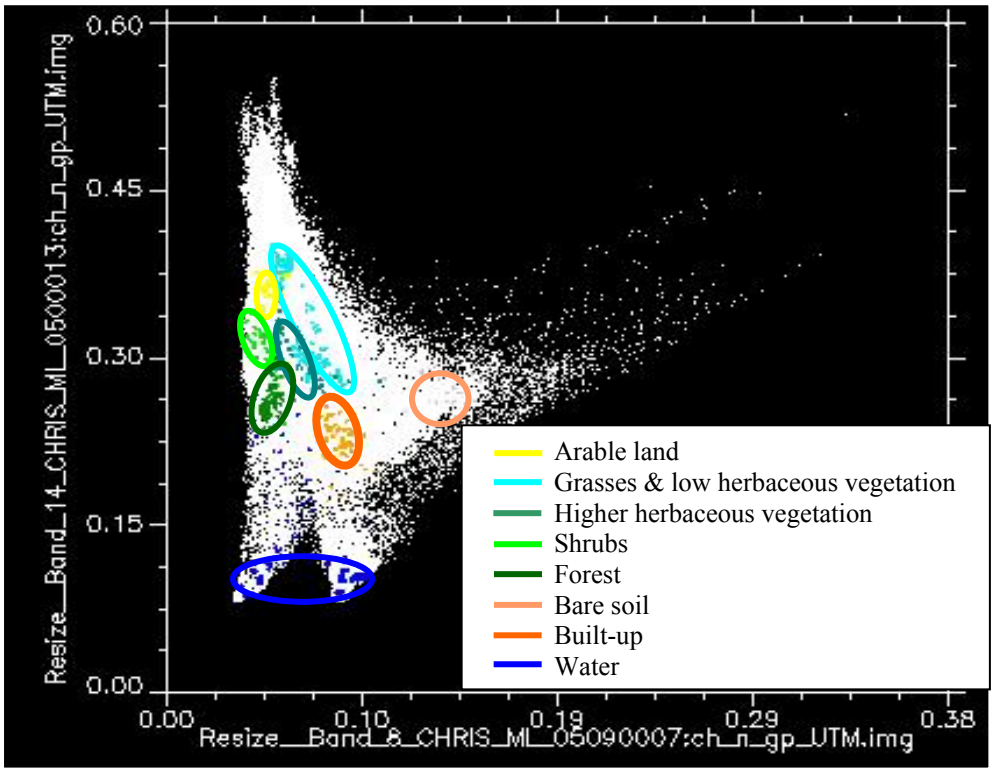

Figure 14: Feature space plot showing the spectral location of pixels that were chosen for each ROI within the nadir image of the Gelderse Poort that is used for classification. The association between the red band (band 8) on the x-axis and the NIR band (band 14) on the y-axis is presented here so the different spectral characteristics of each land use class become apparent.

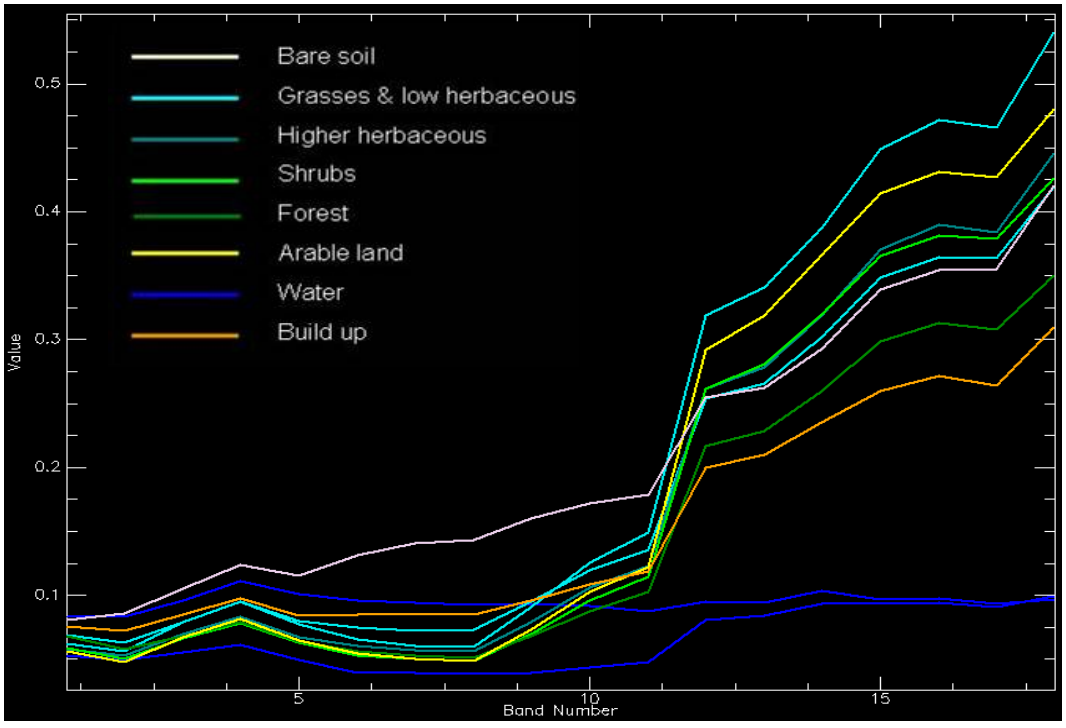

Figure 15: Spectral signatures of the ROI classes, belonging to a pixel from the ROIs in the feature space plot in figure 14, with on the x-axis the band numbers from the CHRIS sensor (bands 1-18) and on the y-axis the HDRF values.

Figure 16 shows the ecotope map of the river floodplains after classification of the CHRIS nadir image with the Maximum Likelihood classifier.

The largest area of the Gelderse Poort is covered by grasses and low herbaceous vegetation. The rest of the Gelderse Poort is mostly covered by agricultural fields, bare soils and higher herbaceous vegetation. Forests take up just a small part in Millingerwaard. Some other parts in and near Millingerwaard are covered by shrubs. Water is present in many parts of the floodplain area. Not many parts are indicated as built-up area.

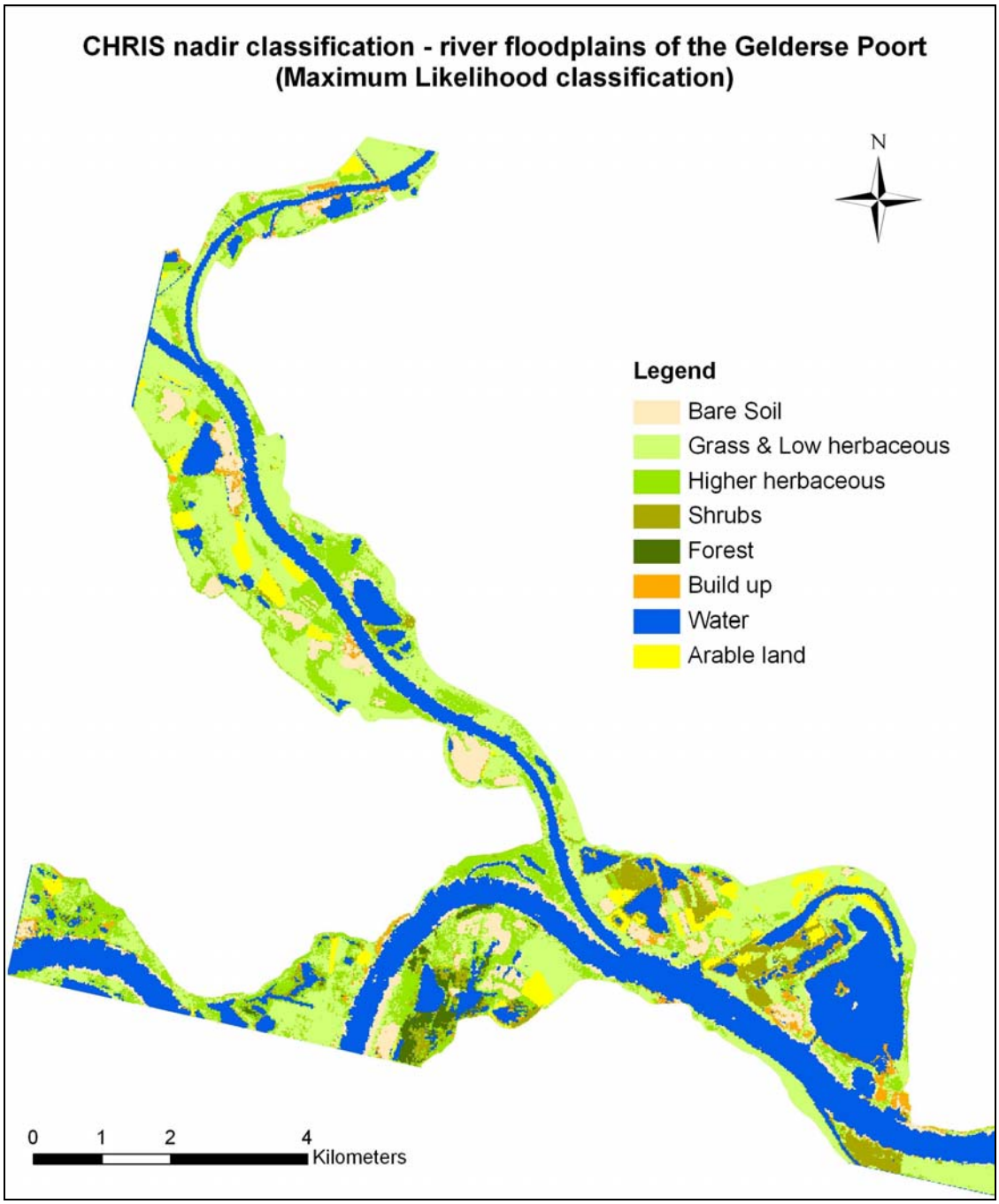

Figure 16: CHRIS ecotope map of the Gelderse Poort, created with maximum likelihood classification of the CHRIS nadir image using regions of interest.

Validation

Validation of ROIs

All of the pairs except for one have a separability value higher than 1.9. This means that the classes are statistically separated well. The arable land class even has a value of 2.0 in separation with built-up, forest, water and bare soil. Only the pair "higher herbaceous vegetation" and "grasses and low herbaceous vegetation" has a separability value of 1.71. This means that the spectral characteristics of these two classes are quite similar. This can be seen in the scatterplot of figure 14 where the classes almost overlap each other. In figure 15 two spectral signatures are plotted for grasses and low herbaceous vegetation. One of those signatures is very close to the signature of higher herbaceous vegetation. These signatures belong to pixels in the scatterplot in the part where the classes almost overlap. The other signature has higher reflectance values in the NIR. This signature belongs to a pixel in the upper part of the plotted ROI class for grasses and low herbaceous in figure 14. In appendix VIII the separability values for the pair separation of the ROIs in the CHRIS nadir image are presented.

Validation of the classified image

During field validation in the floodplains of Millingerwaard it was obvious that some parts of the class of higher herbaceous vegetation (on the classified CHRIS image) have moved up to the class of shrubs and the class of shrubs to the forest class. Furthermore, on some parts where the classification indicates bare soil there is water now.

Table 9 shows the confusion matrix for the maximum likelihood classification of the CHRIS nadir image and table 10 the measures of accuracy. The matrix is based on the 160 random sample points taken in the CHRIS image and in the aerial photograph (ground truth). The overall classification accuracy is 68.13% and the kappa coefficient is 0.56. The accuracies of the classes "arable land" and "built-up" are the highest and the accuracy of the class "grasses and low herbaceous" is the lowest. Sample points of other classes, especially "higher herbaceous" and "shrubs" are often misclassified into this class. The reliability, however, is highest for the class "grasses and low herbaceous". Pixels that are grass on the aerial photograph are also classified as grass in the Nadir image. Furthermore, the reliability of "forest", "arable land" and "water" is high. The reliabilities of "higher herbaceous vegetation" and "shrubs" are the lowest. These classes are often misclassified into "grasses and low herbaceous vegetation" and, in the case of shrubs, also in forest.

Table 9: Confusion matrix CHRIS nadir ML classification

Ground truth	Bare soil	Grass & low herbaceous	Higher herbaceous	Shrubs	Forest	Arable land	Water	Build up	Total
Bare soil	11		1		2			3	17
Grass & low herbaceous	3	19	6	5	1	3	1	1	39
Higher herbaceous		1	8	1				1	11
Shrubs			2	9	1				12
Forest			2	4	16		1	3	26
Arable land	1					17		1	19
Water	3		1	1			18		23
Build up	2							11	13
Total	20	20	20	20	20	20	20	20	160

Table 10: Accuracy CHRIS nadir ML classification

Classes	Accuracy (%)	Error of omission (%)	Error of commission (%)	Reliability (%)
Bare soil	64,71	35,29	45,00	55,00
Grass & low herbaceous	48,72	51,28	5,00	95,00
Higher herbaceous	72,73	27,27	60,00	40,00
Shrubs	75,00	25,00	55,00	45,00
Forest	61,54	38,46	20,00	80,00
Arable land	89,47	10,53	15,00	85,00
Water	78,26	21,74	10,00	90,00
Build up	84,62	15,38	45,00	55,00

Results and validation of the other CHRIS classifications

Table 11: Overall accuracy for the other CHRIS classifications
Stacked layers means a combination of bands 2-18 from the CHRIS nadir, -36, +36 VZA images

Input image	Classification method	Overall accuracy
CHRIS Nadir	Support Vector Machine	56,25%
CHRIS Stacked layers	Maximum Likelihood	44,38%
CHRIS Stacked layers PCA bands 1-3	Maximum Likelihood	55%
CHRIS Stacked layers PCA bands 1-4	Maximum Likelihood	56,25%
CHRIS Stacked layers PCA bands 1-5	Maximum Likelihood	58,13%

The results from the other classification methods are less good than the results from the CHRIS nadir classification with the ML classifier. In table 11 the overall accuracies are given for those classifications. The maps and accuracy matrices of the other classifications can be found in appendix IX.
The SVM method did not improve the results compared to the ML method. The classified image (appendix IX) shows misclassifications in built-up areas that are placed along the borders of the river and the lakes. The classification of the CHRIS image with stacked layers, using the ML classifier, performed worst with an overall accuracy of only 44%. As is noticeable in appendix IX, many parts of the image are classified as water. Also, the vegetation classes do not come out as they should. Too many parts are classified as high herbaceous vegetation, but are in fact shrubs or forest. The classifications of the stacked layers CHRIS image with PCA has better results. All of these images were classified with the maximum likelihood method. When using the first 3 PCA bands, the overall accuracy is 55%. The overall accuracy improves when more PCA bands are chosen. With 4 PCA bands, the overall accuracy is 56% and with 5 PCA bands 58%. On the classified *PCA*-band images the parts along the river borders are also classified as built-up area.

4.1.3 Comparison of CHRIS classification with RWS classification

CHRIS nadir classification (ML) **RWS classification**

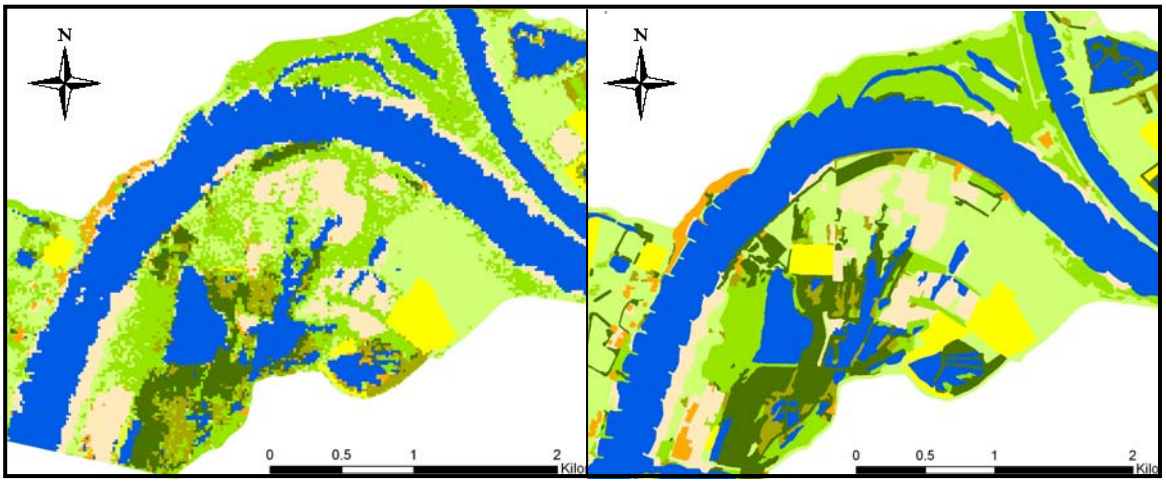

Figure 17: Ecotope maps of Millingerwaard obtained by maximum likelihood classification of the CHRIS nadir image and reclassification of the RWS ecotope map.

In figure 17 the images of the RWS classification and the best results for the CHRIS classification (CHRIS – nadir – ML) are shown together.

The RWS classification has a higher overall accuracy (80%) than the CHRIS classification (68%). As can be seen in the classifications of Millingerwaard in figure 17, the RWS classification shows more details in the classes. It shows for example small lines of forest (in the north, near the river) and small areas of shrubs. But the CHRIS image is more detailed in showing the classes on a pixel basis. For example, within the parts of higher herbaceous vegetation, there are some pixels of low herbaceous vegetation.

4.2 Vegetation structure properties

4.2.1 LAI

4.2.1.1 Millingerwaard

LAI -36 VZA (figures 18 & 19)
Most LAI values range from 1 to 4.5, with a peak at 2.5 (figures 18 and 19). The LUT values for LAI range from 1-7, with a step of 0.5; and from 7-12 with a step of 1. Every possible LUT value is present in the map, but from 5 until 12, the frequencies are lower, with an exception at value 10. This second peak at 10 represents the rectangular shaped arable fields. The higher LAI values around 6-7 and at 12 belong to parts west of the lake. These parts consist of natural vegetation with a lot of appearing high grasses, small shrubs and some scattered bushes. Those higher values can also be seen in some forest parts in the middle and south of Millingerwaard and along the winter dike. There is a gradient in the map with subtle differences in LAI values. Even in the rectangular agricultural field in the east some variation in values are discernable.

LAI nadir VZA (figures 20 & 21)
The distribution of LAI values is more or less the same as for the backward scattering direction (figures 20 and 21). Most values are ranged between 1 and 4.5, with a peak at 2.5. There is also a second peak at 10 and a lower frequency for the other values between 6 and 12. However, not all possible LUT values occur in the image. The higher LAI values are located in the same places as on the map for the backscattering direction: next to the lake, in the forested areas in the middle and south of the image, in the arable fields and along the winter dike in the south. The difference with the backward scattering direction is that less of a gradient can be seen in LAI values.

LAI +36 VZA (figures 22 & 23)
Most LAI values in the forward scattering direction are again in-between 1 and 4.5, but there is not a natural curve in the histogram like in the histograms of the backward scattering and nadir direction (figures 22 and 23). There is a small peak at 2.5. Furthermore there is a high frequency at 6 and 6.5. This indicates the same parts on the map as where the peak value of 10 is in the nadir and backward scattering direction: the value of 6 belongs to the natural grasslands west of the lake and the value of 6.5 belongs to the arable land. There are also some values of 12 in the forest and shrub areas in Millingerwaard. There is not so much gradient in LAI values compared to the backward scattering map and the values from 7 to 11 are not included. No subtle differences can be discerned in the image. Large parts, like the part next to the lake, received high values.

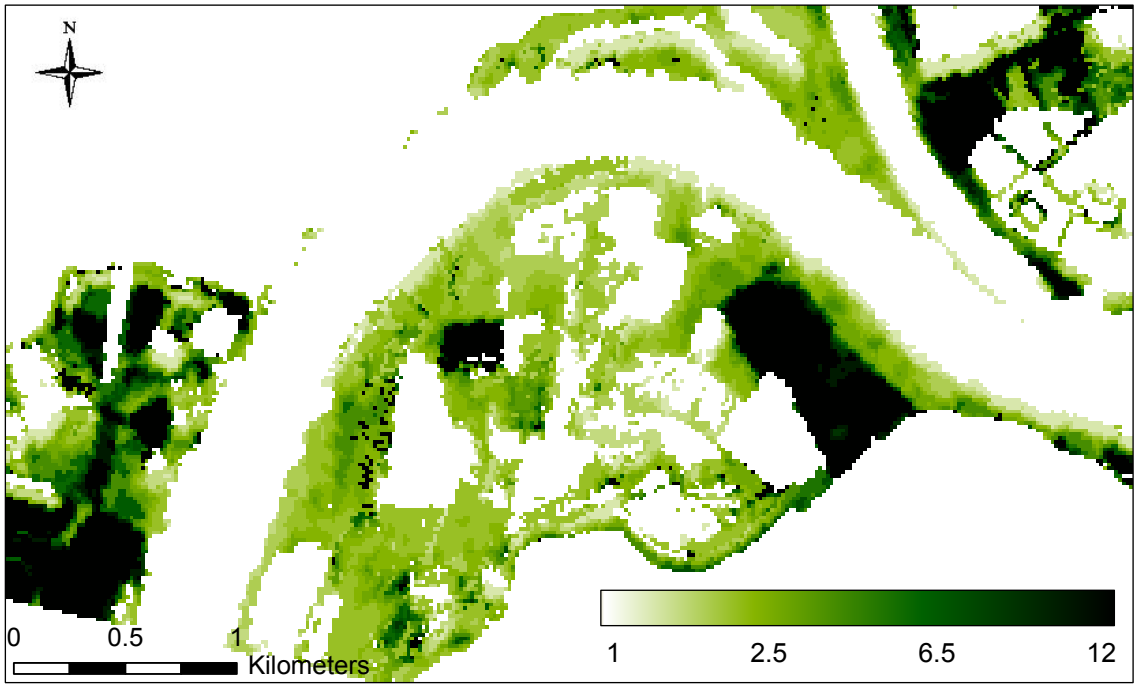

Figure 18: LAI map of Millingerwaard for the backward scattering direction (VZA -36).

NB: the values at the colour scale bar in the 2nd and 3rd position (here: 2.5 and 6.5) differ for each colour map in paragraphs 4.2.1.1-4.2.2.2. This is because of the different ranges of values that are present in each map.

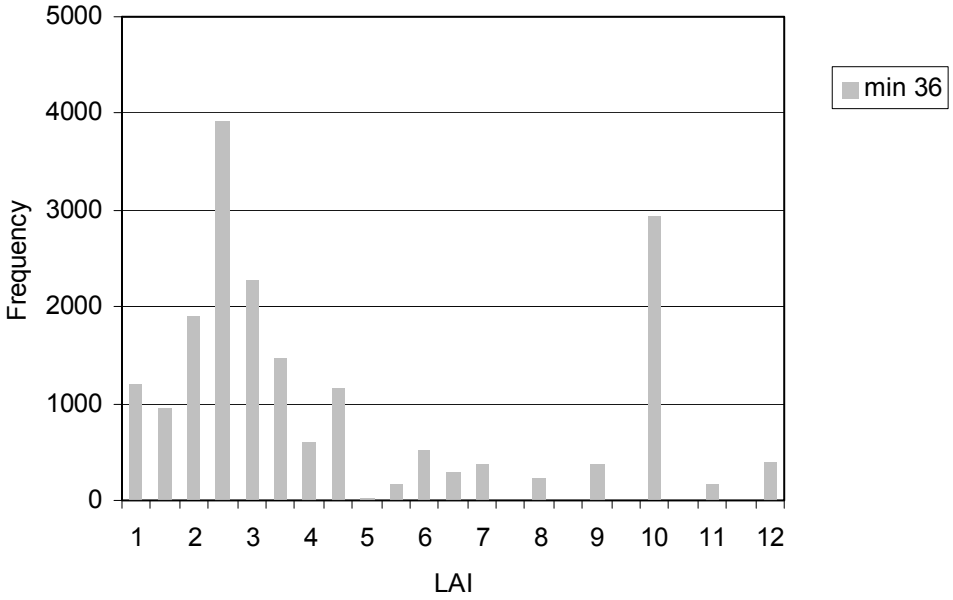

Figure 19: Histogram of LAI for all classes in Millingerwaard for the backward scattering direction.

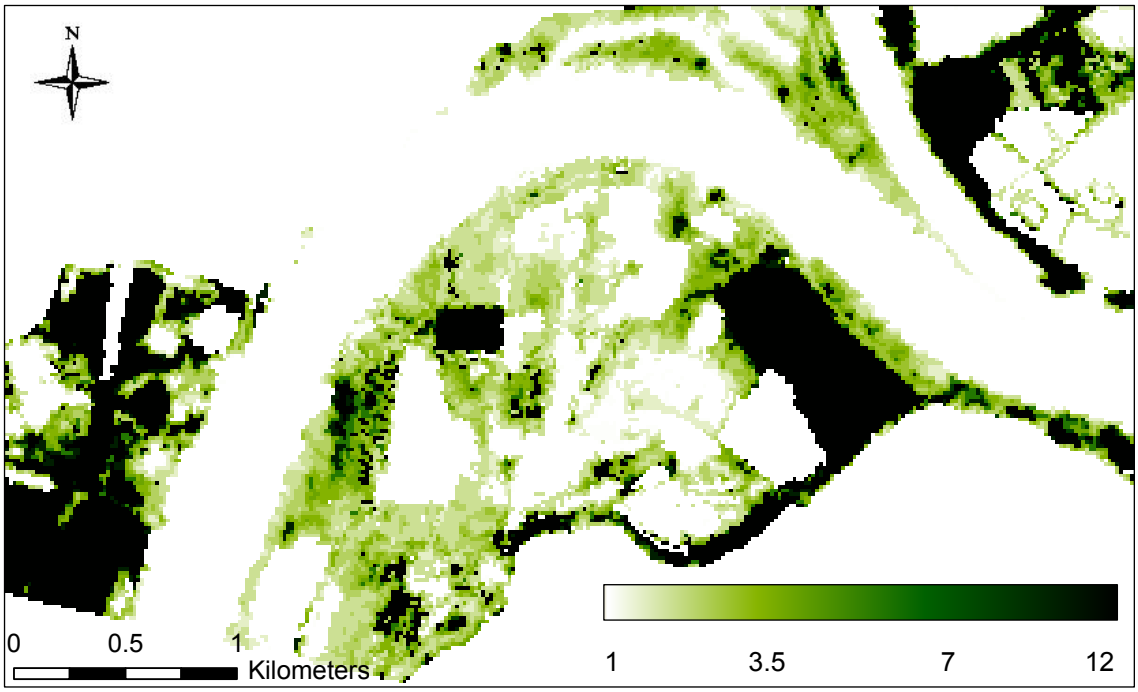

Figure 20: LAI map of Millingerwaard for the nadir direction.

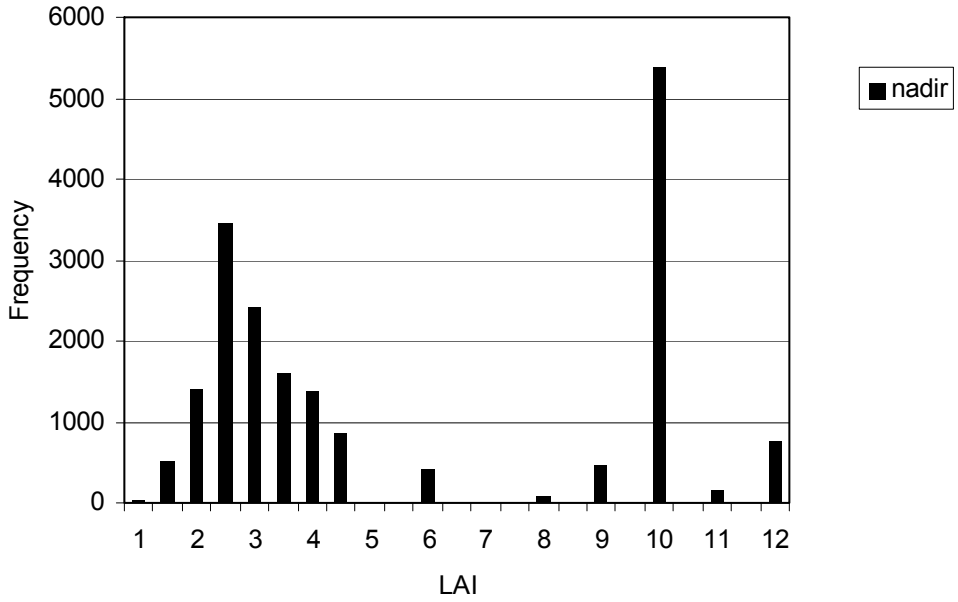

Figure 21: Histogram LAI for all classes in Millingerwaard for the nadir direction.

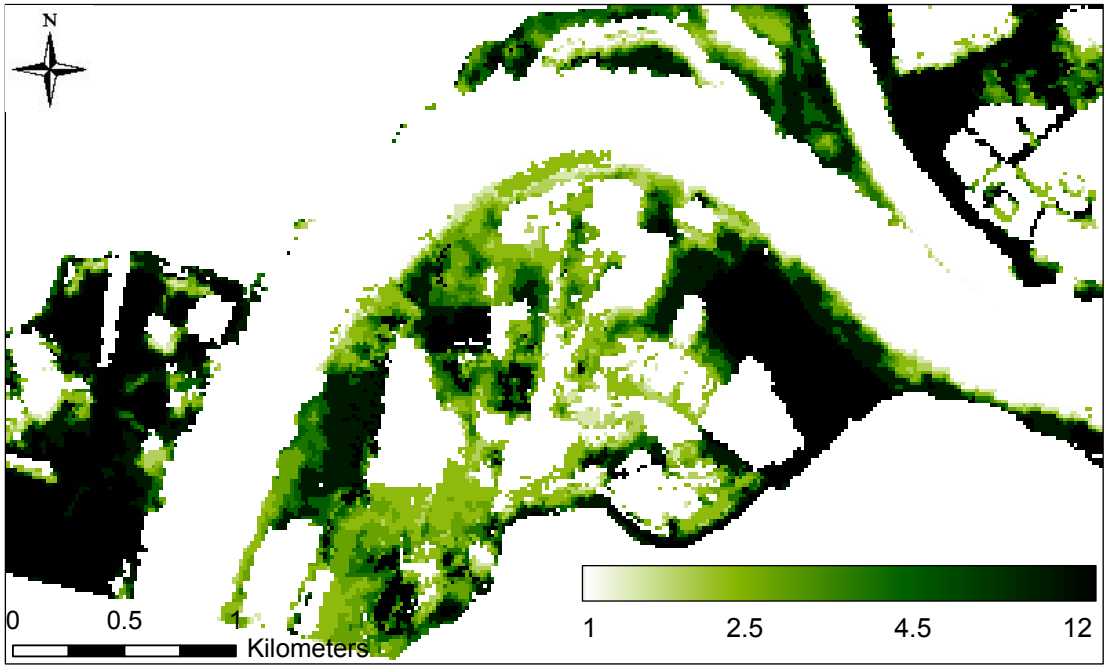

Figure 22: LAI map of Millingerwaard for the forward scattering direction (VZA +36).

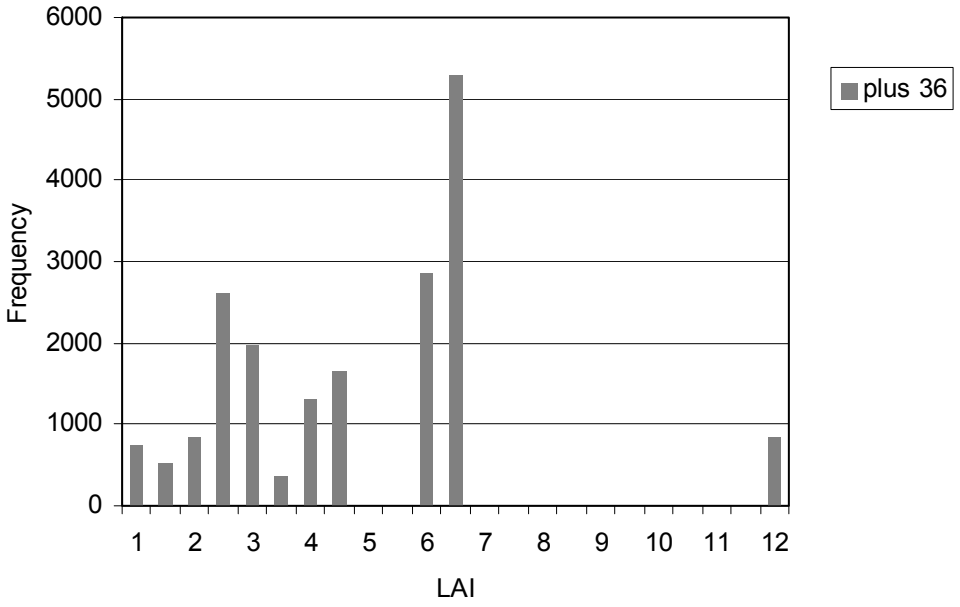

Figure 23: Histogram of LAI for all classes in Millingerwaard for the forward scattering direction.

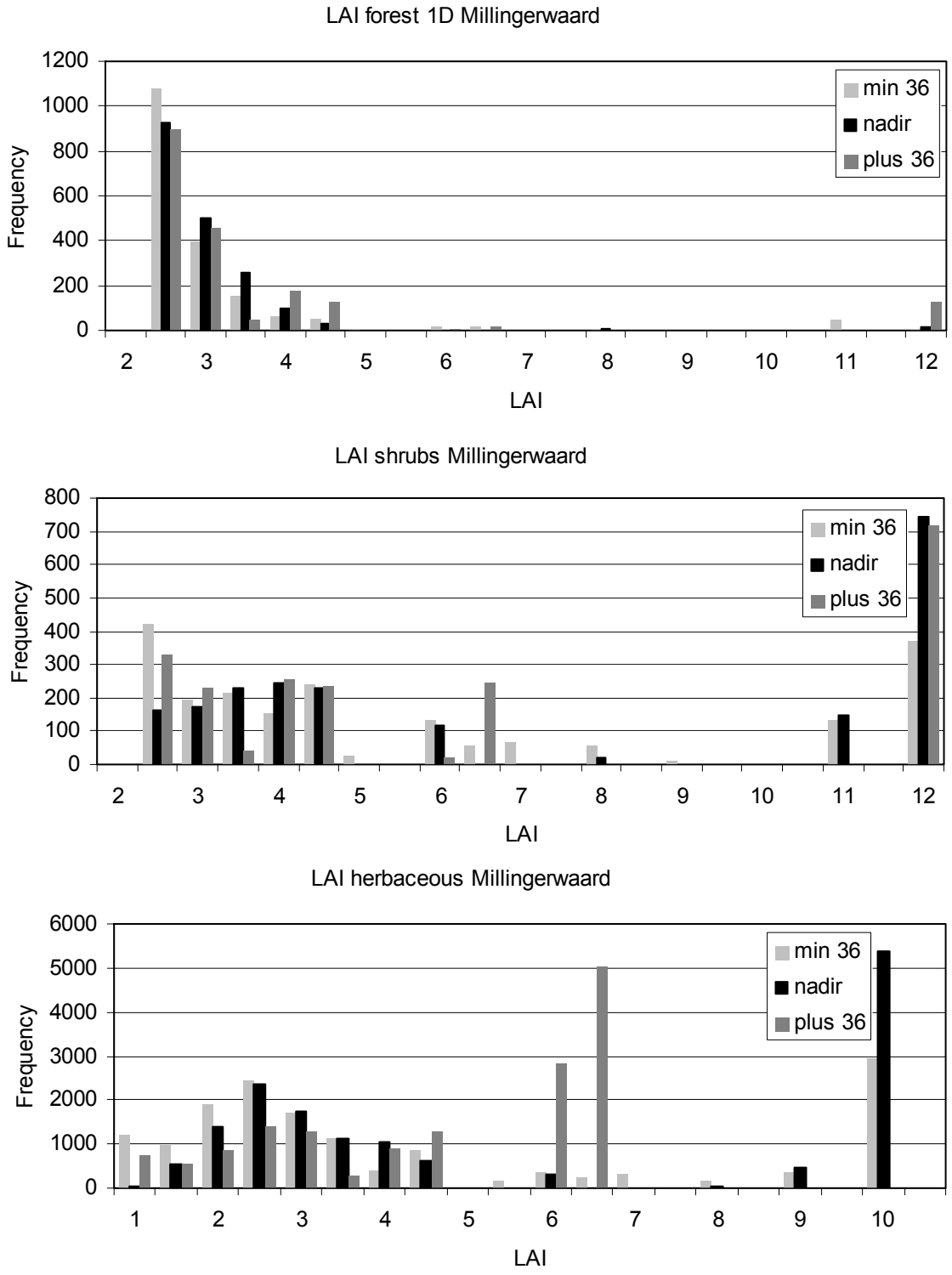

Figure 24: Histograms of LAI for the forest class (modelled as 1D medium), the shrub class and the herbaceous class in Millingerwaard for all 3 viewing directions.

Figure 24 shows the LAI histograms separately for each vegetation structure type. All three angles show the same trend of how the LAI values are distributed within the lower ranges from 1-5. However there are some small differences in frequencies within this range and also in the higher ranges of values.
In the forest class almost all values range from 2.5 until 4.5. LAI of 2.5 has the highest frequency for all scattering directions, the frequency decreases with higher LAI values. There are some LAI values around 6 and 12. LAI of 2.5 has the highest frequency in the backward scattering direction; LAI of 3 and 3.5 has the highest frequency in the nadir direction. LAI of 4 and 4.5 has the highest frequency in the forward scattering direction.
For the shrub class most values are also in-between 2.5 and 4.5, but there are also quite high frequencies around 6, 7 and 11 and a high peak at 12. In the forward scattering direction, LAI values do almost not occur in the higher ranges, except at the value of 12. The LAI values for the backward scattering direction are distributed over more classes than for the nadir and forward scattering direction.
Most LAI values in the herbaceous class range from 1 until 4.5 for all three scattering directions. The LAI value of 1 has a very low frequency for the nadir direction; the backward and forward scattering directions have a higher frequency at 1. At 6 and 6.5 there are peaks in the forward scattering direction. At 9 there are some values covered by the nadir and backward scattering direction and at 10 there is a peak in the nadir and backward scattering direction. LAI values of the backward scattering direction occur at almost every possible LUT value.

Forest was modelled as 1D medium, because this gave better results than with an explicit 3D geometric shape. As an example, in appendix X, the results for forest modelled as 3D medium are presented for the nadir viewing direction. There is not much variation in LAI values. This is also pronounced in the histogram in appendix X, where the LAI values for the forest class in all three viewing directions are given.

4.2.1.2 Gelderse Poort

The LAI modelling results for the river floodplains of Gelderse Poort as spatial subset are more or less the same as for Millingerwaard. The maps and histograms for the backward scattering direction are shown in figures 25 and 26. The results for the nadir and forward scattering direction are presented in appendix XI. The high peaks at values 10 for backward scattering direction are much higher compared to those peaks for Millingerwaard. This means that there are many arable fields along the river floodplains in the Gelderse Poort; they have a very dark colour. Similar peaks can be seen in the nadir and forward scattering direction, respectively at 10 at 6-6.5. The peaks at 2.5, however, are less expressed than for Millingerwaard. The distribution of the rest of the values is similar to the distribution of values for Millingerwaard. The histogram for the backward scattering direction covers all possible LUT values, the nadir histogram has the same shape as the backward scattering histogram, but does not cover all values. The histogram for the forward scattering direction has an irregular shape and no values between 7 and 11.

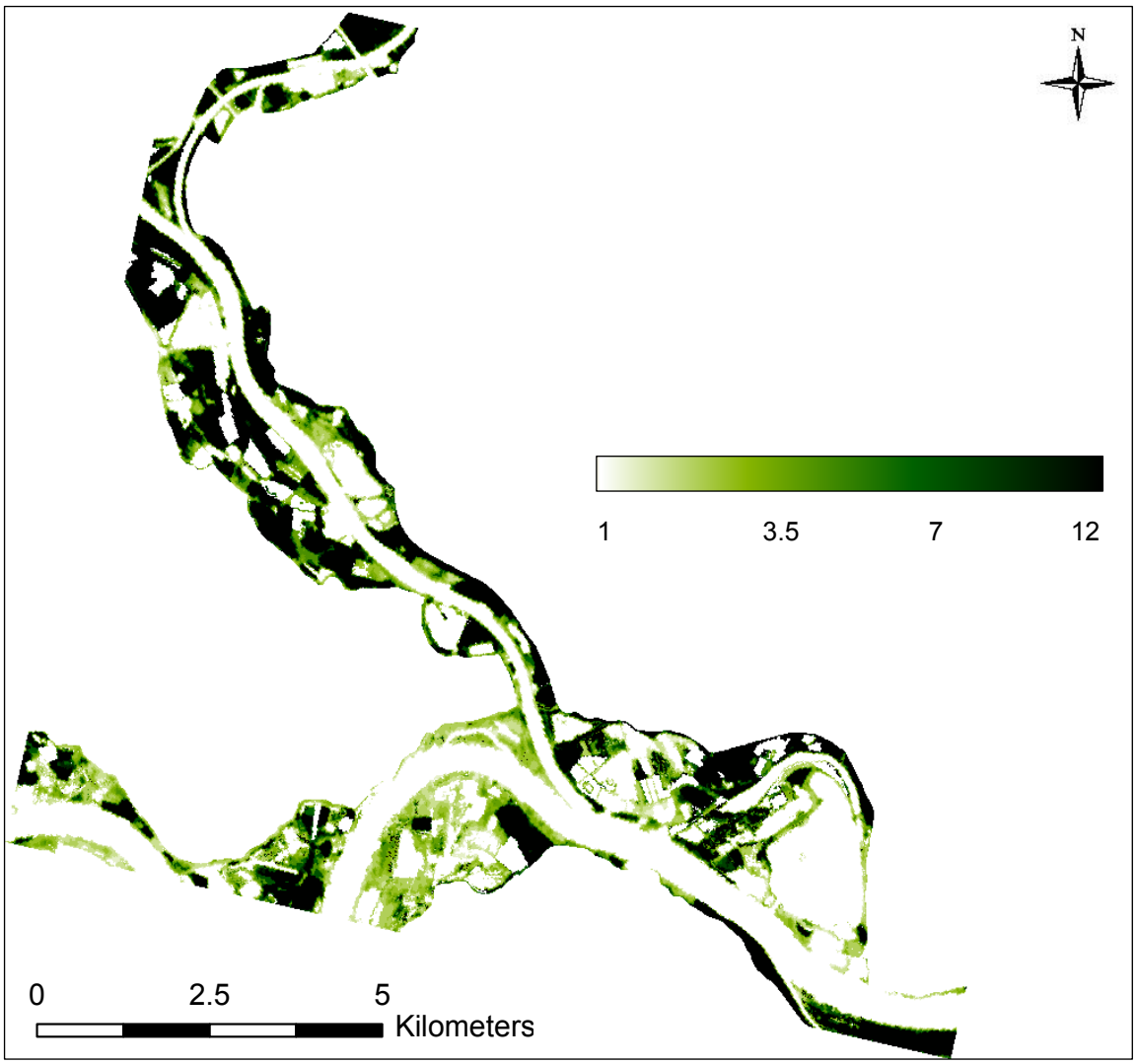

Figure 25: LAI map of the Gelderse Poort for the backward scattering direction.

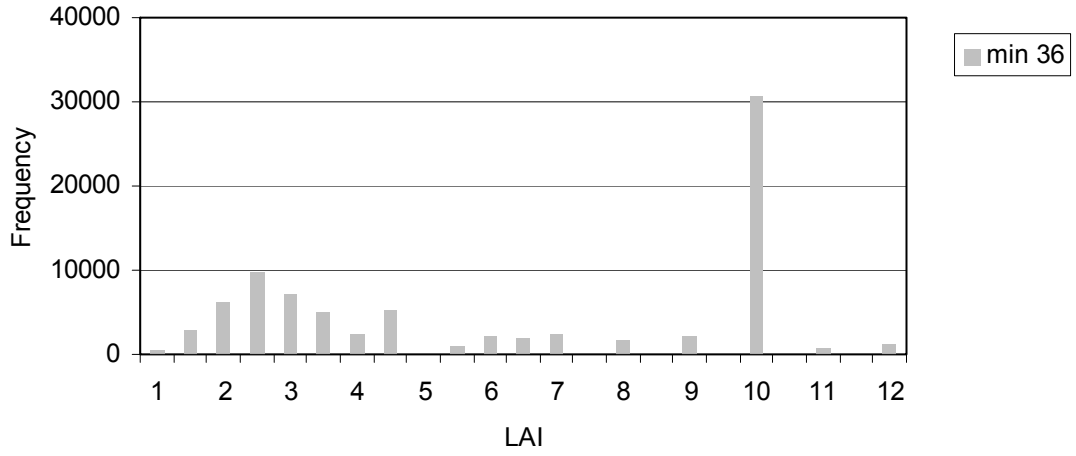

Figure 26: Histogram LAI Gelderse Poort for the backward scattering direction.

4.2.2 fCover

4.2.2.1 Millingerwaard

The fCover maps look much more granulated than the smooth-looking LAI maps. The map and histogram of the backward scattering direction (figures 27 and 28) show almost no values of 0.6 and 0.65. Most values are evenly distributed between 0.7 and 1. The highest fCover values of 0.95 and 1 belong to the arable field in the northeast of Millingerwaard. Some parts within the forest and natural grassland and along the winter dikes also received high values. Lowest values are present in the parts that contain bare soil or pioneer vegetation, in the north of Millingerwaard.

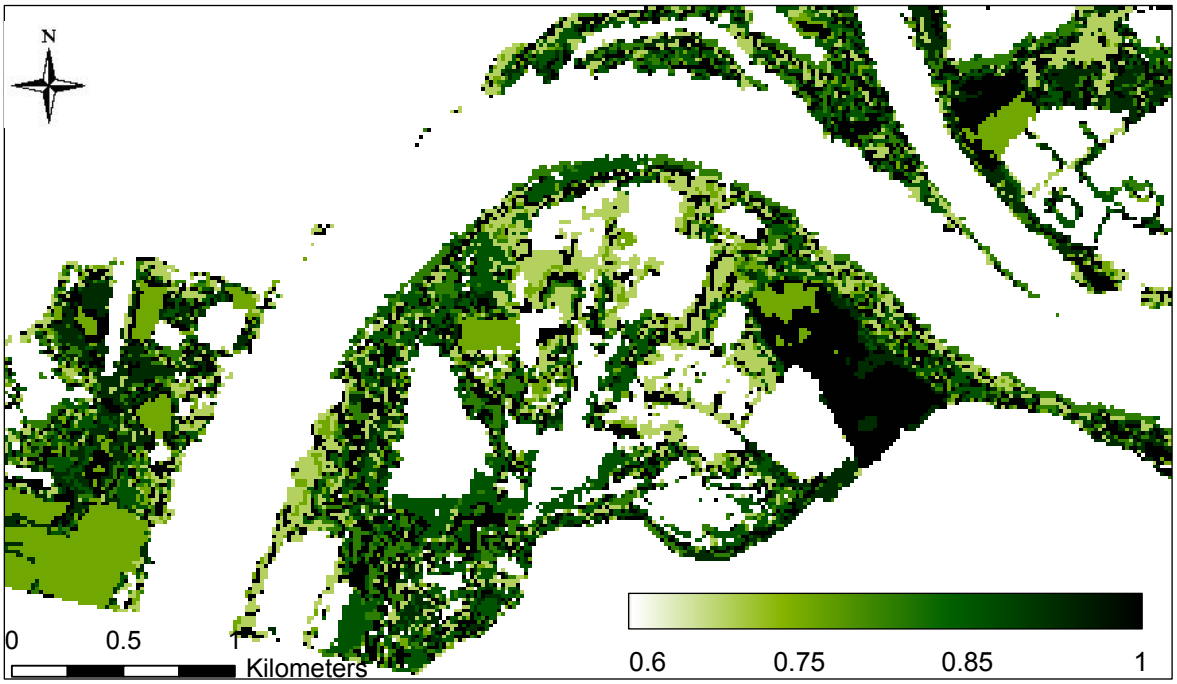

Figure 27: fCover map of Millingerwaard for the backward scattering direction.

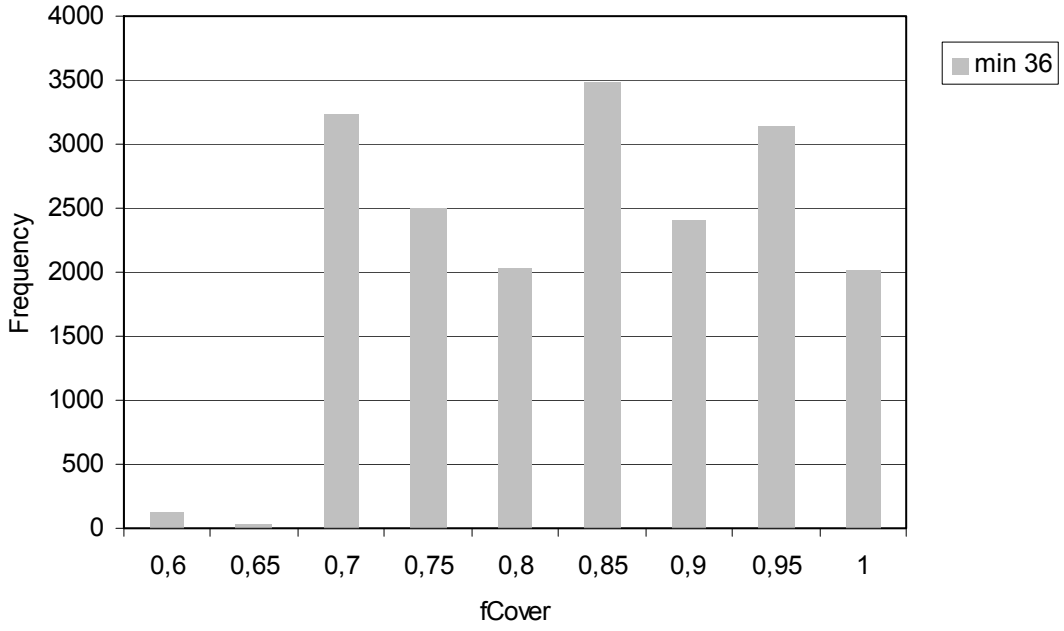

Figure 28: Histogram of fCover for all classes in Millingerwaard for the backward scattering direction.

Figures 29 and 30 show the fCover map and histogram for the nadir viewing direction. The fCover values of 0.6 and 0.65 have a low frequency. Then there is a small peak at 0.7. The right part of the histogram is bell-shaped with a peak at 0.85. Highest values are scattered through the whole image. The value of 0.7 belongs to pixels in the natural grassland in the north and west of Millingerwaard and the peak at 0.85 belongs to pixels in the arable fields.

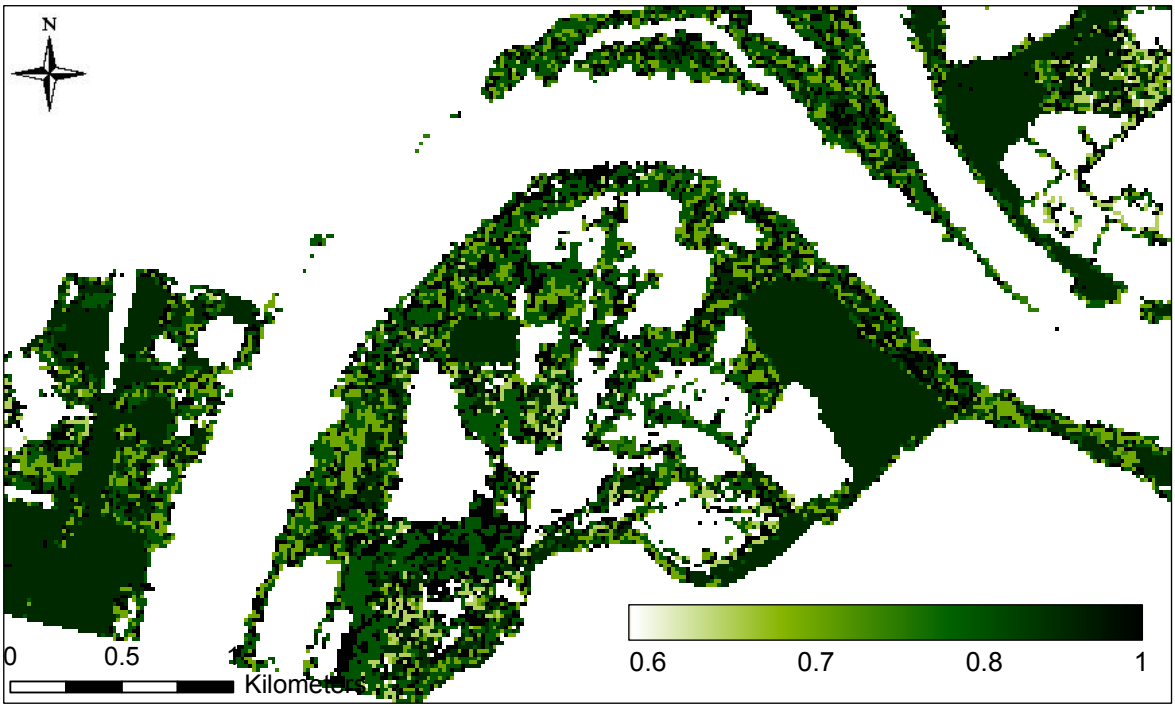

Figure 29: fCover map of Millingerwaard for the nadir direction.

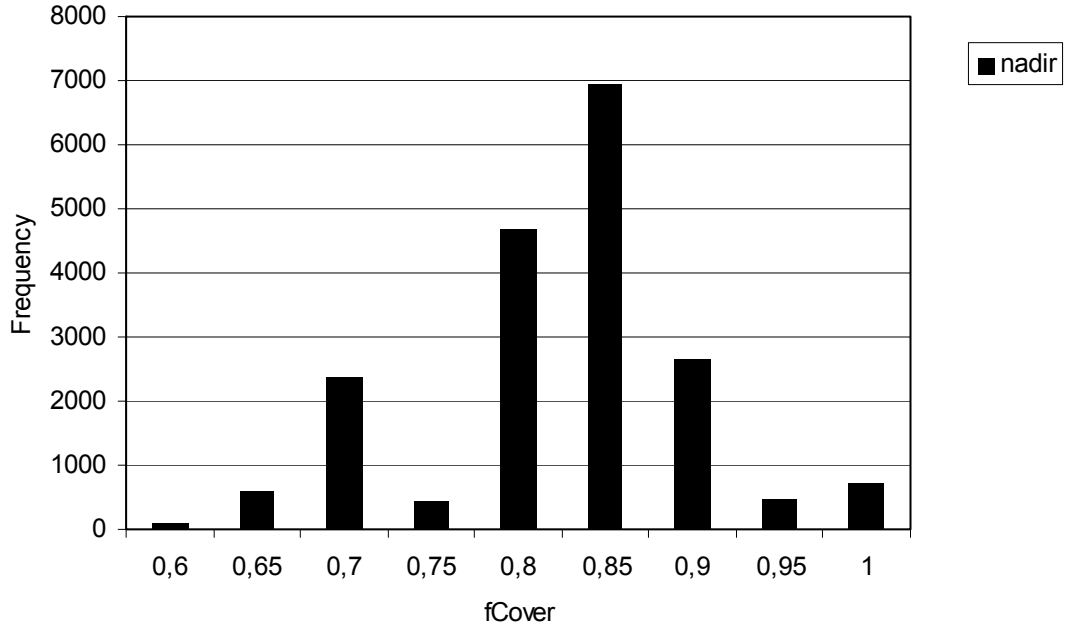

Figure 30: Histogram of fCover for all classes in Millingerwaard for the nadir direction.

What is striking for the forward scattering direction (figures 31 and 32) is that most pixels received the highest possible fCover value of 1. This is not only the case for the arable fields, but also for the natural grasslands west of the lake. The rest of the values is irregularly distributed between 0.7 and 0.95. The highest values belong to the arable land, the natural grasslands west and north of the lake, the forest south of the lake and along the winter dike in the south of Millingerwaard. The lowest values belong to the parts that are bare or pioneer vegetation, in the north of Millingerwaard.

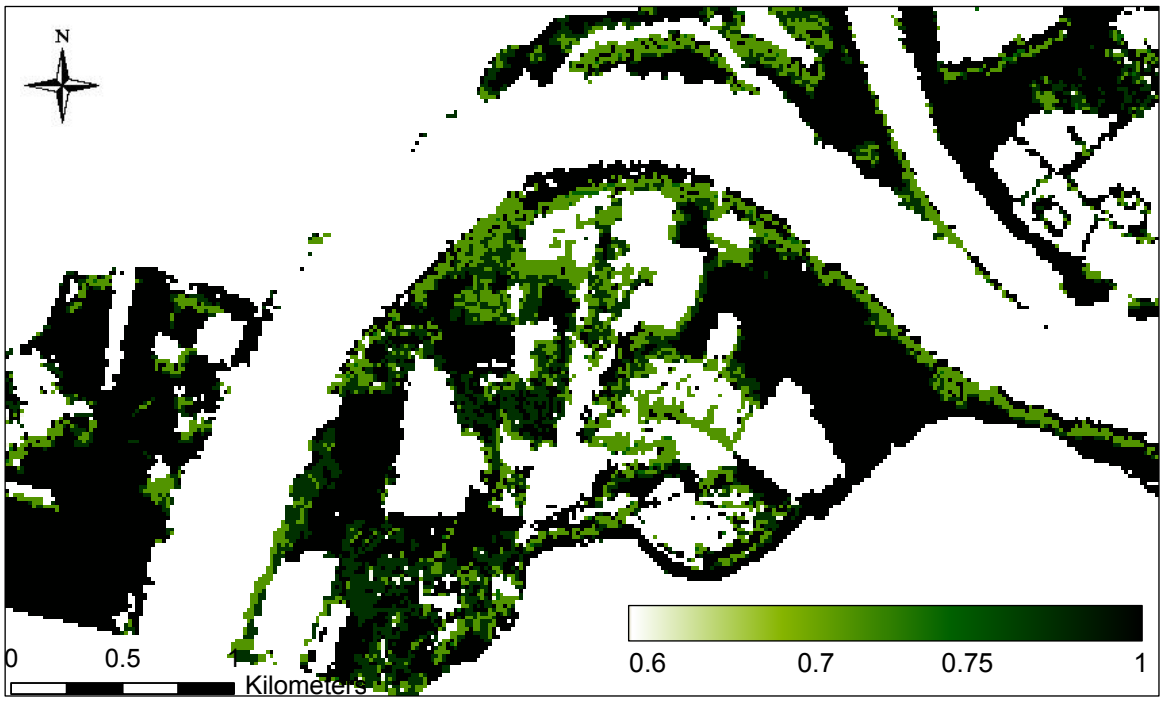

Figure 31: fCover map of Millingerwaard for the forward scattering direction.

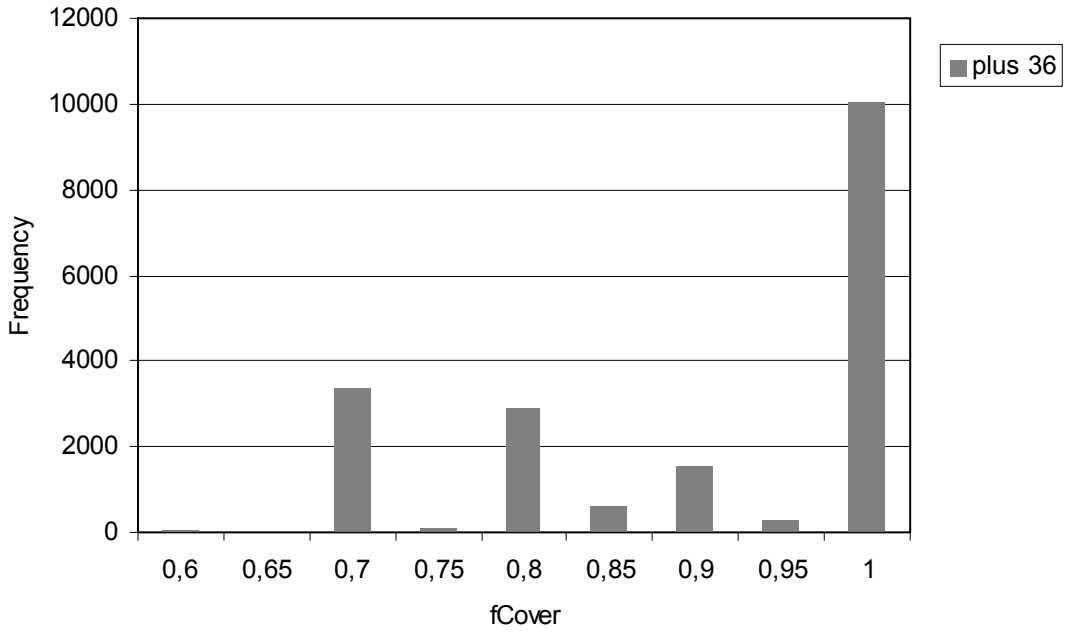

Figure 32: Histogram of fCover for all classes in Millingerwaard for the forward scattering direction.

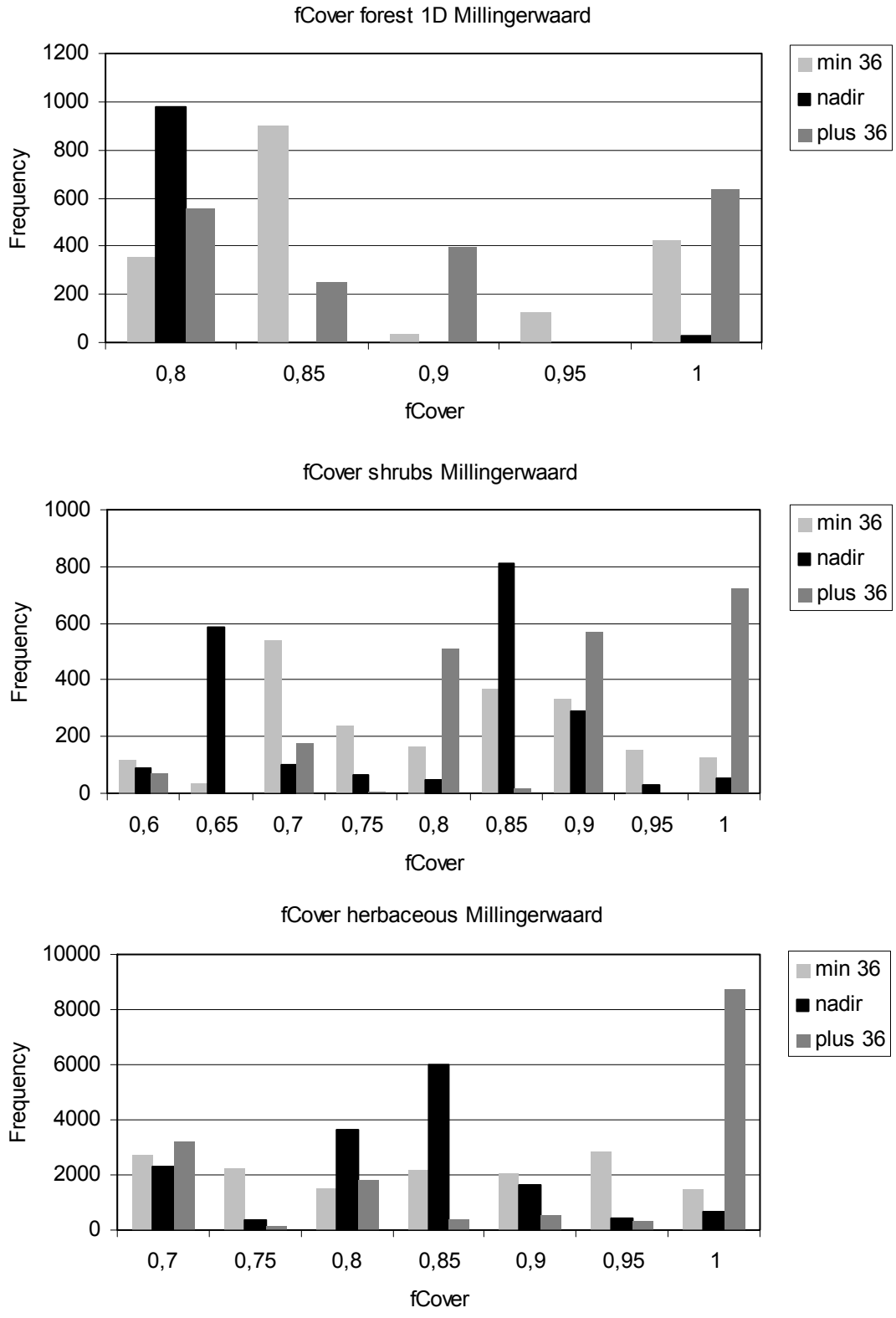

Figure 33: Histograms of fCover for the forest class (modelled as 1D medium), the shrub class and the herbaceous class in Millingerwaard for all 3 viewing angles.

Figure 33 shows the histograms of fCover in Millingerwaard separately for the three vegetation structure types.
For the forest class, the highest frequency of fCover values in the nadir direction is at 0.8. The highest frequency of the backward scattering direction is at 0.85. For the forward scattering direction, the highest frequency is at 1. The backward scattering direction has a frequency at all possible fCover LUT values. The nadir direction only has a frequency at values 0.8 and 1. The values in the forward scattering direction are more evenly distributed among the fCover values.
For the shrub class there are two peaks in the nadir direction at 0.65 and 0.85. The rest of the nadir fCover values are distributed among the other classes. The highest frequencies for the backward scattering direction are at 0.7 and also at 0.85 and 0.9. The fCover values occur in all classes. The forward scattering direction has peaks at higher fCover values of 0.8, 0.9 and 1.
The herbaceous class has a high frequency of fCover values in the nadir direction at 0.8 and 0.85. The peak for the forward scattering direction lies at 1. The fCover values for the backward scattering direction are distributed quite evenly over all the fCover classes.

4.2.2.2 Gelderse Poort

The map and histogram in figures 34 and 35 show the distribution of fCover values derived from the backward scattering direction for the whole Gelderse Poort area. The results are similar to the results of Millingerwaard. Although, there are higher peaks and lower dips in the histogram. There are almost no fCover values of 0.6 and 0.65.

The results for the nadir and forward scattering direction are displayed in appendix XII. The results for the nadir direction are similar to those of Millingerwaard. There are almost no fCover values of 0.6 and 0.65. The results for the forward scattering direction are also similar to those of Millingerwaard. Only, the frequency for the fCover value of 1 is much higher in the Gelderse Poort.

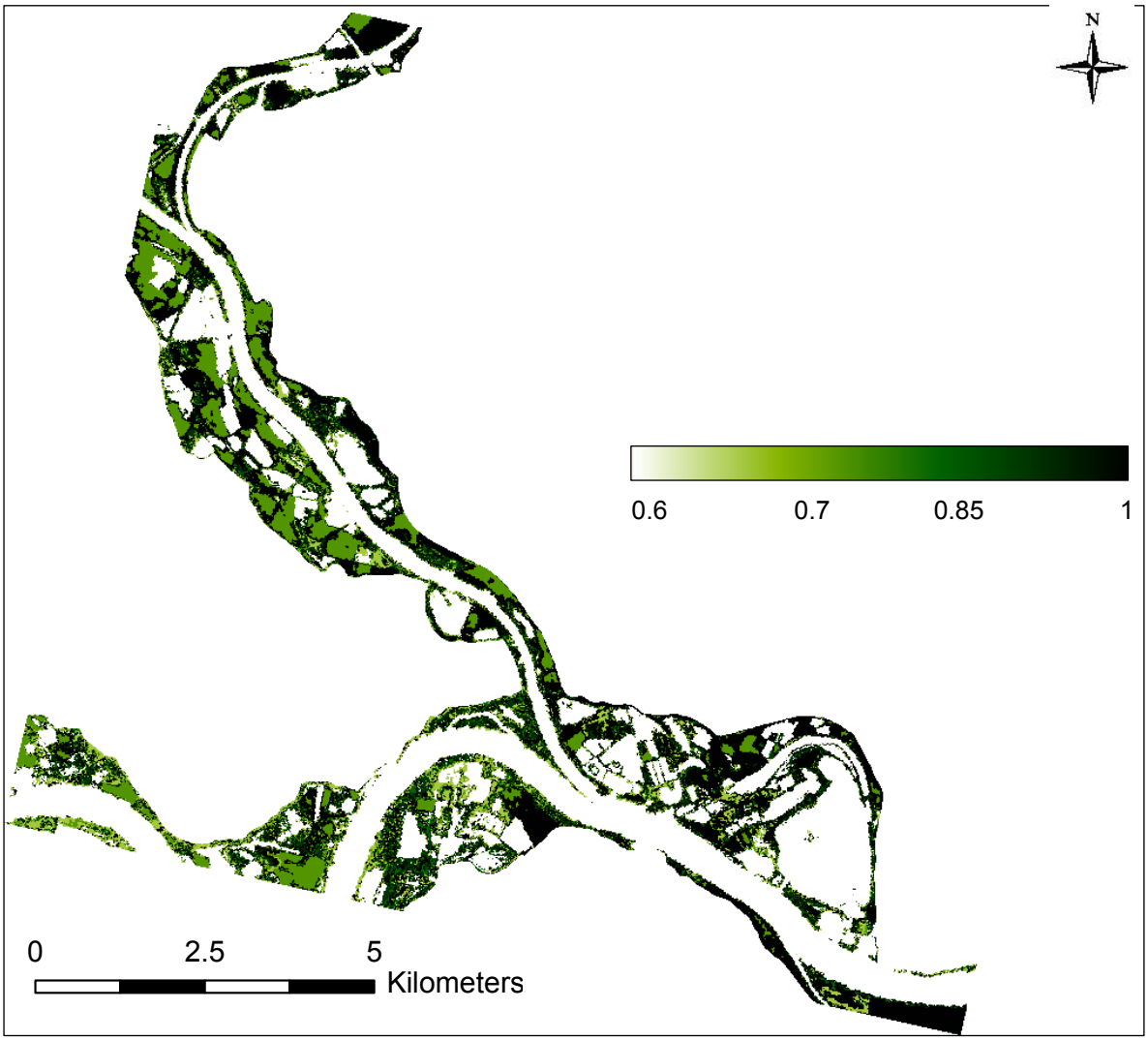

Figure 34: fCover map of the Gelderse Poort for the backward scattering direction.

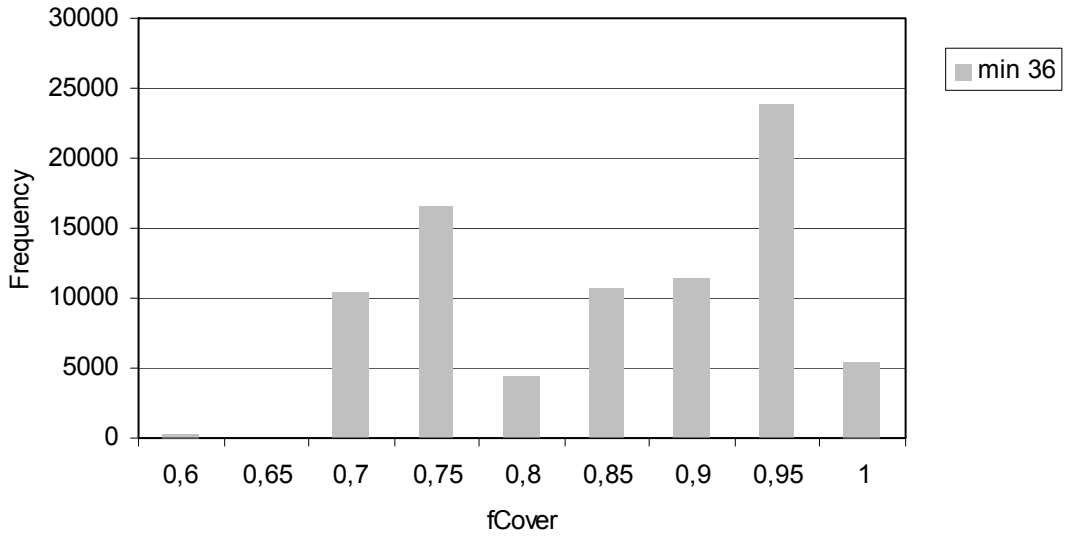

Figure 35: Histogram fCover Gelderse Poort for the backward scattering direction.

4.2.3 PV

The model outcome of PV did not show any variation with the RMSE method. The PV received the minimum LUT-value that was available for each vegetation structure type. For the forest and shrub class this was 0.7 and for the herbaceous class this was 1. If you allow the LUT to have a larger range of PV values, for example 0.5-1, than PV again receives the lowest possible value, which is in this case: 0.5.

4.2.4 Validation of LAI with field data from 2004 and 2005

4.2.4.1 Validation of LAI with field data from 2004

Figure 36 shows scatter plots of the modelled and measured LAI values from the field campaign of 2004. All validation points are located in forest areas (appendix VI). The black dots represent validation points that have a poor correlation and were not included for the linear regression.
The blue line is the linear regression line that belongs to the blue dots: the validation points that were used for linear regression. The ranges of values of the modelled and measured LAI are the same with values in-between 2.5 and 4. Overall the modelled LAI is a little bit lower than the measured LAI, but all values still lie close to the 'x=y'-line, which is the ideal line for regression. If all points fell on the 'x=y'-line, the modelled and measured values would be the same. The R^2 is the highest in the nadir and forward scattering (plus 36) direction. The linear regression line from the nadir scatter plot is very close and almost parallel to the 'x=y'-line.
Two of the black dots (validation points 3 and 9: appendix VI) occur in all three observation angles. The modelled LAI for these two points is lower than the measured LAI and the difference is larger in comparison to other validation points. A reason for this could be that the forest area is quite heterogeneous. As a CHRIS pixel is ± 17 m^2, the modelled LAI is an average value for the whole pixel; the forest surrounding the exact measurement location is also taken into account. Therefore the modelled LAI can have a different value than would be expected for the exact measurement location. Another reason could be that those points are outliers because of measurement inaccuracies. The 3rd black dot (validation point 10: appendix VI) is only present in the nadir direction. This validation point has a relatively high modelled LAI value. In the other two directions the modelled value of this point is much lower. So probably it is because of a modelling uncertainty that this point has such a high value in the nadir direction. Those three points are considered as outliers and are therefore excluded from the validation analysis. They would change the direction of the linear regression line and the R^2 considerably. Excluding them from further analysis will give a more realistic validation result.

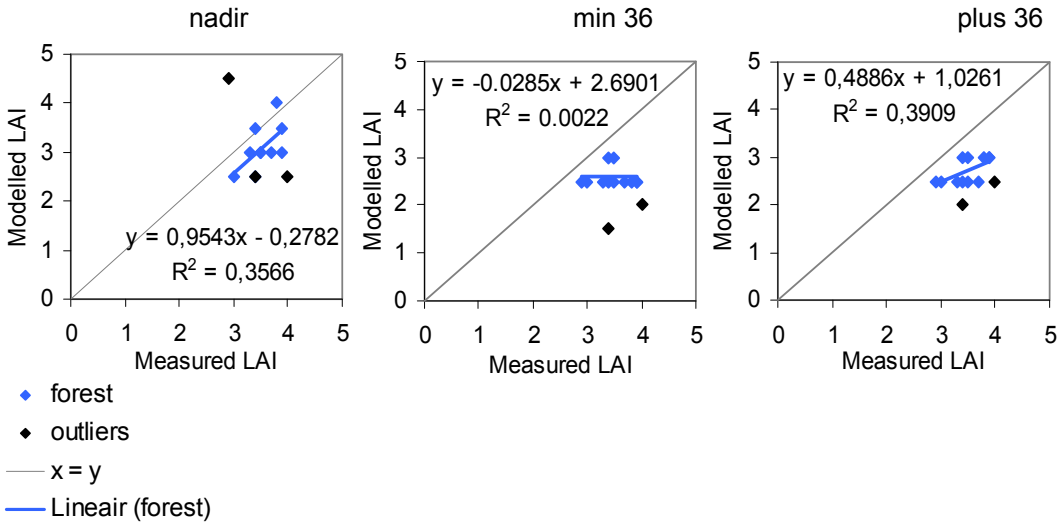

Figure 36: Scatter plots showing the correlation between the modelled LAI for the 3 viewing angles and the measured LAI that was obtained with the hemispherical camera for 13 validation points in 2004. The linear regression functions and R^2s are plotted in the graphs.

Cross validation

The modelled LAI outcomes for all 3 observation angles lie within the same range of values; between 1.5 and 4.5 (figure 37). The modelled LAI values in the back scatter (VZA -36) and forward scatter (VZA +36) directions are lower than in the nadir direction. The LAI values in the backscatter and forward scatter direction are very similar. The scatter plot in figure 37 shows a higher correlation between those two observation angles than in the scatter plots with the nadir direction. The points lie almost on the 'x=y'-line and the R^2 is relatively high: 0.56.

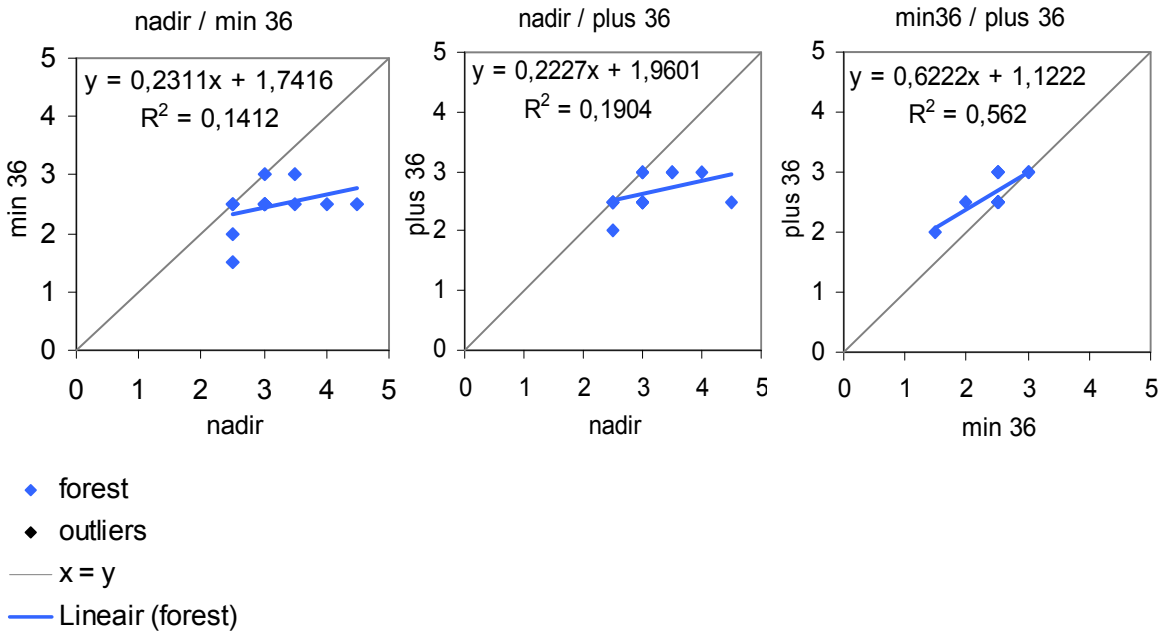

Figure 37: Scatter plots showing the cross validation results of the modelled LAI outcomes for the 3 different viewing angles for the 13 validation point locations of 2004.

NB: some points have the same value in this graph: so 5 blue dots represent 13 validation points.

4.2.4.2 Validation of LAI with field data from 2005

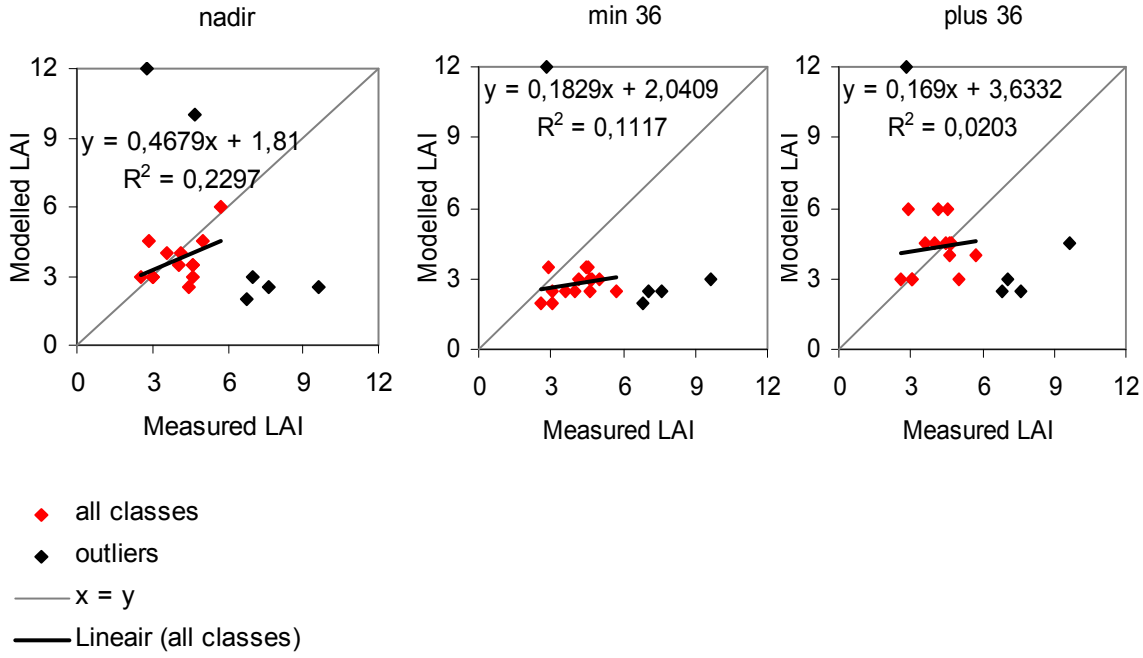

Figure 38: Scatter plots showing the correlation between the modelled LAI for the 3 viewing angles and the measured LAI that was obtained with the hemispherical camera + TRAC for 19 validation point locations of 2005. The linear regression functions and R^2s are plotted in the graphs.

The scatter plots in figure 38 contain the modelled and measured LAI values for the validation points from 2005. Red points represent dots from all the measured classes (herbaceous, shrubs and forest); black dots represent the points that were excluded from validation analysis.
The four black dots in the bottom of the graphs occur in all three observation directions. These points represent GH1, FR17, FR18 and FR19; 1 validation point in the grasses & herbaceous class and 3 validation points in the forest class (for exact location, see appendix VII). These points probably have inaccuracies in the field measurements, because the measured value is much higher than the average measured value of the other points. On the aerial photograph, the vegetation composition looks similar to the vegetation composition of the other validation points in the same class (for grass: GH1, compared to GH4 or GH5; for forest: FR17, 18, 19 compared to FR20; appendix VII). So you would expect a similar value in measured LAI. One outlier, visible in all 3 observation angles, has a very high modelled value. This concerns validation point SH8 in the shrub class. Another validation point in the shrub class, SH11 only has a high value in the nadir direction. These high modelled values for SH8 and SH11 are probably due to modelling uncertainties. The validation points GH1, FR17, FR18, FR19, SH8, and SH11 were considered as outliers and therefore excluded from further analysis.
Best validation results are obtained in the nadir direction, with an R^2 of 0.2297. The ranges of values lie close to each other, but there does not seem to be a very strong correlation between measured and modelled LAI values. Validation results for the forward and backward scattering direction are very poor.

Appendix XIII contains scatter plots of the same validation results, but they show the results separately for the three modelled classes. The correlations are not very strong. The forest class shows an R^2 of 1, but this is not representative for the forest class, because the linear regression line was drawn based on only 2 points. In the nadir direction the shrub class gives the best validation results and in the forward and backward scattering direction best validation results were obtained from the herbaceous class.

Cross validation

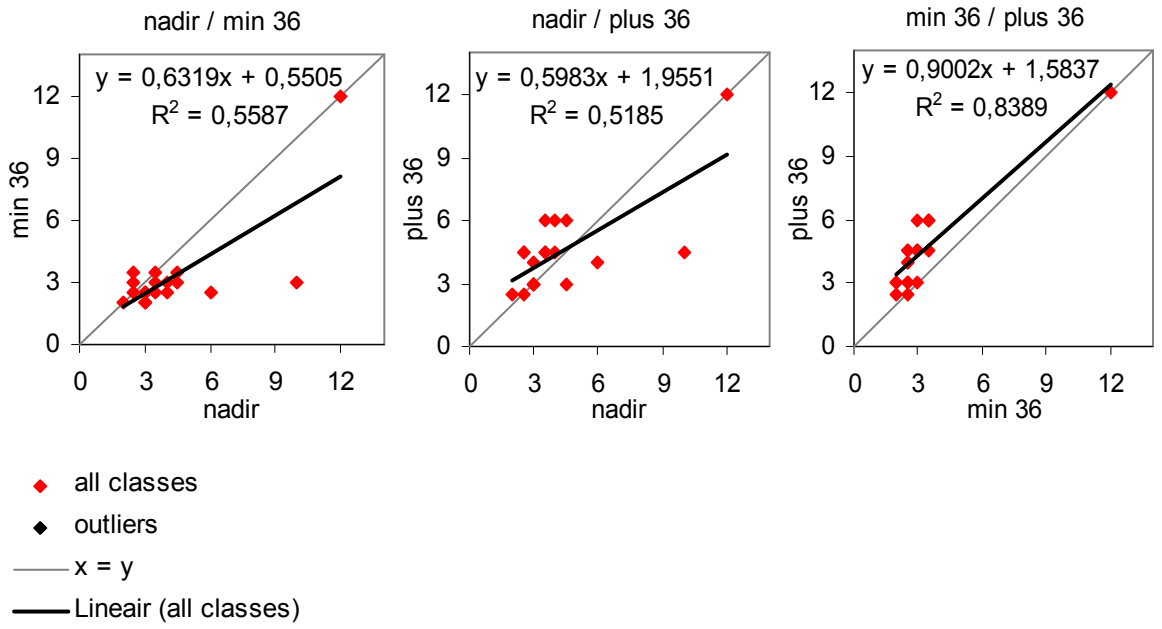

Figure 39: Scatter plots showing the cross validation results of the modelled LAI outcomes for the 3 different viewing angles for the 19 validation point locations of 2005.

The scatter plots from the cross validation in figure 39 show a relatively high correlation of LAI values between all CHRIS observation angles. The best results were obtained from cross validation of the backscattering (VZA -36) and the forward (VZA +36) scattering direction.

4.2.5 Validation of fCover with field data from 2004

The validation results of the modelled fCover with measured fCover from 2004 are not so good. There hardly seems to be any correlation between the modelled and measured fCover values. Validation points are scattered all over the plot, especially in the nadir and backward scattering direction. It is hard to find an explanation for this. It could be again due to the fact that the forest is heterogeneous and that therefore the modelled values for a CHRIS pixel differ too much from the measured values at one exact location. The nadir and backward scattering direction have better validation results than the forward scattering direction. The R^2s are 0.34 and 0.24 respectively. For this analysis the validation points with a large difference in modelled and measured values were excluded, so taking these points into account would make the results even worse. Appendix XIV contains the scatter plots that show the correlation between the modelled and measured fCover values and also the scatter plots with the cross validations. The results from cross validation are even weaker than the validation results themselves. There seems to be no correlation between the different observation angles.

4.2.6 Critical assessment of outliers

In figure 40 the HDRF values from the CHRIS nadir data are plotted against the measured LAI values from 2004 and 2005. Reflectance in the green, red and NIR band are plotted separately. The scales of the x and y axes are set equal so the results from 2004 and 2005 can be compared.
A positive linear relationship is expected between the NIR/Red VI and LAI, and between the NIR/Green VI and LAI (Kimura et al. 2004). Based on this finding, you would expect certain linear relationships between reflectance in NIR, red and green with LAI: A positive linear relation between NIR reflectance and LAI, and a negative linear relation between red reflectance and LAI, and green reflectance and LAI. The same kind of relationships was found in the study of Rautiainen et al. (2009).

Measurements of 2004

Linear regression lines are drawn through all the measured points, excluding the points that were labelled as outliers. In this way it becomes clear if the points that were labelled as outliers (black dots), also show a different relation than expected between reflectance values and LAI. The black dots with a red circle (figure 40, on the left side) are in such a position that they would change the direction of the linear regression line in a wrong way if they were included for linear regression. This justifies the decision that those points are considered as outliers based on LAI measurements. This concerns the measurement points 3 and 10 (appendix VI). The other ‘outlier’; point 9 is the black dot in the middle of the graphs. There is no obvious reason why this point should be considered as outlier, because this point falls in the right range of linear regression. So probably point 9 is an outlier because of modelling accuracies: the modelled LAI value of this point is too high. Looking at the same 3 points (point 3, 9 and 10) in the fCover validation table and graphs (appendix XIV), points 3 and 9 can also be seen as outliers. Point 10 is positioned relatively close to the ‘x=y’-line and is not an outlier in the fCover graphs.

Measurements of 2005

The measured points in the graphs (figure 40, on the right side) are split up in 3 classes. The linear line is drawn through all points from all classes, excluding the outliers. Only for the herbaceous class the negative trend in linear regression for the green and red band, and the positive trend for the NIR band can be seen. However, the points are not positioned very close together. The herbaceous outlier with the red circle is GH1. This point is located in natural grassland (appendix VII). There is no reason why this point should have a higher measured LAI value than the rest of the GH points, so it concerns an outlier. For the shrub class the linear relation between reflectance values and LAI is not obvious. It seems that the decision of the choice of outliers was right, but in fact the expected linear relationships can not be drawn between the remaining shrubs points. For the forest class a negative linear trend can be seen in the green and red band. In the NIR band, there is no positive linear trend. The group of three forest outliers (red circle) should have higher reflectance values in the NIR band. The decision seems right to consider them as outliers.

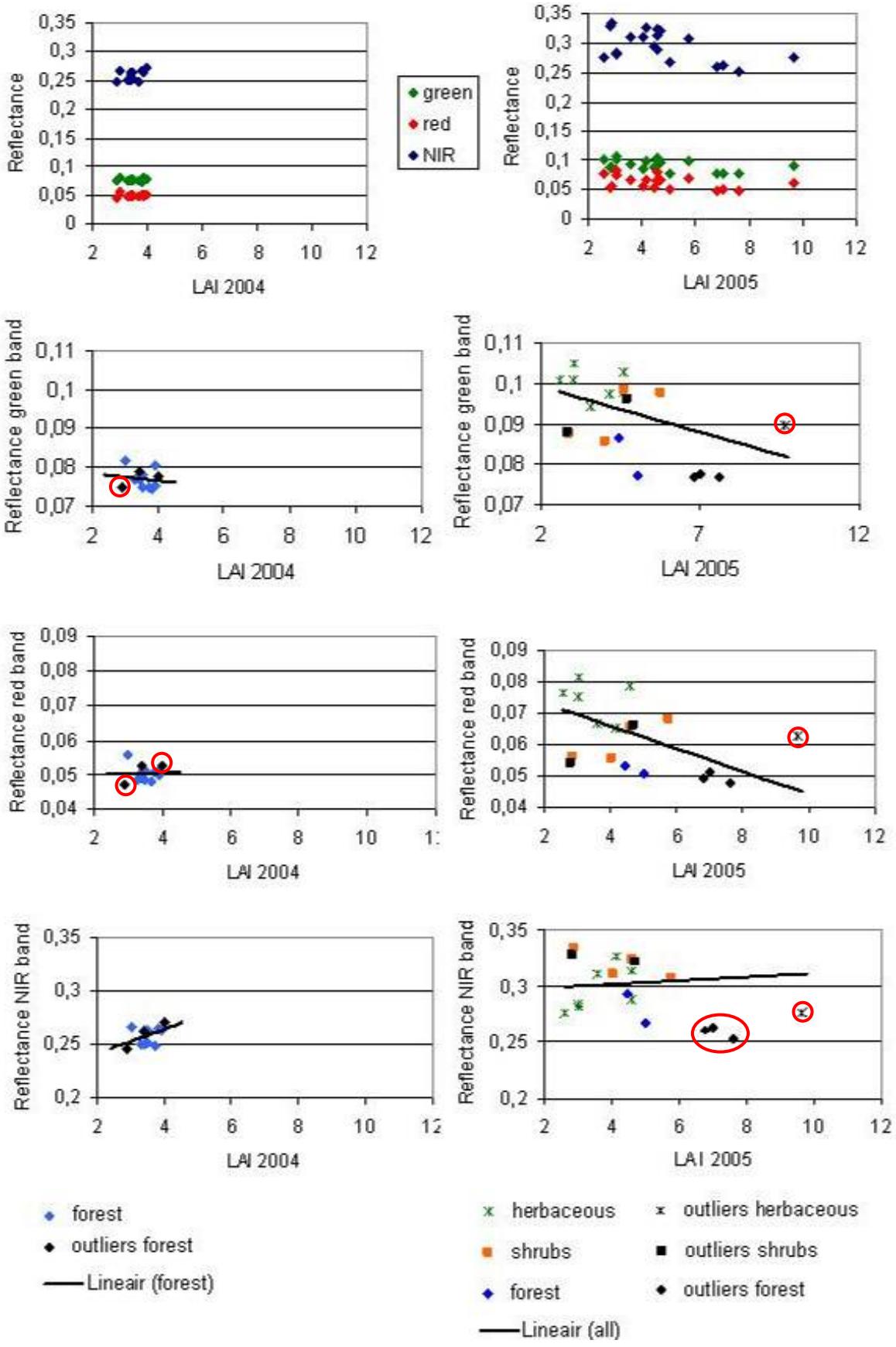

Figure 40: Spectral reflectance in green, red and NIR bands (bands 4, 8 and 14) of the CHRIS nadir data in comparison to the LAI measured in 2004 and 2005.

5. Discussion

5.1 Classification of vegetation structure types

5.1.1 Separability of classes

In the feature space plot of figure 14 and from the separability values in appendix VIII it becomes apparent that the ROIs are well separated. The classes lie close to each other in the feature space plot, but do not really overlap. Except for the pair of "grasses and low herbaceous" and "higher herbaceous", all separability values are higher than 1.9. Therefore the decision was made to combine those two herbaceous classes in one class "herbaceous" for the modelling part of the research.
The classes with different vegetation structure types lie closest to each other in the feature space plot. They all show a high reflectance in the NIR band and a low reflectance in the Red band. This is characteristic for vegetation and it indicates the red edge inflection point. The arable land class is well separated from all the other classes. It was useful to create this extra class, because it does not show many similarities to the other classes. Arable land consists of mainly maize; this has different spectral characteristics than other vegetation types in the image.

Field validation
Field validation was preformed in early Spring 2009. The field observations were only done to get a general idea of the vegetation composition in the floodplain area, because the classification was based on CHRIS images from 2005. It was clearly visible that the vegetation had developed since this date. For example, what belonged to the higher herbaceous class on the CHRIS classification image had become part of the shrubs area. Also, there were more bare soil parts in the field: the soil has been excavated as part of the nature rehabilitation and floodplain restoration projects. During field validation, all grasses and herbaceous vegetation were low, because it was the month of March, while the CHRIS acquisition was done in September. Therefore, there were no differences detectable between the classes of "grasses and low herbaceous" and "higher herbaceous" vegetation in the field.

5.1.2 Misclassifications

Table 9 and 10 show the accuracy and misclassifications of the CHRIS nadir ML classification. Misclassifications can be due to the large pixel size of the CHRIS data. If some of the classes are mixed within a pixel, the spectral signature is a mixture of these classes too. The pixel is classified to the class for which the pixel reflectance values have the highest probability. So, for part of the pixel this can be right. However, the whole pixel is generalized and the parts that actually belong to another class are misclassified.
Furthermore, due to the large pixel size, some class boundaries have shifted from the actual position which is illustrated in figure 41. The random sample point 134 is positioned in a forested area, but in the CHRIS image, this point still belongs to the water class. The largest part of this pixel consists of water; therefore the whole pixel was classified as water. Around 9 random sample points were positioned near a class boundary and were misclassified because of this.

Figure 41: Misclassification due to pixel size of CHRIS image and shifting of boundaries.

Another reason for misclassification can be that sometimes the spectral signatures in the CHRIS image, especially for the vegetation classes, are very similar, that they can easily be misclassified. It could for example happen that higher herbaceous vegetation is classified as shrubs.

On the classified CHRIS nadir ML image there are small lines on the river that were classified as sand. These lines are probably ships with a load of sand.
The spectral signature for the built-up class (figure 15) has some characteristics of a vegetation signature. It has a small peak in the green band (band 4) and makes a jump from the Red band to the NIR bands, although a smaller jump than for the vegetation signatures. The reason for this can be that within built-up areas there are vegetated areas as well, such as gardens, parks and trees. The pixel size of CHRIS is about 17m*17m, so within a pixel small vegetated areas are mixed with the buildings and streets. This causes a mixed signal.
In Millingerwaard (and elsewhere in the image) there are small spots of "built-up" area. These are probably scattered houses, farms or piles of bricks. Of course not the whole pixel consists of built-up area, but the mixture of signals of houses and their surroundings probably comes closest to the "built-up" signature.

5.1.3 Difference in classification accuracy when using different methods and input maps

The used classification methods resulted in differences of overall classification accuracy (tables 10 and 11). Best results were obtained with the ML classification that was performed on the CHRIS nadir image. The overall accuracy was 68%. The SVM classification of the CHRIS nadir image had less good results with an overall accuracy of 56%. SVM works well on complex and noisy data. ENVI uses a reduced resolution classification process for SVM classification. This works best with large homogeneous areas. The river floodplains however, are quite heterogeneous because shrubs, forests, grasses and herbaceous vegetation interchange with each other. The SVM classification worked well for the large homogeneous water and arable land areas. Misclassifications occurred mostly within the heterogeneous herbaceous classes. When the penalty parameter was set to 100, the "ships with loads of sand" were erased from the image, because the small spots of sand had been seen as unrealistic pixels in the river and thus were erased from the image.

Huber (2008) used the SVM methodology for making a land cover classification with multi-angular CHRIS data. The main findings of Huber were that SVM methods achieved higher classification accuracies than standard methods such as the ML classifier. However, Hubers study also showed that ML results differed considerably with different strategies of collecting training samples. It is important to choose the training samples (ROIs) well. For SVM classification, especially mixed pixels at the border of class boundaries should be included, because they are useful to determine the support vectors and the hyperplane (borders) between two classes. For ML classification however, rather pure pixels are required for the ROIs to explicitly separate land cover classes. For this thesis research, mostly pure pixels were chosen for the ROIs. As an addition, some pixels near class boundaries were chosen. Probably SVM classification would have performed better, when a different set of ROIs was chosen, mainly located next to class boundaries.

The stacked layers ML classification has the lowest accuracy of all: only 44%. The spectral signature of the pixels consists of a combination of signatures from the three viewing directions. The nadir signature of one pixel can for example be the reflectance of bare soil. But the forward scattering and backward scattering signatures of the same pixel can contain the reflectance of something else; for example a tree, standing just next to the bare soil part. The CHRIS sensor first received the reflectance of this tree. The bare soil part is behind the tree and thus could only be detected from the nadir viewing direction. Many pixels that are lying close to class boundaries were assigned to the wrong class, probably because they have a spectral signature that is a mixture of different classes.
Another striking thing is that water bodies were enlarged in the image. This could be explained by the following: the forward scattering and backward scattering direction "detect" water; while in the

nadir viewing direction something different is detected. The water signal is very low and distinctive (see figure 15) so it has a large influence on the mixed signature of the pixel. Therefore, the pixel has the highest probability to fall into the water class.

The stacked layers ML classification with PCA performed better than without PCA. The PCA classification is based on the variability of information in a pixel. Because of this, the regions of interest contain more characteristic information. They are not a mixture of 3 angular layers, but they consist of separate PCA bands with a high variability. The more PCA bands are used, the better the results get. The accuracy for the first 3 PCA bands is 55%, for the first 4 PCA bands 56% and for the first 5 PCA bands 58%. This is reasonable because more PCA bands contain more variability of data. Although, the more bands, the smaller the *extra* amount of variability gets. What is remarkable is that in all these classifications some parts are classified as built-up, while they actually belong to another class. This can be especially seen along river borders. A mixed signature of water and bare soil resembles most to the built-up signature and is therefore classified as built-up area. This can be seen in figure 15 where the built-up spectral signature lies in-between the water and bare soil signature.

Simic and Chen (2008) found that hyperspectral measurements in multiple CHRIS VZAs have much redundancy in data. They tried to refine the measurement concept and concluded that next to hyperspectral measurements in the nadir direction, only measurements in the red and NIR band in two other directions would suffice. The two other directions would be the hotspot, the angle where the sun and view directions coincide and the darkspot, the angle where the sensor sees the maximum amount of vegetation structural shadows. Further research could be done to see if this method would improve the classification results.

5.1.4 Difference in classification accuracy of RWS and CHRIS ecotope maps

The RWS classification has a higher overall accuracy (81%) than the CHRIS classification (68%). This is probably due to the pixel size from the images that were used for classification. A dedicated method using aerial photographs with a high spatial resolution was used for the RWS classification. Small lines of forest and shrubs can be discerned in the RWS ecotope classification map, which are not visible in the CHRIS classification map. The CHRIS images have a pixel size of around 17*17m². Taken into account the difference in pixel size and the amount of time needed to create a classification, the methodology used in this research shows good results.
In the classified RWS ecotope map, the classes look quite homogeneous. The classification of the CHRIS image looks more heterogeneous. This is more realistic, because natural areas in a river floodplain ecosystem are a mixture of grasses, herbs, shrubs and trees.

5.1.5 Added value of multi-angular data

Best classification results were obtained with ML classification performed on the CHRIS nadir image. Classification with multiple (stacked) layers as input did not give better results. This means that with the current research methodology, the use of multiple angular images as classification input do not improve the classification results.
Different angular images, however, do have an added value in making the ML classification on the nadir image. This accounts for the process of choosing the ROIs on which the ML classification is based. When the 3 layers of VZA -36, nadir and VZA +36 were stacked, certain band combinations showed more distinctive colours for the different classes. This was especially the case after performing PCA on the stacked layers image. With certain PCA band combinations, classes stood out compared to the other classes and ROIs could be chosen with great precision. With RBG band composition, water for example can be easily mistaken for dark coloured vegetation. But with PCA bands 1,3 and 4 (figure 10), water becomes easily detectable. So, with respect to the first research question, the added value of using multi-angular data lies in the decision making process of choosing ROIs for ML classification.

No added value could be seen when using the ML classification on the stacked layers image, neither when using PCA as additional method. As written in 5.1.3 this could be due to the fact that a 'stacked layers'-pixel contains a mixed signature.

Not much literature could be found on making classifications of multi-angular remote sensing images. Most articles have the focus on assessing vegetation structure and deriving canopy biophysical and vegetation biochemical variables from multi-angular data.
In one of the few articles about multi-angular classification techniques, Duco and Del Frate (2008) investigated the use of hyperspectral, multi-angular and multi-temporal measurements from CHRIS imagery to generate thematic maps. They also found that different multi-angular compositions allow a clearer perception of differences in land cover types and vegetation density, because differences are more evident in multi-angular band compositions than in RGB true colour compositions (for differences in angular signatures, see appendix II). This is why the ROIs were easier to choose on an image with a multi-angular band composition. PCA made the differences in land cover type even clearer because it presents the greatest variety in the multi-angular image.

Duca and Del Frate (2008) used an neural network methodology, making use of ROIs, to make a land cover classification based on CHRIS imagery. First they classified the nadir image with a precision of 85.7%. After stacking the images of VZA -36, nadir and VZA 36, the classification accuracy improved with 7%. Especially the classification of bare soil, asphalt and industrial buildings improved considerably. Probably, the neural network methodology, that uses multiple input values with associated weight factors and a function that sums the weights and maps the results to an output, performs better on multi-angular data than the ML classification that was used in this research. ML classification only uses statistical probabilities of pixels belonging to a land cover class, which is maybe not appropriate for multi-angular data. Huber (2008) found that the use of multi-angular data only slightly improved SVM and ML classification accuracies in general, when all bands from the stacked image were included. So, to improve classification results with the use of multi-angular data, probably the neural network methodology should be used.

5.2 Vegetation structure properties

5.2.1 Modelling results for LAI

The colour gradient in the LAI maps of figures 18, 20 and 22 shows the variability in LAI values within the vegetation structure types. Especially in the natural grasslands and heterogeneous forest parts this variability is very obvious. The parts in the forest, shrub and herbaceous areas that show the darkest colours, have the highest LAI values. This means that they have the largest leaf surface per unit ground area, contain a high amount of chlorophyll and thus have a high photosynthetic rate. As a consequence, in these parts there is most accumulation of biomass. So these parts have a high relevance with respect to water resistance in river floodplain ecosystems and river managers should pay special attention to these areas.

The range of modelled LAI values is the same as the range of measured LAI values from 2004. The ranges of modelled and measured LAI values from 2005 are more diverged. In general, the modelled LAI is slightly lower than the measured LAI (figures 36 and 38). There could be several reasons for this. First, it is not sure if the measured LAI values are reliable, because the two validation datasets from 2004 and 2005 differ much from each other. From figure 40 it became apparent that the validation dataset from 2005 is less reliable. Also, LAI measurements within one validation dataset show varying results for the same type of vegetation. You would expect a quite similar LAI value for these parts. Second, it can be due to the parameterization of the model. Certain spectral signatures for leaves, woody parts and background were used as model input. Those spectral signatures were obtained at a different location and under other circumstances than when the CHRIS images were acquired for Millingerwaard. When input spectral signatures would be used from the same location, the modelled LAI results would maybe resemble more the LAI ground measurements.

There are some parts with extremely high LAI values of 10 and 12 in the nadir and backward scattering direction, and high values of 6, 6.5 and 12 in the forward scattering direction. This mainly concerns arable land, with maize crops, that had been (mis)classified as "herbaceous class" or "shrub class". As a consequence it was also modelled as "herbaceous class" or "shrub class" and this gives some erroneous results in the maps. The high values can be explained as follows: The leaf size of maize is much bigger than the leaf size of *Calamagrostis epigejos* or *Salix alba*, that were used as model input. A leaf of *Calamagrostis epigejos* would fit several times in a leaf of maize. To compensate for the leaf size, the model creates a very high LAI value. So, when using the *Calamagrostis epigejos* leaves as model input in stead of maize leaves, the total surface of the leaves will be the same as for the maize leaves.
Other parts with high LAI values are lines along the winter dikes next to the road, especially visible in the nadir and forward scattering direction. The vegetation on these dikes consists of grass. Grass has the characteristic to grow very fast. It could be that when the CHRIS images were obtained in September, the grass on these dikes was dense and high, resulting in a high LAI.

The modelling results for the forest class, using the 1D (turbid medium) modelling approach, were better than the 3D modelling results. They showed more variation in LAI values. This could be because the 3D modelling approach has a more extensive parameterization process, which could not be properly done in this study. Widlowski et al. (2005) studied if 1D models could describe forest reflectance as good as 3D models can. They concluded that results from 1D models match well the results from 3D models, both in magnitude and in directionality. So, it is maybe not necessary to use the 3D modelling approach and the 1D modelling approach is sufficient for modelling the forest canopy.

5.2.2 Modelling results for fCover

High fCover values occur at the same places as high LAI values (figures 18, 20, 22 and 27, 29, 31). This is what you would expect, because LAI and fCover are closely related. The large arable field in the north east of Millingerwaard received the highest fCover values. This is reasonable because it is a homogeneous maize field. The natural grasslands and some parts of the forest also received high values. The fCover maps however, do not look as smooth as the LAI maps, but are much more granulated. Probably the modelling outcome for fCover is not as good as for LAI and fCover maps should have had a smoother colour gradient. The validation results for fCover also showed that the modelled fCover results are quite poor. LAI maps look more realistic and the validation results were better. Jimenez et al. (2009) obtained good fCover validation results with approaches based on VI-modelling and spectral mixture analysis. fCover was calculated for homogeneous agricultural fields. Probably the fCover validation results for Millingerwaard are quite poor, because it is a heterogeneous area. Unfortunately, not much literature could be found on physical based fCover modelling results and multi-angular (CHRIS) data, so it is hard to explain the results and compare them with other findings.

5.2.3 Modelling results for PV

The focus of this study was not on the variable PV. The modelling results for PV were not realistic yet, because PV always received the lowest possible LUT value. There can be several reasons for this. Possibly, the model is not fit yet for this variable and further research is needed to improve the model for use of this variable. Also, more attention should be paid to the parameterization of this variable. There were no ground reference data available, so the parameterization process could not be properly done. The fact that PV always received the lowest possible LUT value would imply that the fraction of photosynthetic vegetation in the area is low, and that there is a lot of non-photosynthetic material (bark) present. This is not a realistic model outcome, because Willow trees consist of more photosynthetic vegetation than only 50% or 70% which were the modelled PV results.

5.2.4 Validation results

Validation points from 2004 (figures 36 and 37)
The ranges of measured and modelled LAI values are very similar. There is a quite high correlation between the measured and modelled LAI values in the nadir direction. The correlation in the forward and backward scattering direction is lower. However, with cross validation, the modelled LAI values from the forward and backward scattering direction together show a high correlation. This is what you would expect, because the satellite observes the same kind of tree structure in an angle of 36 degrees, either in the forward or in the backward scattering direction.

The validation points of fCover are spread all over the scatter plots, there seems to be hardly any correlation between measured and modelled fCover values. Leaving out all the outliers, the nadir and backscattering direction give the best validation results. When doing cross validation, there seems to be no correlation between the different observation angles. There is no obvious reason for this. Maybe better parameterization of the model is needed.

Validation points from 2005 (figures 38 and 39)
There is not a high correlation between measured and modelled LAI values. When leaving out the outliers, best validation results were obtained in the nadir direction. Cross validation, however, shows better validation results. This means that the LAI model outcomes in different observation angles are highly correlated. Best cross validation results were again obtained from the backscattering together with the forward scattering direction. This is the same kind of result as could be seen with the validation points used in 2004.

Reliability of field measurements
From the graphs in figure 40 the reliability of the field measurements becomes clear. There should be a negative linear relationship between the CHRIS HDRF in the green band and the measured LAI, and the red band and the measured LAI. There should be a positive linear relationship between the CHRIS HDRF in the NIR band and the measured LAI.
This trend can be partly seen in the data from 2004. The green band shows the negative linear relation and the NIR band show the positive linear relation. The red band does not show a very clear negative linear relation. Also, the points are located very close to the linear line.
The relations are not so well expressed in the data from 2005. There is a negative linear relation in all the graphs, and the validation points are not closely located to the linear line. For the individual classes, only the herbaceous class seems to have the right relationships.
Therefore, it can be concluded that the validation results with data from 2005 are less reliable than those with data from 2004.

5.2.5 Added value of multi-angular data

A good result is that the LAI values in the backscattering and forward scattering direction are highly correlated. This implies that the model gives good results, because the same kind of vegetation structure in observed under an angle of 36 degrees, either in the forward or in the backward direction.
Most variability in results can be seen in the backscattering direction (-36 VZA). The highest peaks in LAI, and thus the places where vegetation is developing fast, are most obvious in this VZA. The polar plot (appendix I) indicates that the sun is shining from the same direction as the image backscattering direction. This explains the good modelling results of the -36 VZA. Huber (2008) found similar results and concluded that there is an increase in reflectance in the backward scattering direction. The -36 VZA is located closest to the images hotspot, where solar reflection is highest and there are almost no shadowing effects. It is shown that the canopy hotspot effect contains most information for vegetation characterization, especially for canopy structure. Less variability can be observed in the nadir angle. Like in the study of Huber (2008) the minimum reflectance values occurred in the forward scattering directions, because shaded leaf surfaces are present in this direction. The forward scattering angle does not show a lot of variability. Similar

results were found in the study of Liesenberg et al. (2007). They showed that the surface anisotropy signatures were not unique and varied with sun-view geometry and seasonality. Strongest anisotropy was observed in the backward scattering direction and in the red band. The best view angles for their classification purposes were from nadir to -45˚. In this research the reverse FLIGHT modelling option was used, where only one angular image is used at a time. In forward modelling there is an option to combine different angular images. This could give interesting results. Maybe a combination of the nadir and backward scattering angle would give the best results for indicating the places with highest LAI values.

5.2.6 Added value of RT models compared to VI based models

In this research the RT modelling approach was followed to estimate vegetation structure properties. This physical based modelling approach is rather new compared to the "traditional" VI (vegetation-index)-based modelling approach, which is an empirical approach. A comparative analysis performed by Richter et al. (2008), showed that improvements on the empirical approaches have been achieved lately with physical model techniques. LAI estimation results from empirical approaches were obtained through the semi-empirical relationship between LAI and a vegetation index like NDVI or WDVI. They used the RT model PROSAILH for the physical based method. It was shown that the empirical methods have limitations, because they are site and sensor dependent. So they require reliable ground measurements for calibration. Accuracy of LAI results from the physical based modelling approach was higher than from the VI-based modelling approach. They concluded that the physical model inversion approach is more promising for LAI estimation. As RT models take the physical features of a plant into account and VI-based models are based on semi-empirical relationships, the physical based modelling approach seems more realistic in describing the interaction of solar radiance with vegetation components. This means that the results from this thesis research are very promising, because the physical based model FLIGHT was used. It would be interesting to derive LAI maps based on a VI-modelling approach and validate them with the same ground measurements as the current results. Then a conclusion can be made if the RT modelling approach is better than the VI based modelling approach.

5.2.7 Coupling of model outcomes with hydraulic roughness values

At this moment RWS calculates the hydraulic roughness values in river floodplain ecosystems per ecotope. The ecotope classification (Van Velzen et al., 2003) is comparable to the ecotope classification used in this research. The only difference is that RWS has more detailed classes in the classification. The main driving factors that determine the hydraulic roughness values are vegetation height and density for grasslands, and vegetation height and soil conditions (e.g. undergrowth or dead wood) for shrubs and forests.

Table 12: Average modelled LAI values for the forest class in each viewing direction.

Forest			
VZA nadir	VZA -36	VZA +36	Average all VZA's
2,98	3,16	3,63	3,26

Table 13: Average modelled LAI values for the shrub class in each viewing direction.

Shrubs			
VZA nadir	VZA -36	VZA +36	Average all VZA's
7,31	5,92	6,78	6,67

Table 14: Average modelled LAI values for the herbaceous class in each viewing direction.

Herbaceous			
VZA nadir	VZA -36	VZA +36	Average all VZA's
5,71	4,48	4,68	4,96

At this moment it is difficult to couple the modelled LAI values from this study to the hydraulic roughness values of RWS. Hydraulic roughness indications for herbaceous vegetation were 0.25-1.45 (table 2), for shrubs 24.41 and for forest 12.84. It is only possible to say something about the shrubs and forest class because they were modelled with the same species *Salix alba*. The average modelled LAI values for all VZAs (tables 12, 13 and 14) for shrubs (6.67) were twice as high as for forest (3.26). This is the same kind of difference in magnitude as for the hydraulic roughness values: 24.41 and 12.84. Both outcomes for the shrub and forest class differ from each other with a factor 2. Based on this finding, a linear relation could maybe be expected between the modelled LAI per vegetation structure type and the hydraulic roughness indication. Further research on this aspect is necessary to be able to conclude something about this.

5.3 Extrapolation of the methodology

An extrapolation to the Gelderse Poort area has been made. There was no validation set available, but a similar trend in magnitude and distribution of LAI and fCover values can be seen in the maps. The only difference is that there are more arable fields present in the Gelderse Poort, which were incorrectly modelled as herbaceous or shrub class. This resulted in more high LAI values of 10 or 12. But overall, it seems possible to extrapolate the method to the Gelderse Poort area. This means that the method could also be extrapolated to other river floodplain ecosystems, when using CHRIS images as input for classification and modelling.

6. Conclusions and recommendations

The first research question was: *"How can different vegetation structure types in a river floodplain ecosystem be classified using multi-angular CHRIS-PROBA imagery?"*.

The best classification results, with an overall classification accuracy of 68% were obtained with the ML classification based on ROIs, performed on the CHRIS nadir image with spectral bands 2-18. With the current classification methodology, the use of multiple angular images did not improve the classification accuracies. The added value of multi-angular data was only in the choice of ROIs: pixels from different classes were easier to detect on an image that was composed of PCA bands from the stacked layers of VZA -36, nadir and VZA +36.

All spectral bands, except for band 1, were used for classification. It is possible that there was redundancy in spectral bands. Classification results could be improved with a better band selection. Also, a better choice of pixels for ROIs could improve the results. For ML classification, pure pixels should be chosen and for SVM classification pixels on the borders between classes should be chosen. As was described in literature, probably the SVM or NN (neural network) approaches could give better results than the ML classification method.

The second research question was: *"How can the canopy structure properties LAI, fCover and PV be derived from multi-angular CHRIS-PROBA data using the radiative transfer, monte carlo ray tracing model FLIGHT (North, 1996)?"*.

The canopy structure properties LAI, fCover and PV were derived with the model FLIGHT in reverse mode. A LUT approach, with the LUT containing varying values of the three variables, was used to run the model. The reflectance outcome (BRF) was compared with the reflectance (HDRF) of each CHRIS pixel and best fits were made based on the RMSE method. Using an inversion script, LAI, fCover and PV maps were derived. Although physically simplified, the 1D modelling approach provided superior results compared to the 3D modelling approach, probably due to the less extensive parameterization process. LAI maps looked smooth and showed a gradient in LAI values. fCover maps were more granulated but also showed variation in values. PV maps did not show any variation. This implies that the model FLIGHT is appropriate for modelling LAI values. The method needs to be improved to derive realistic fCover values, maybe with better parameterization of the model. Possibly the model is not fit yet for the variable PV. Further research is needed to improve the model performance for this variable.

Best LAI modelling results were obtained in the backscattering (VZA -36) direction. This angle shows most variations in LAI values. The differences in LAI values are more pronounced than in the nadir direction, because the backscattering angle coincides more with the solar viewing angle.

Further improvement of the model is possible by choosing better input spectral signatures. The model generalizes the canopy, because only one leaf spectrum and one background spectrum is used. For this research, some input signatures were averaged to get a more realistic canopy representation. In a heterogeneous canopy, however, the average spectral signature differs from location to location. More research in the test site could be done, to obtain more realistic (combinations of) input spectral signatures.

The third research question was: *"Are results still accurate when the methods from the first 2 questions are extrapolated to a larger floodplain area, namely from Millingerwaard (figure 42) to the complete area of the Gelderse Poort?"*.

Extrapolation of the method is possible, because an RT modelling approach was used and those methods are not site specific. The method has been successfully extrapolated to the Gelderse Poort resulting in LAI and fCover maps that show a similar distribution of values as for Millingerwaard. These results, however, could not be validated because of lack of ground reference data. It would be useful to try the currently used method with multi-angular CHRIS data for another river floodplain ecosystem, using a detailed ground data set for model parameterization and validation.

And finally, more research is needed to find out if it is possible to link the LAI findings to hydraulic roughness values. In this way the LAI maps (or hydraulic roughness maps derived from LAI maps) could give an indication to river managers were management measures are most needed. LAI maps could improve the hydraulic roughness indication, because the hydraulic roughness values are computed per ecotope and the LAI values are derived per pixel. So within ecotope variation becomes clear when using LAI values from this thesis methodology.

Figure 42: The river Waal and softwood forest development on the shores of Millingerwaard (photography: Erika Romijn).

References

ALLEN, W.A., GAUSMAN, H.W., RICHARDSON, A.J. & THOMAS, J.R. (1969) “Interaction of isotropic light with a compact plant leaf”, *Journal of the Optical Society of America,* 59 (10), pp. 1376-1379.

BARNSLEY, M. J., SETTLE, J.J., CUTTER, M.A., LOBB, D.R. & TESTON, F. (2004) "The PROBA/CHRIS mission: A low-cost smallsat for hyperspectral multiangle observations of the earth surface and atmosphere", *IEEE Transactions on Geoscience and Remote Sensing*, 42(7), pp. 1512-1520.

BROADBENT, E.N., ZARIN, D.J., ASNER, G. P., PEÑA-CLAROS, M., COOPER, A. & LITTELL, R. (2006) “Recovery Of Forest Structure And Spectral Properties After Selective Logging In Lowland Bolivia”, *Ecological Applications,* 16 (3), pp. 1148-1163.

CARLETTA, J. (1996) “Squibs and discussions: Assessing agreement on classification tasks: The kappa statistic”, *Computational linguistics,* 22 (2), pp. 248-254.

CHEN, J. M., LIU, J., LEBLANC, S.G., LACAZE, R. & ROUJEAN, J-L. (2003) "Multi-angular optical remote sensing for assessing vegetation structure and carbon absorption", *Remote Sensing of Environment,* 84(4), pp. 516-525.

CHOPPING, M., SU, L., LALIBERTE, A., RANGO, A., PETERS, D.P.C. & KOLLIKKATHARA, N. (2006) "Mapping shrub abundance in desert grasslands using geometric-optical modeling and multi-angle remote sensing with CHRIS/Proba", *Remote Sensing of Environment,* 104(1), pp. 62-73.

CHUMA, B.J., (2008) *Opportunities for mapping heathland habitat types using multi-angular CHRIS PROBA data.* [student report] Wageningen University.

CHUVIECO, E. (2008) *Earth Observation of Global Change: The Role of Satellite Remote Sensing in Monitoring the Global Environment.* Dordrecht: Springer.

D'URSO, G., DINI, L., VUOLO, F., ALONSO, L & GUANTER, L. (2004) “Retrieval of leaf area index by inverting hyper-spectral, multi-angular CHRIS/Proba data from sparc 2003”. In: European Space Agency. *Proc. of the 2nd CHRIS/Proba Workshop.* Frascati, Italy, 28-30 April (ESA SP-578, July 2004), ESA/ESRIN.

DE BRUIN, D., HAMHUIS, D., VAN NIEUWENHUIJZE, L., OVERMARS, W., SIJMONS, D. & VERA, F. (1987) *OOIEVAAR: De toekomst van het rivierengebied.*Arnhem: Sticgting Gelderse Milieufederatie.

DINER, D. J., ASNER, G.P., DAVIES, R., KNYAZIKHIN, Y., MULLER, J-P., NOLIN, A.W., PINTY, B., SCHAAF, C.B. & STROEVE, J. (1999) "New Directions in Earth Observing: Scientific Applications of Multiangle Remote Sensing", *Bulletin of the American Meteorological Society,* 80(11), pp. 2209-2228.

DINER, D. J., BRASWELL, B.H., DAVIES, R., GOBRON, N., HU, J., JIN, Y., KAHN, R.A., KNYAZIKHIN, Y., LOEB, N., MULLER, J-P., NOLIN, A.W., PINTY, B., SCHAAF, C.B., SEIZ, G. & STROVE, J. (2005) "The value of multiangle measurements for retrieving structurally and radiatively consistent properties of clouds, aerosols, and surfaces", *Remote Sensing of Environment,* 97(4), pp. 495-518.

DUCA, R. & DEL FRATE, F. (2008) "Hyperspectral and multiangle CHRIS-PROBA images for the generation of land cover maps", *IEEE Transactions on Geoscience and Remote Sensing*, 46(10), pp. 2857-2866.

GEERLING, G. (2008) *Changing rivers: analysis fluvial landscape dynamics using remote sensing.* Ph.D. Radboud University Nijmegen.

GENSUO, J.J., BURKE, I.C., GOETZ, A.F.H., KAUFMANN, M.R., & KINDEL, B.C. (2006) "Assessing spatial patterns of forest fuel using AVIRIS data", *Remote Sensing of Environment,* 102: 318-327.

GIDYELEW MENGESHA, T. (2005) *Validation of ground biophysical products using imaging spectroscopy in a softwood forest.*[student report] Wageningen University.

GOBRON, N., PINTY, B., VERSTRAETE, M.M. & GOVAERTS, Y. (1997) "A semidiscrete model for the scattering of light by vegetation", *Journal of geophysical research,* 102(D8), 9431-9446.

GONSAMO GOSA, A. (2006) *Estimation of leaf area index using optical field instruments and imaging spectroscopy.*[student report] Wageningen University.

GROEN, K. & SCHMEINK, T. (1981) *Waterschappen in Nederland.* Baarn: Keuning.

GUANTER, L., ALONSO, L. & MORENO, J. (2005) "A method for the surface reflectance retrieval from PROBA/CHRIS data over land: Application to ESA SPARC campaigns", *IEEE Transactions on Geoscience and Remote Sensing*, 43(12), pp. 2908-2917.

GUERSCHMAN, J.P., HILL, M.J., RENZULLO, L.J., BARRETT, D.J., MARKS, A.S. & BOTHA, E. J. (2009) "Estimating fractional cover of photosynthetic vegetation, non-photosynthetic vegetation and bare soil in the Australian tropical savanna region upscaling the EO-1 Hyperion and MODIS sensors", *Remote Sensing of Environment,* 113(5), pp.928-945.

HUBER, S. (2008) *Estimation of Ecologically Relevant Land Cover Variables from Imaging Spectroscopy.* Ph.D. Zürich University.

HUEMMRICH, K.F. (2001) "The GeoSail model: A simple addition to the SAIL model to describe discontinuous canopy reflectance", *Remote Sensing of Environment*, 75(3), pp. 423-431.

JACQUEMOUD, S. & BARET, F. (1990) "PROSPECT: A model of leaf optical properties spectra", *Remote Sensing of Environment*, 34(2), pp. 75-91.

JIA, G.J., BURKE, I.C., GOETZ, A.F.H., KAUFMANN, M.R. & KINDEL, B.C. (2006) "Assessing spatial patterns of forest fuel using AVIRIS data", *Remote Sensing of Environment,* 102(3-4), pp.318-327.

JIMENÉZ-MUNOZ, J.C., SOBRINO, J.A., PLAZA, A., GUANTER, L., MORENO, J. & MARTÍNEZ, P. (2009) "Comparison Between Fractional Vegetation Cover Retrievals from Vegetation Indices and Spectral Mixture Analysis: Case Study of PROBA/CHRIS Data Over an Agricultural Area", *Sensors,* 9, pp. 768-793.

JONCKHEERE, I., S. FLECK, K. NACKAERTS, B. MUYSA, P. COPPIN, M. WEISS & BARET, F. (2004) "Review of methods for in situ leaf area index determination Part I. Theories, sensors and hemispherical photography", *Agricultural and Forest Meteorology,* 121, pp. 19-35.

KIMURA, R., OKADA, S., MIURA, H. & KAMICHIKA, M. (2004) “Relationship among the leaf area index, moisture availability, and spectral reflectance in an upland rice field”, *Agricultural Water Management,* 69(2). Pp. 83-100.

KOETZ, B., SCHAEPMAN, M., MORSDORF, F., BOWYER, P., ITTEN, K., & Allgöwer, B. (2004) “Radiative transfer modeling within a heterogeneous canopy for estimation of forest fire fuel properties”, *Remote Sensing of Environment*, 92, 332−344.

KOETZ, B., KNEUBÜHLER, M., HUBER, S., SCHOPFER, J.T., & BARET, F. (2007) “LAI Estimation Based on Multi-temporal CHRIS/PROBA Data and Radiative Transfer Modelling”. In H. Lacoste & L. Ouwehand (Eds.). *Envisat Symposium*. Montreux, Switzerland, 23-27 April 2007, ESA Communication Production Office, ESTEC: Noordwijk, The Netherlands.

KOOISTRA, L., WAMELINK, W., SCHAEPMAN-STRUB, G., SCHAEPMAN, M., VAN DOBBEN, H., ADUAKA, U. & BATELAAN, O. (2008) "Assessing and predicting biodiversity in a floodplain ecosystem: Assimilation of net primary production derived from imaging spectrometer data into a dynamic vegetation model", *Remote Sensing of Environment,* 112(5), pp. 2118-2130.

LIESENBERG, V., GALVÃO, L.S. & PONZONI, F.J. (2007) "Variations in reflectance with seasonality and viewing geometry: Implications for classification of Brazilian savanna physiognomies with MISR/Terra data", *Remote Sensing of Environment,* 107(1-2), pp. 276-286.

LILLESAND, T.M., KIEFER, R.W. & CHIPMAN, J.W. (2004) *Remote sensing and image interpretation.* 5th edition. University of Wisconsin – Madison: Wiley.

LIRAS LAITA, E. (2005) *Imaging Spectroscopy for Ecological Monitoring at the Test Site the Millingerwaard: Species Mapping using Spectral Libraries and Soil-Vegetation-Atmosphere-Transfer Models.*[student report] Wageningen University.

LORENZ, C.M. (2001) *Rijkswateren ecotopen stelsel: oevers.* Deventer: Witteveen + Bos.

MA, J., CHAN, J.C.-W. & CANTERS, F. (2009) “Automatic image registration of multi-angle imagery for CHRIS/PROBA”. In E. Ben-Dor et al. (Eds.). *Proceedings 6th EARSeL SIG IS workshop "IMAGING SPECTROSCOPY: Innovative tool for scientific and commercial environmental applications".* Tel-Aviv, March 16-19, EARSeL.

NORTH, P.R.J., (1996) “Three-dimensional Forest Light Interaction Model using a Monte Carlo method”, *IEEE Transactions on Geoscience and Remote Sensing,* 34(4), pp. 946-956.

RICHARDS, J.A. & XIUPING, J. (1999) *Remote Sensing Digital Image Analysis: An Introduction*, 3rd revised and enlarged edition. Berlin, Heidelberg, New York, London, Paris, Tokyo, Hong Kong: Springer-Verlag

RICHTER, K., VUOLO, F. & D’URSO, G. (2008) Leaf area index and surface albedo estimation: Comparative analysis from vegetation indexes to radiative transfer models. In: IGARSS. *International Geoscience and Remote Sensing Symposium (IGARSS)* 3 (1), art. no. 4779453, pp. III736-III739, Boston.

ROUJEAN, J-L. & LACAZE, R. (2002) “Global mapping of vegetation parameters from POLDER multiangular measurements for studies of surface-atmosphere interactions: A pragmatic method and its validation”, *Journal of geophysical research,* 107 (12), pp. ACL 6-1 – ACL 6-14.

RAUTIAINEN, M., NILSON, T. & LÜKK, T. (2009) “Seasonal reflectance trends of hemiboreal birch forests”, *Remote Sensing of Environment*, 113, pp. 805-815.

RIJKSWATERSTAAT (2008-2) *Ecotopenkartering Rijntakken-Oost 2005: Biologische monitoring zoete rijkswateren.*RIZA rapport nr 2007.031. Ministerie van Verkeer en Waterstaat.

SCHAEPMAN-STRUB, G., SCHAEPMAN, M.E., PAINTER, T.H., DANGEL, S. & MARTONCHIK, F.V. (2006) “Reflectance quantities in optical remote sensing – definitions and case studies”, *Remote Sensing of Environment,* 103(1) pp.27-42.

SCHAMINÉE, J.H.J., STORTELDER, A.H.F., HOMMEL, P.W.F.M. & VAN DORT, K. (1995-1999) *Vegetatie van Nederland (5 delen).* Uppsala: Opulus.

SIMIC, A. & CHEN, J.M. (2008) "Refining a hyperspectral and multiangle measurement concept for vegetation structure assessment", *Canadian Journal of Remote Sensing,* 34(3), pp. 174-191.

VAN DE VEN, G.P. (1993) *Leefbaar laagland.* Utrecht: Matrijs.

VAN DER MOLEN, D.T., AARTS, H.P.A., BACKX, J J.G.M., GEILEN, E.F.M. & PLATTEEUW, M. (2000) *Rijkswateren-ecotopen-stelsel: aquatisch.* Lelystad [etc.] : Ministerie van Verkeer en Waterstaat, Directoraat-Generaal Rijkswaterstaat, RIZA Rijksinstituut voor Integraal Zoetwaterbeheer en Afvalwaterbehandeling

VAN VELZEN, E.H., JESSE, P., CORNELISSEN, P. & COOPS, H. (2003) *Stromingsweerstand vegetatie in uiterwaarden, deel 1 handboek.* RIZA rapport 2003.028. Arnhem: RIZA.

VERHOEF, W. (1984) "Light scattering by leaf layers with application to canopy reflectance modeling: The SAIL model", *Remote Sensing of Environment*, 16(2), pp. 125-141.

VERHOEF, W. & BACH, H. (2007) "Coupled soil-leaf-canopy and atmosphere radiative transfer modeling to simulate hyperspectral multi-angular surface reflectance and TOA radiance data", *Remote Sensing of Environment*, 109(2), pp. 166-182.

VERRELST, J., GEERLING, G.W., SYKORA, K.V. & CLEVERS, J.G.P.W. (2009) "Mapping of aggregated floodplain plant communities using image fusion of CASI and LiDAR data", *International Journal of Applied Earth Observation and Geoinformation,* 11(1), pp. 83-94.

VERRELST, J., SCHAEPMAN, M.E., KOETZ, B. & KNEUBÜHLER, M. (2008) "Angular sensitivity analysis of vegetation indices derived from CHRIS/PROBA data", *Remote Sensing of Environment*, 112(5), pp. 2341-2353.

VERRELST, J., SCHAEPMAN, M., MALENOVSKY, Z.& CLEVERS, J. (2009) (Manuscript Draft) "Effects of woody elements on forest canopy chlorophyll content retrieval", *Remote Sensing of Environment.*

VUOLO, F., DINI, L. & D’URSO, G. (2005) “Assessment of LAI retrieval accuracy by inverting a RT model and a simple empirical model with multiangular and hyperspectral CHRIS/PROBA data from SPARC”. In: European Space Agency. *Proc. Of the 3rd ESA CHRIS/Proba Workshop*. Frascati, Italy, 21-23 March (ESA SP-593, June 2005), ESA/ESRIN.

WEISS, M., BARET, F., MYNENI, R.B., PRAGNÈRE, A. & KNYAZIKHIN, Y. (2000) "Investigation of a model inversion technique to estimate canopy biophysical variables from spectral and directional reflectance data", *Agronomie*, 20(1), pp. 3-22.

WILLEMS, D., BERGWERFF, J. & GEILEN, N. (2007). *Rijkswatere-ecotopenkartering: RWES-terrestrisch.* RIZA rapport 2007.030.

WIDLOWSKI, J-L., PINTY, B., LAVERGNE, T., VERSTRAETE, M.M. & GOBRON, N. (2005) "Using 1-D models to interpret the reflectance anisotropy of 3-D canopy targets: issues and caveats", *IEEE Transactions on Geoscience and Remote Sensing,* 43, pp. 2008–2017.

WU, T.-F., LIN, C.-J. & WENG, R.C. (2004) "Probability estimates for multi-class classification by pairwise coupling", *Journal of Machine Learning Research,* 5, pp. 975-1005.

E-books / Websites

ARK NATUURONTWIKKELING. (2008) *Cyclisch verjongen.* Available at: http://www.ark.eu. (Accessed at: 10 November 2008).

BIERBZA NATIONAL PARK. (2008) *Bierbzanzki Park Narodowy.* Available at: http://www.biebrza.org.pl/. (Accessed: 10 November 2008).

CANADA CENTRE FOR REMOTE SENSING. (2009) *Glossary of Remote Sensing terms:Kkappa Coeffficient.* Available at: http://www.ccrs.nrcan.gc.ca/glossary/index_e.php?id=2967/. (Accessed: 30 April 2009).

EAROPEAN SPACE AGENCY. (2008) *ESA Earthnet online: PROBA.* Available at: http://earth.esa.int/proba/. (Accessed: 8 December 2008)

HSU, C.-W., CHANG, C.-C. & LIN, C-J. (2009). *A Practical Guide to Support Vector Classification.* [e-book] Department of Computer Science, Taiwan. Available at: http://www.csie.ntu.edu.tw/~cjlin/. (Accessed: 13 August 2009).

IPCC (2007) *Fourth assessment report climage change.* Paris: WMO UNEP. Available at: http://news.bbc.co.uk/2/shared/bsp/hi/pdfs/02_02_07_climatereport.pdf. (Accessed: 13 August 2009

KNMI (2006) *Klimaatscenario's voor Nederland.* Available at: http://www.knmi.nl/klimaatscenarios/. (Accessed: 13 August 2009).

NEDERLAND LEEFT MET WATER. (2008) *Nederland leeft met water.* Available at: www.nederlandleeftmetwater.nl (Accessed: 10 November 2008).

MINISTERIE VAN V&W (2005) *PKB deel 1Ruimte voor de rivier: ontwerp planologische kernbeslissing.* Available at: http://www.ruimtevoorderivier.nl/files/Files/Rapporten%20ed/PKB%201/pkb-deel-a.pdf. (Accessed: 13 August 2009).

MINISTERIE VAN V&W (2007) *PKB deel 4 Ruimte voor de rivier: nota van toelichting.* Available at: http://www.ruimtevoorderivier.nl/files/Files/Rapporten%20ed/PKB%204/PKB%204%20Vastgesteld%20Besluit%20H01-H05.pdf. (Accessed: 13 August 2009).

RIJKSWATERSTAAT. (2008-1) *Water.* Available at: www.rijkswaterstaat.nl/. (Accessed: 10 November 2008).

Appendices

Appendix I: Information about image acquisition

PROBA-1 satellite

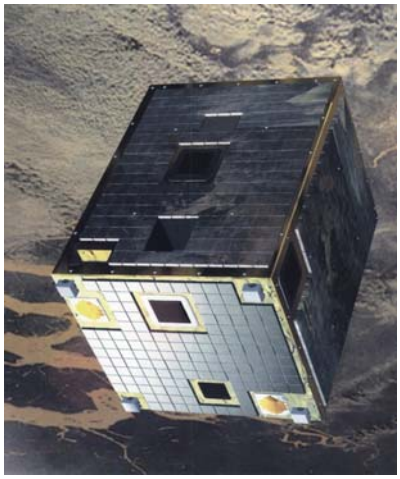

http://www.lamma.rete.toscana.it

CHRIS sensor

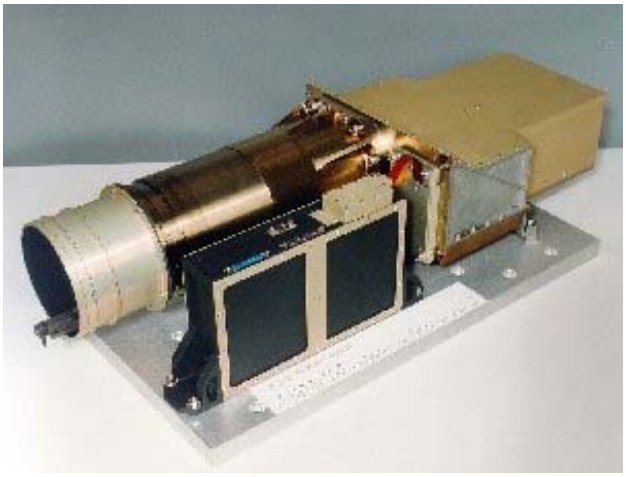

http://www.chris-proba.org.uk/

Polar plot

The polar plot shows the position of the sensor when the 5 angular images were acquired

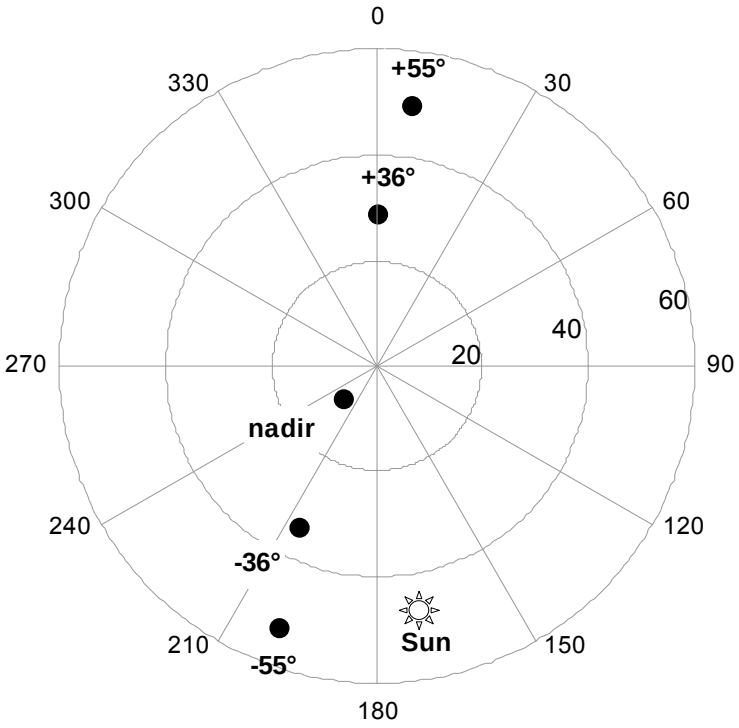

Solar zenith angle: 46°
Solar azimuth angle: 170°

CHRIS Mode 3, bands & wavelengths

1	442.6000 nm
2	490.5000 nm
3	530.3000 nm
4	551.7000 nm
5	570.4000 nm
6	631.9000 nm
7	661.8000 nm
8	675.2000 nm
9	698.1000 nm
10	707.1000 nm
11	713.3000 nm
12	742.5000 nm
13	752.9000 nm
14	781.8000 nm
15	873.2000 nm
16	896.6000 nm
17	911.0000 nm
18	1020.4000 nm

Image acquisition
RGB-colour composite (Red: band 8, Green: band 4, Blue: band 2)
ESA PROBA mission, Sira Technology Ltd.

Date of acquisition: September 2005
Fly-by Time : 11:06
Platform Altitude : 644 m

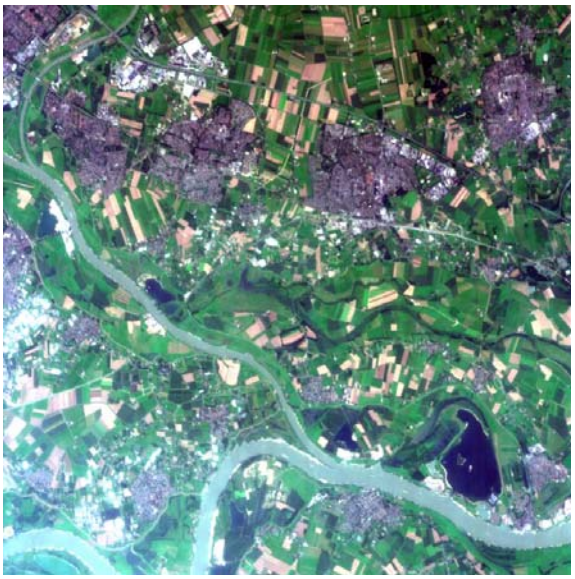

Fly-by Zenith Angle : 0 (nadir)
Observation Zenith Angle : 8.67
Observation Azimuth Angle : 224.81

Fly-by Zenith Angle : +36
Observation Zenith Angle : 28.64
Observation Azimuth Angle : 0.71

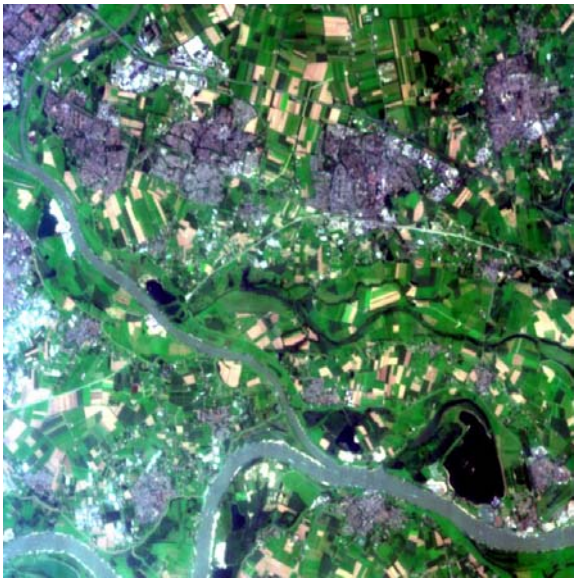

Fly-by Zenith Angle : -36
Observation Zenith Angle : 33.77
Observation Azimuth Angle : 205.54

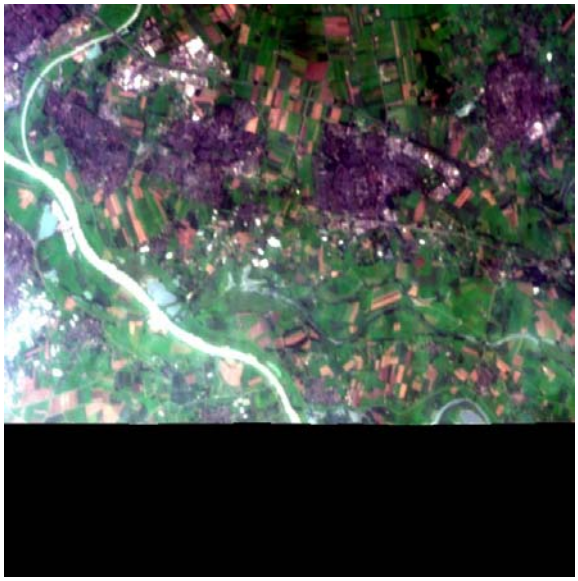

Fly-by Zenith Angle : +55
Observation Zenith Angle : 49.44
Observation Azimuth Angle : 8.28

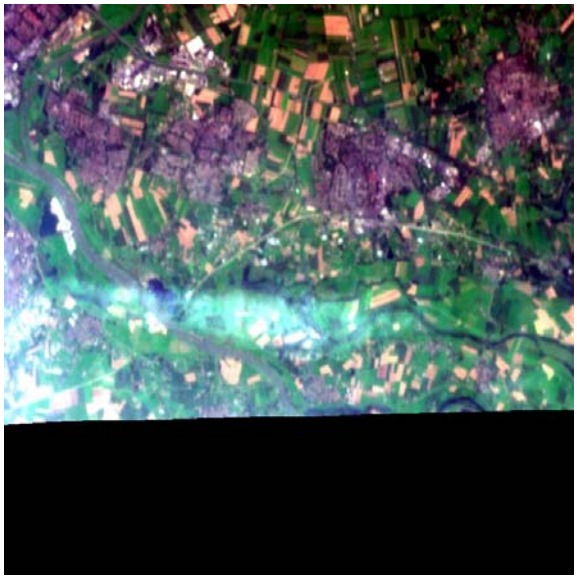

Fly-by Zenith Angle : -55
Observation Zenith Angle : 52.95
Observation Azimuth Angle : 201.21

Appendix II: Spectral signatures for all classes

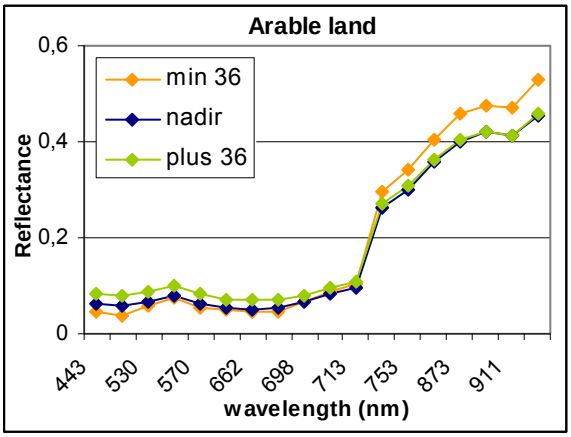

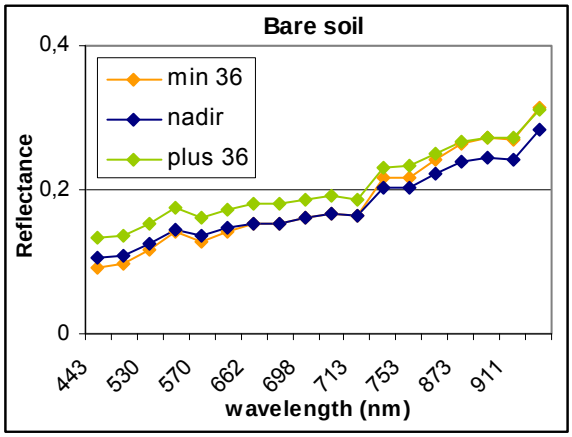

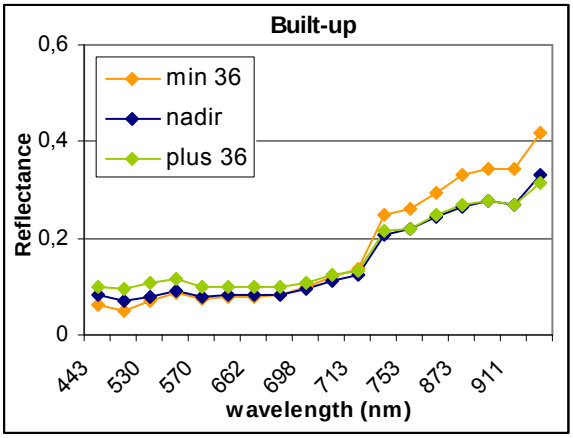

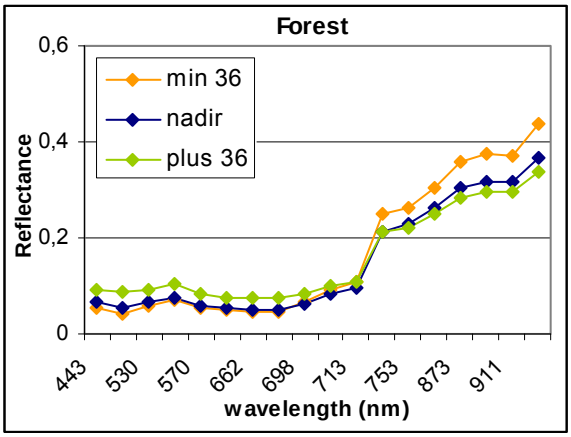

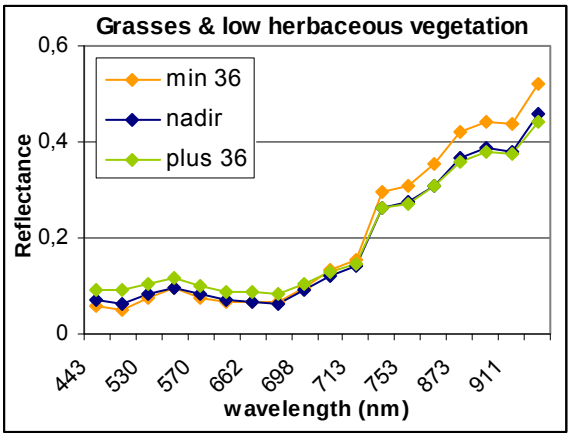

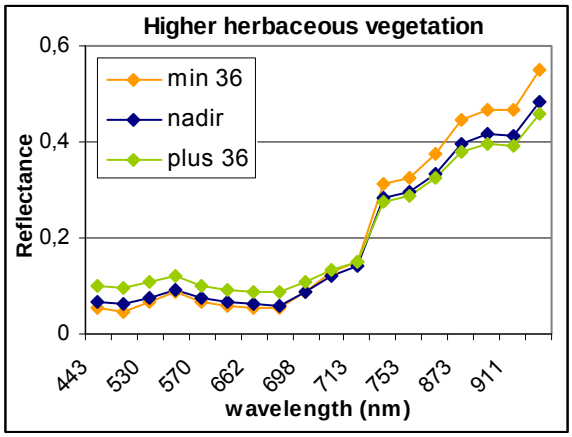

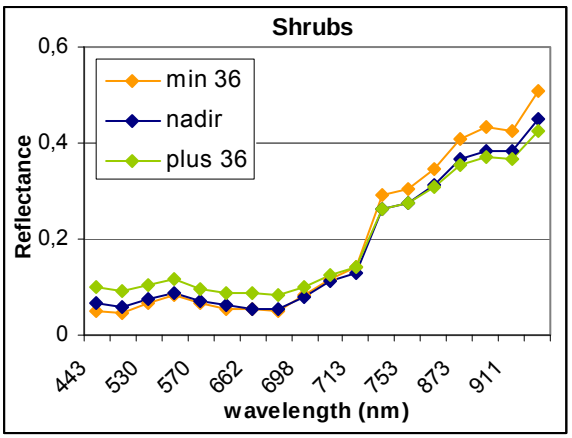

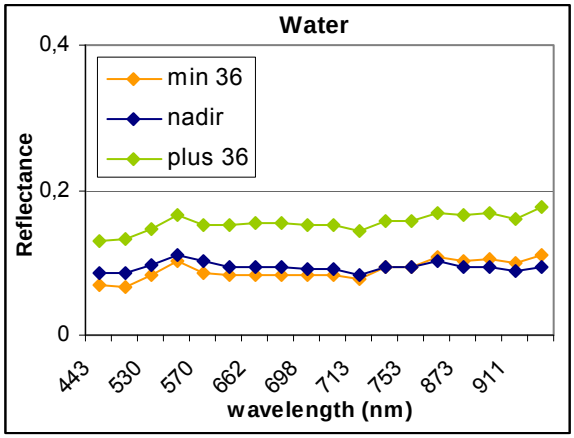

Appendix III: Division of RWS classes into the 8 new classes

Bare and pioneer communities	
RWS code	**Description (Dutch)**
II.2	zoete zandplaten
OK-1	Onbegroeide oeverwal
K4	Kale oever
O-UK-1	Onbegroeide oeverwal of uiterwaard
REST-U	Uiterwaard tijdelijk kaal
REST-T	Overstromingsvrij tijdelijk kaal
REST-O	Tijdelijk kaal
REST-O-U	Oeverwal of uiterwaard tijdelijk kaal
REST	Tijdelijk kaal

Grasses and low herbaceous vegetation	
RWS code	**Description (Dutch)**
VII.1	Moerassig overstromingsgrasland
VII.3	Produktiegrasland
UG-1	Natuurlijk uiterwaardgrasland
UG-2	Uiterwaard productiegrasland
HG-1	Overstromingsvrij natuurlijk grasland
HG-2	Overstromingsvrij productiegrasland
G1	Natuurlijk grasland
G1-2	Productie/natuurlijk grasland
G2	Productiegrasland
O-UG-1	Oeverwal of uiterwaard natuurlijk grasland
O-UG-2	Oeverwal of uiterwaard productiegrasland

Higher herbaceous vegetation	
RWS code	**Description (Dutch)**
IV.8	Soortenarm helofytenmoeras
IV.9	Soortenrijk riet met moerasplanten
UM_1	Oeverwal of uiterwaard riet
G5	Riet en overige helofyten
G6	Ruigte
O-UR-1	Oeverwal of uiterwaard ruigte
V.1	Soortenrijke moerasruigte
V.2	Soortenarme moerasruigte
UR-1	Uiterwaardruigte
HR-1	Overstromingsvrije ruigte
HM-1	Overstromingsvrij riet
UR-1	Uiterwaardruigte

Shrubs	
RWS code	**Description (Dutch)**
VI.2	Zachthout struweel
VI.3	Pionier zachthoutooibos
UB-2	Uiterwaardstruweel (<5m)
HB-2	Overstromingsvrij struweel
B4	Struweel
O-UB-2	Oeverwal of uiterwaard struweel

Forest

RWS code	Description (Dutch)
VI.4	Zachthoutooibos
VI.7	Griend
UB-1	Natuurlijk uiterwaardbos (>5m)
UB-3	Uiterwaardproductiebos
HB-1	Overstromingsvrij natuurlijk bos
HB-3	Overstromingsvrij productiebos
B1	Natuurlijk bos
O-UB-1	Oeverwal of uiterwaard natuurlijk bos
B2	Productiebos
VI.8	Productiebos in oever
O-UB-3	Oeverwal of uiterwaard productiebos

	Arable land (Maiz)
RWS code	**Description (Dutch)**
UA-1	Uiterwaardakker
HA-1	Overstromingsvrije akker
G3	Akker
IX.a	Akker in oever
O-UA-1	Oeverwal of uiterwaard akker

	Water
RWS code	**Description (Dutch)**
RzD	Diep zomerbed
RzM	Matig diep zomerbed
RzO	Ondiep zomerbed
RnM	Matig diepe nevengeul
RwO	Ondiep
RwM	Matig diep
RvM	Matig diep
RvD	Zeer diep
RwD	Zeer diep
RvO	Ondiep
I.1	dynamisch zoet tot zwak brak ondiep water

	Built-up
RWS code	**Description (Dutch)**
A	Bebouwd/verhard
O-UA-2	Bebouwde oeverwal of uiterwaard
III.2	Sterk dynamisch hard substraat onder invloed van zoet of brak water
III.3	Matig dynamisch hard substraat onder invloed van zoet water
UA-2	Bebouwde uiterwaard
HA-2	Overstromingsvrij bebouwd

Appendix IV: ROIs in Millingerwaard

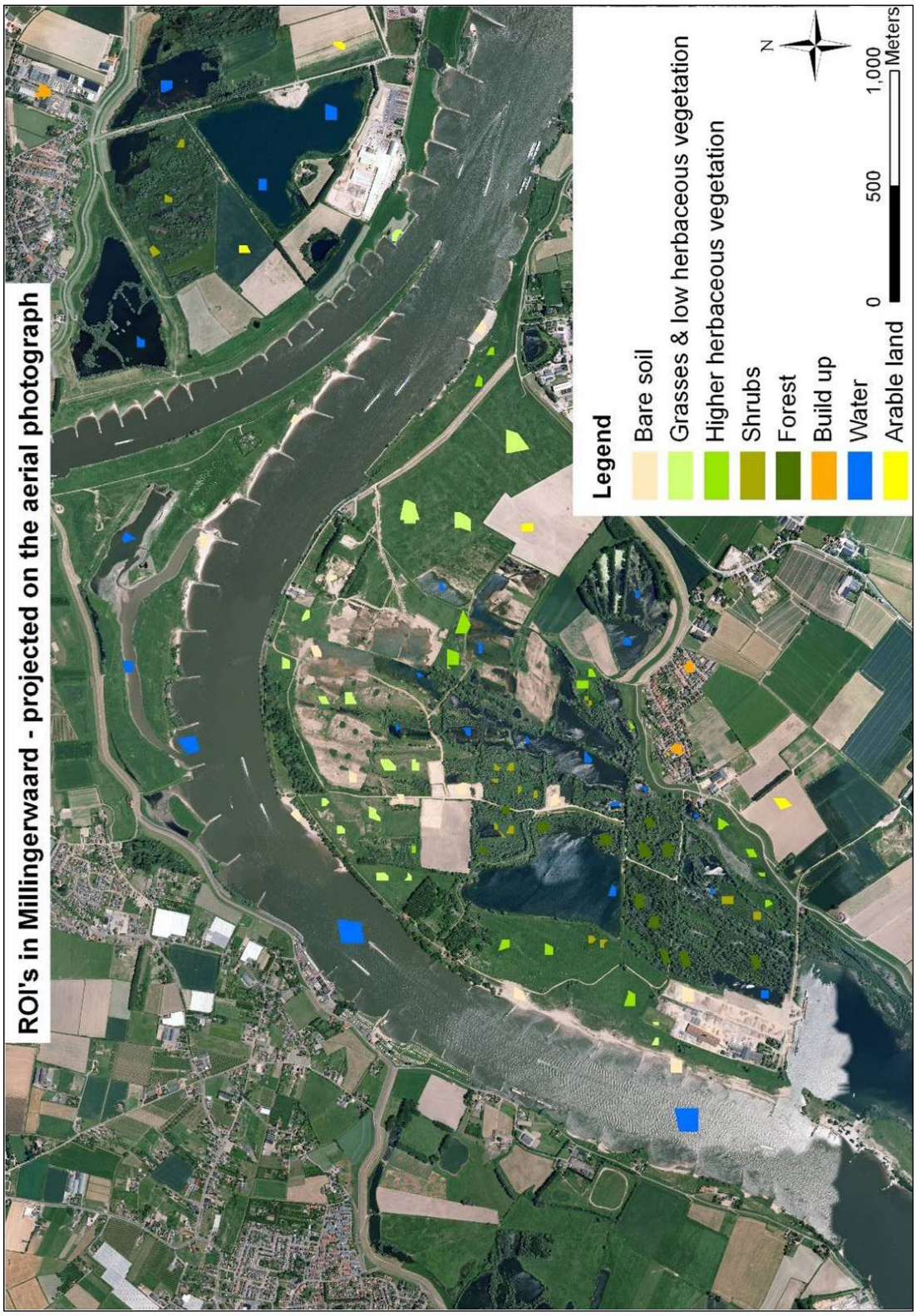

Appendix V: Parameters of vegetation structure classes for running the model FLIGHT

For 3D case only (forest class)					
Crown shape	**Exy (m)**	**Ez (m)**	**Min_HT (m)**	**Max_HT (m)**	**DBH (m)**
ellipsoid	3	8	1	10	0.4

Not varying parameters (same for each class; default values are taken)		
AER.OPT		0
SOILROUGH		0.08
LAD	**bins**	**value**
	0-10	0.015
	10-20	0.045
	20-30	0.074
	30-40	0.1
	40-50	0.123
	50-60	0.143
	60-70	0.158
	70-80	0.168
	80-90	0.174

Model parameters:

Fixed parameters			
MODE			r
NO_WVBANDS			18
SOLAR_ZENITH (degrees)			46
SOLAR_AZIMUTH (degrees)			170
	nadir	**+36**	**-36**
VIEW_ZENITH (degrees)	8.67	28.64	33.77
VIEW_AZIMUTH (degrees)	224.81	0.71	205.54

Vegetation structure class variables & parameters:

1st model run

	Variables			**Fixed parameters**	
Class	**Fcover**	**LAI (m²/m²)**	**PV**	**Scene**	**Leaf size (m)**
Herbaceous	0.6-1; step: 0.05	0-7; step: 0.5 until 5; step: 1 until 7	0.5-1; step: 0.1	1D	0.027
Shrubs	0.5-1; step: 0.05	0-7; step: 0.5 until 5; step: 1 until 7	0.5-1; step: 0.1	1D	0.02
Forest	0.2-1; step: 0.05	0-10; step: 0.5 until 5; step: 1 until 10	0.3-1; step: 0.1	3D	0.02

2nd model run

	Variables			**Fixed parameters**	
Class	**Fcover**	**LAI (m²/m²)**	**PV**	**Scene**	**Leaf size (m)**
Herbaceous	0.4-1; step: 0.05	1-10; step: 0.5 until 7; step: 1 until 10	1; no steps	1D	0.027
Shrubs	0.6-1; step: 0.05	1.5-12; step: 0.5 until 7; step: 1 until 12	0.5-0.95; step: 0.05	1D	0.02
Forest	0.8-1; step: 0.05	2.5-12; step: 0.5 until 7; step: 1 until 12	0.5-0.95; step: 0.05	3D	0.02

Input spectra

1st model run

Class	**Leaf**	**Background**	**Bark**
Herbaceous	Calamagrostis epigejos	sand	
Shrubs	Salix alba	average (water+grass & forest background)	Salix alba
Forest	Salix alba	forest background	Salix alba

2nd model run

Class	**Leaf**	**Background**	**Bark**
Herbaceous	Calamagrostis epigejos	0.95*forest background + 0.05*sand	
Shrubs	Salix alba	average (water+grass & forest background)	Salix alba
Forest	Salix alba	forest background	Salix alba

VEGETATION PARAMETERS

Scene (1D/3D)
1D indicates a "turbid medium". This is used for an area that is homogenous in coverage. Here it is used for the herbaceous and shrub classes. 3D is used for the forest class. Each tree is than represented by 3D shapes of cones and ellipsoids.

Fractional cover (0-1)
This is the fraction of ground covered by vegetation on vertical projection.

Leaf area index (m^2/m^2)
LAI is the mean one-sided green leaf area per unit ground area.

Fraction of photosynthetic vegetation (0-1)
This is the volume-fraction of photosynthetic vegetation within the vegetation. The PV, together with the NPV (fraction of woody vegetation / non-photosynthetic) is 1.

Background type (herbaceous, shrubs, forest)
For each vegetation structure class a different background type is used. The background type is defined as the type of soil or vegetation that grows underneath the vegetation or in the gaps within the vegetated area.

Only for the 3D case:

Crown shape (e/c/f)
The crown shape of the trees can be e (ellipsoid), c (cones) or f (field).

Crown radius (Exy) (m)

Centre to top distance (Ez) (m)
For crowns that are modelled as ellipsoids, this is half of the crown height.

Minimum height for the first branch (Min_HT) (m)

Maximum height for the first branch (Max_HT) (m)

The first branches of the crowns are randomly distributed between the minimum and maximum height for the first branch.

Diameter at breast height (DBH) (m)
This is the diameter of the trunk, measured at breast height.

GENERAL PARAMETERS (non-varying)

Mode of operation (MODE) (f,i,s,r)
This is the mode in which FLIGHT will operate. F means forward modelling, i = image, s = solid-object, r = reverse. For this research the reverse modelling option was used. In reverse mode the model output gives the simulated (BRF) reflectance in one specified view direction, for a certain class. This takes less calculation time than the forward mode in which the reflection in all direction is simulated.

Number of wavebands (NO_WVBANDS)
This is the number of wavebands that is used for the simulations. In this case it is 18, the same number as the CHRIS wavebands.

Number of photons (NO_PHOTONS)
This is the total number of photon paths that is simulated.

Leaf angle distribution (LAD) (1-9)
This measure indicates how the leaves are distributed in the crowns and in which angles. It is expressed as a fraction lying within 10 degree bins of 0-10, 10-20, 20-30…80-90.

Soil roughness index (SOILROUGH) (0-1)
This indicates how rough the soil is. A Lambertian soil receives the value 0, a rough slope (mean slope of 60 degrees) is indicated by 1.

Solar zenith angle (degrees)
The solar zenith angle is from the moment that the satellite obtained the image.

Solar azimuth angle (degrees)
The solar azimuth angle is from the moment that the satellite obtained the image.

View zenith angles (degrees)
The view zenith angle is indicated for the three angular CHRIS images that are used. It differs a little bit from the expected 0˚ and +/-36˚.

View azimuth angles (degrees)
The view azimuth angle is indicated for the three angular CHRIS images that are used.

Appendix VI: Validation points LAI and fCover from 2004. Plotted on the aerial photograph and the CHRIS nadir classification.

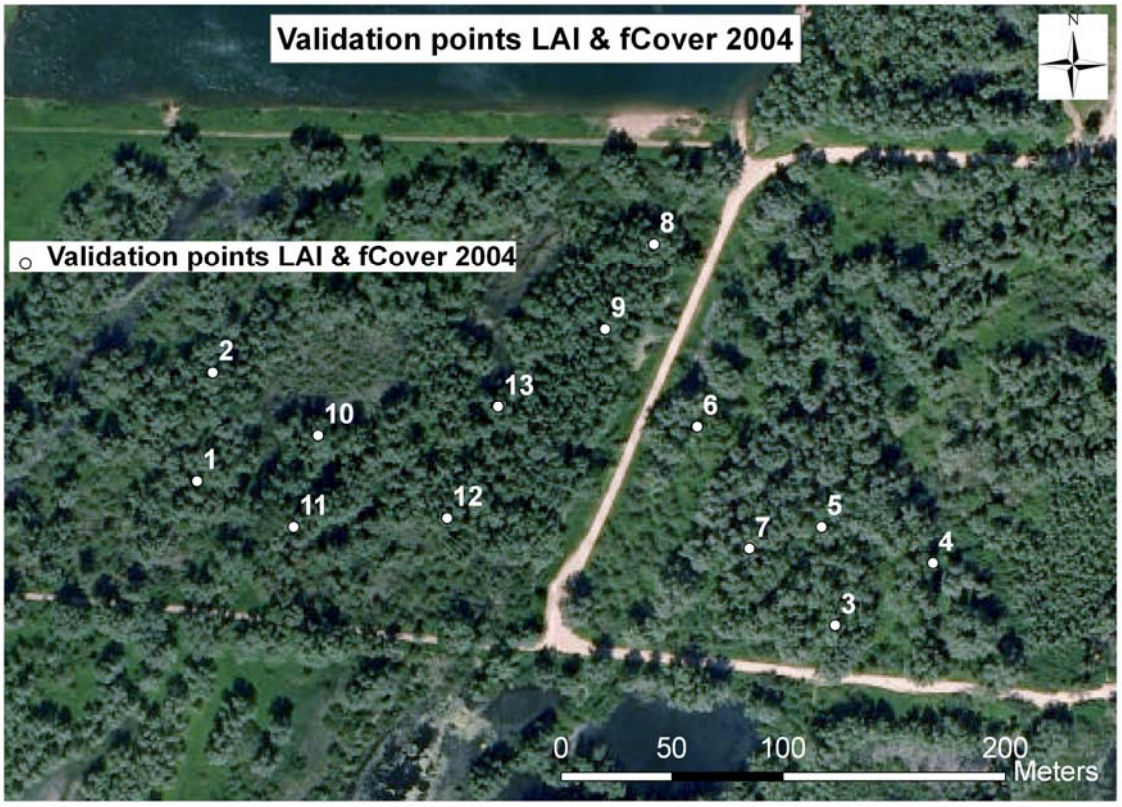

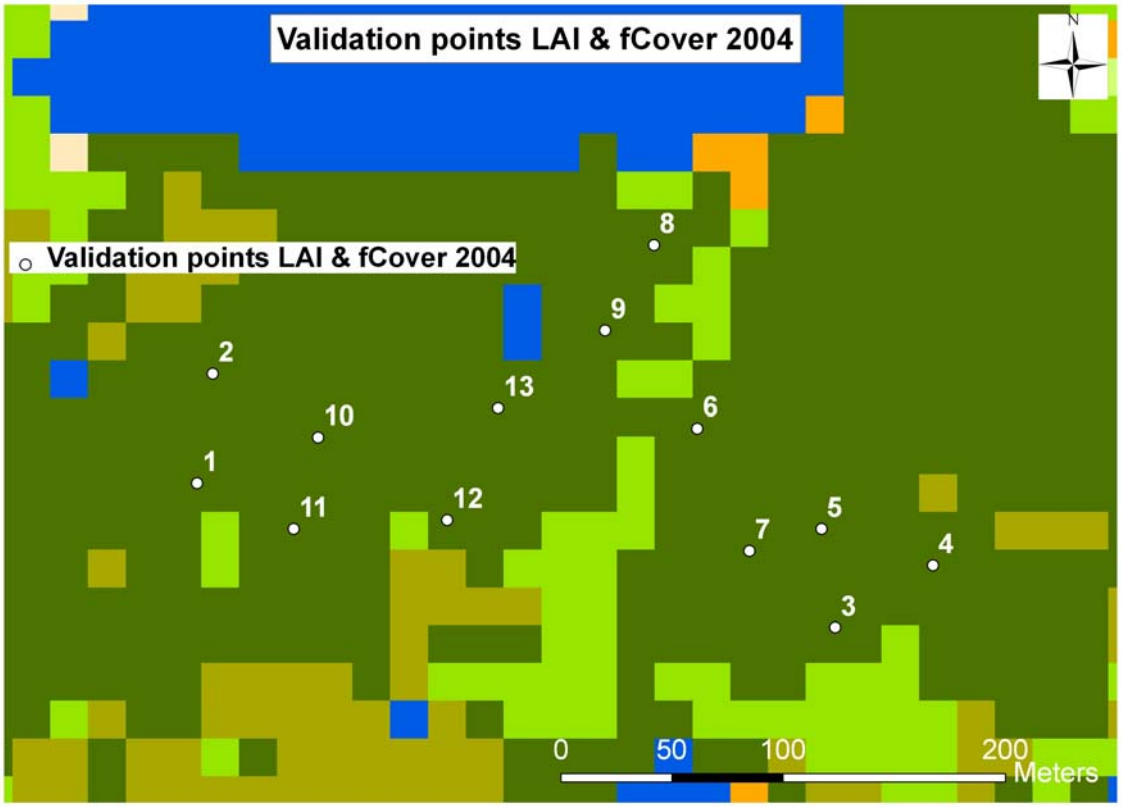

Validation points 2004

LAI

Plot.no	CE_LAIeff(m2/m2)	LAI_2nd_modelrun_nadir	LAI_2nd_modelrun_min36	LAI_2nd_modelrun_plus36
1	3,9	3	2,5	3
2	3,4	2,5	2,5	2,5
3	4	2,5	2	2,5
4	3,4	3,5	3	3
5	3,9	3,5	2,5	3
6	3,5	3	2,5	2,5
7	3,8	4	2,5	3
8	3	2,5	2,5	2,5
9	3,4	2,5	1,5	2
10	2,9	4,5	2,5	2,5
11	3,3	3	2,5	2,5
12	3,5	3	3	3
13	3,7	3	2,5	2,5

outliers

CE_LAIeff = measured effective LAI, obtained with hemispherical photography and CAN_EYE
LAI_2nd_modelrun_nadir =
modelled LAI for the CHRIS nadir direction, obtained from the 2nd modelrun
LAI_2nd_modelrun_min36 =
modelled LAI for the CHRIS backscattering direction, obtained from the 2nd modelrun
LAI_2nd_modelrun_plus36 =
modelled LAI for the CHRIS forward scattering direction, obtained from the 2nd modelrun

fCover

Plot.no	CE_fCover	fCover_2ndmodelrun_nadir	fCover_2nd_modelrun_min36	fCover_2nd_modelrun_plus36
1	0,96	0,8	1	0,8
2	0,94	0,8	0,85	0,9
3	0,95	0,75	0,9	0,7
4	0,93	0,8	0,8	0,8
5	0,97	0,9	1	0,9
6	0,94	0,9	0,85	0,85
7	0,94	1	1	0,8
8	0,89	0,8	1	0,85
9	0,91	1	0,7	0,7
10	0,84	0,8	0,85	0,9
11	0,93	0,8	1	0,85
12	0,93	0,8	0,85	0,8
13	0,92	0,8	0,85	0,9

outliers

CE_fCover = fCover, obtained with hemispherical photography and CAN_EYE
fCover_2nd_modelrun_nadir =
modelled fCover for the CHRIS nadir direction, obtained from the 2nd modelrun
fCover_2nd_modelrun_min36 =
modelled fCover for the CHRIS back scattering direction, obtained from the 2nd modelrun
fCover_2nd_modelrun_plus36 =
modelled fCover for the CHRIS forward scattering direction, obtained from the 2nd modelrun

Appendix VII: Validation points LAI from 2005. Plotted on the aerial photograph and the CHRIS nadir classification

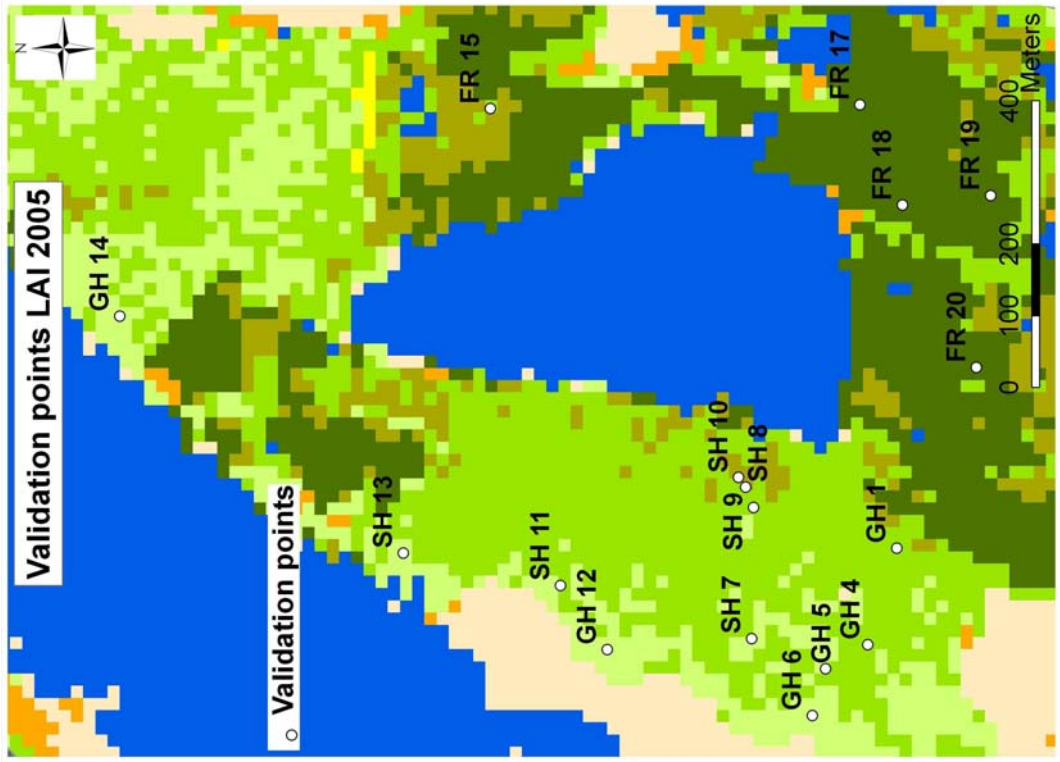

Validation points 2005

Plot code	LAI combined HP/TRAC	LAI 2nd modelrun (nadir)	LAI 2nd modelrun (min 36)	LAI 2nd modelrun (plus 36)
GH 1	9,6400	2,5000	3,0000	4,5000
GH 2	3,0300	3,0000	2,0000	3,0000
GH 3	2,5800	3,0000	2,0000	3,0000
GH 4	3,5900	4,0000	2,5000	4,5000
GH 5	4,1500	4,0000	3,0000	6,0000
GH 6	3,0300	3,0000	2,5000	3,0000
SH 7	4,5800	3,5000	3,5000	6,0000
SH 8	2,8200	11,9800	12,0000	12,0000
SH 9	2,8700	4,5000	3,5000	6,0000
SH 10	4,0300	3,5000	2,5000	4,5000
SH 11	4,7000	10,0000	3,0000	4,5000
GH 12	4,6000	3,0000	2,5000	4,0000
SH 13	5,7600	6,0000	2,5000	4,0000
GH 14	4,6000	3,5000	3,0000	4,5000
FR 15	4,4500	2,5000	3,5000	4,5000
FR 17	7,0200	3,0000	2,5000	3,0000
FR 18	7,6100	2,5000	2,5000	2,5000
FR 19	6,7900	2,0000	2,0000	2,5000
FR 20	5,0300	4,5000	3,0000	3,0000

outliers

GH = validation point in the grasses&herbaceous class
SH = validation point in the shrub class
FR = validation point in the forest class

LAI combined HP/TRAC = LAI obtained with combined hemispherical photography and TRAC measurements.
LAI_2nd_modelrun(nadir) = modelled LAI for the CHRIS nadir direction, obtained from the 2nd modelrun.
LAI_2nd_modelrun(min36) = modelled LAI for the CHRIS back scattering direction, obtained from the 2nd modelrun.
LAI_2nd_modelrun(plus) = modelled LAI for the CHRIS forward scattering direction, obtained from the 2nd modelrun.

Appendix VIII: Separability values ROIs

Input File: CHRIS nadir
ROI Name: (Jeffries-Matusita, Transformed Divergence)

Water [Blue] 385 points:
Bare Soil [Thistle] 93 points: (1.99862393 1.99999999)
Forest [Green3] 88 points: (1.99999650 2.00000000)
Shrubs [Green1] 84 points: (1.99999989 2.00000000)
Higher herbaceous [Cyan3] 124 points: (1.99999642 2.00000000)
Grass & Low herbaceous [Cyan1] 149 points: (1.99999915 2.00000000)
Built-up [Orange1] 123 points: (1.99990476 2.00000000)
Agricultural [Yellow] 79 points: (2.00000000 2.00000000)

Bare Soil [Thistle] 93 points:
Water [Blue] 385 points: (1.99862393 1.99999999)
Forest [Green3] 88 points: (2.00000000 2.00000000)
Shrubs [Green1] 84 points: (1.99999990 2.00000000)
Higher herbaceous [Cyan3] 124 points: (1.99988437 2.00000000)
Grass & Low herbaceous [Cyan1] 149 points: (1.99979736 2.00000000)
Built-up [Orange1] 123 points: (1.99991421 2.00000000)
Agricultural [Yellow] 79 points: (2.00000000 2.00000000)

Forest [Green3] 88 points:
Water [Blue] 385 points: (1.99999650 2.00000000)
Bare Soil [Thistle] 93 points: (2.00000000 2.00000000)
Shrubs [Green1] 84 points: (1.98509284 1.99999598)
Higher herbaceous [Cyan3] 124 points: (1.98601952 1.99999400)
Grass & Low herbaceous [Cyan1] 149 points: (1.99995479 2.00000000)
Built-up [Orange1] 123 points: (1.99998975 2.00000000)
Agricultural [Yellow] 79 points: (2.00000000 2.00000000)

Shrubs [Green1] 84 points:
Water [Blue] 385 points: (1.99999989 2.00000000)
Bare Soil [Thistle] 93 points: (1.99999990 2.00000000)
Forest [Green3] 88 points: (1.98509284 1.99999598)
Higher herbaceous [Cyan3] 124 points: (1.92044373 1.99984125)
Grass & Low herbaceous [Cyan1] 149 points: (1.99941992 1.99999995)
Built-up [Orange1] 123 points: (1.99999678 2.00000000)
Agricultural [Yellow] 79 points: (1.99999984 2.00000000)

Higher herbaceous [Cyan3] 124 points:
Water [Blue] 385 points: (1.99999642 2.00000000)
Bare Soil [Thistle] 93 points: (1.99988437 2.00000000)
Forest [Green3] 88 points: (1.98601952 1.99999400)
Shrubs [Green1] 84 points: (1.92044373 1.99984125)
Grass & Low herbaceous [Cyan1] 149 points: (1.76135549 1.90461146)
Built-up [Orange1] 123 points: (1.99981010 1.99999997)
Agricultural [Yellow] 79 points: (1.99999933 2.00000000)

Grass & Low herbaceous [Cyan1] 149 points:
Water [Blue] 385 points: (1.99999915 2.00000000)
Bare Soil [Thistle] 93 points: (1.99979736 2.00000000)
Forest [Green3] 88 points: (1.99995479 2.00000000)
Shrubs [Green1] 84 points: (1.99941992 1.99999995)
Higher herbaceous [Cyan3] 124 points: (1.76135549 1.90461146)
Built-up [Orange1] 123 points: (1.99983315 2.00000000)
Agricultural [Yellow] 79 points: (1.99998508 2.00000000)

Built-up [Orange1] 123 points:
Water [Blue] 385 points: (1.99990476 2.00000000)
Bare Soil [Thistle] 93 points: (1.99991421 2.00000000)
Forest [Green3] 88 points: (1.99998975 2.00000000)
Shrubs [Green1] 84 points: (1.99999678 2.00000000)
Higher herbaceous [Cyan3] 124 points: (1.99981010 1.99999997)
Grass & Low herbaceous [Cyan1] 149 points: (1.99983315 2.00000000)
Agricultural [Yellow] 79 points: (2.00000000 2.00000000)

Agricultural [Yellow] 79 points:
Water [Blue] 385 points: (2.00000000 2.00000000)
Bare Soil [Thistle] 93 points: (2.00000000 2.00000000)
Forest [Green3] 88 points: (2.00000000 2.00000000)
Shrubs [Green1] 84 points: (1.99999984 2.00000000)
Higher herbaceous [Cyan3] 124 points: (1.99999933 2.00000000)
Grass & Low herbaceous [Cyan1] 149 points: (1.99998508 2.00000000)
Built-up [Orange1] 123 points: (2.00000000 2.00000000)

Appendix IX: Results from other classification methods

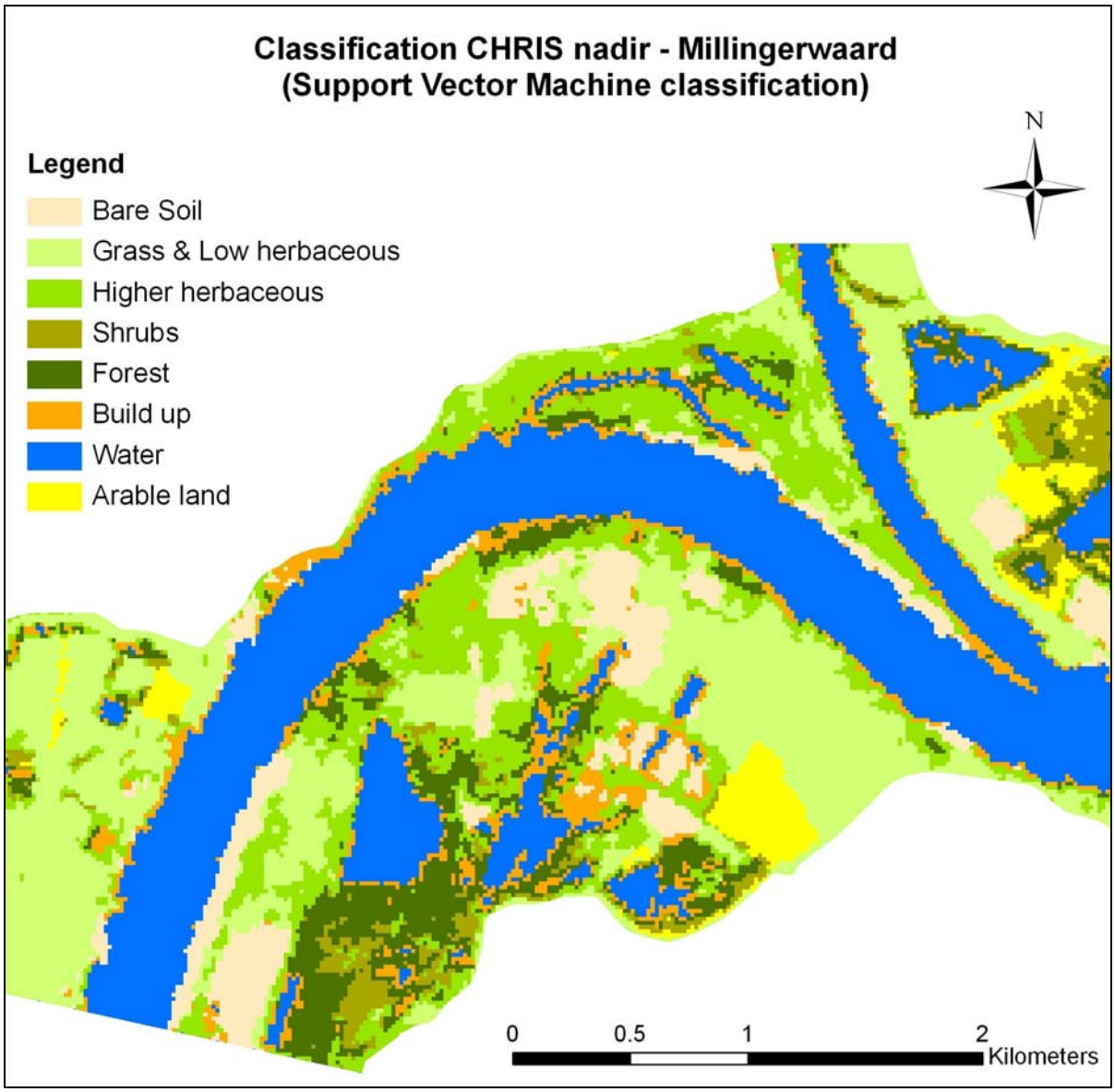

Ground truth	Bare soil	Grass & low herbaceous	Higher herbaceous	Shrubs	Forest	Arable land	Water	Build up	Total
Bare soil	7	2	1		2			5	17
Grass & low herbaceous	1	23	4	1	4	4	1	1	39
Higher herbaceous		4	4	1	2				11
Shrubs		1	2	5	1	3			12
Forest		2	4	3	15		1	1	26
Arable land		1	1	3		13		1	19
Water			1		2		18	2	23
Build up	5	1			1		1	5	13
Total	13	34	17	13	27	20	21	15	160

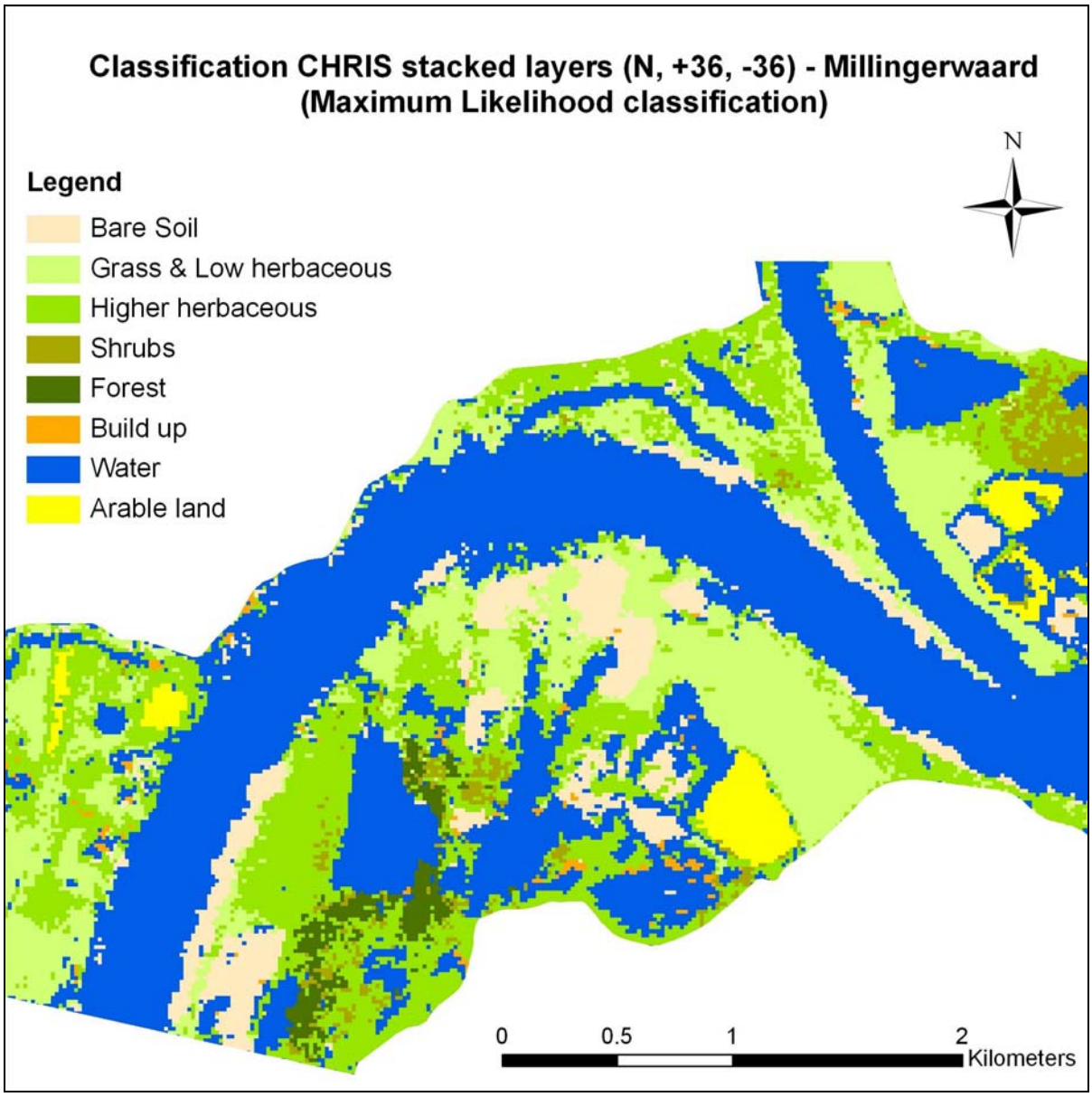

Ground truth	Bare soil	Grass & low herbaceous	Higher herbaceous	Shrubs	Forest	Arable land	Water	Build up	Total
Bare soil	6	1	2				6	2	17
Grass & low herbaceous		14	7	1		1	15	1	39
Higher herbaceous		4	4	1			2		11
Shrubs			2	6			4		12
Forest			10	3	4		8	1	26
Arable land						11	8		19
Water			1				22		23
Build up							9	4	13
Total	6	19	26	11	4	12	74	8	160

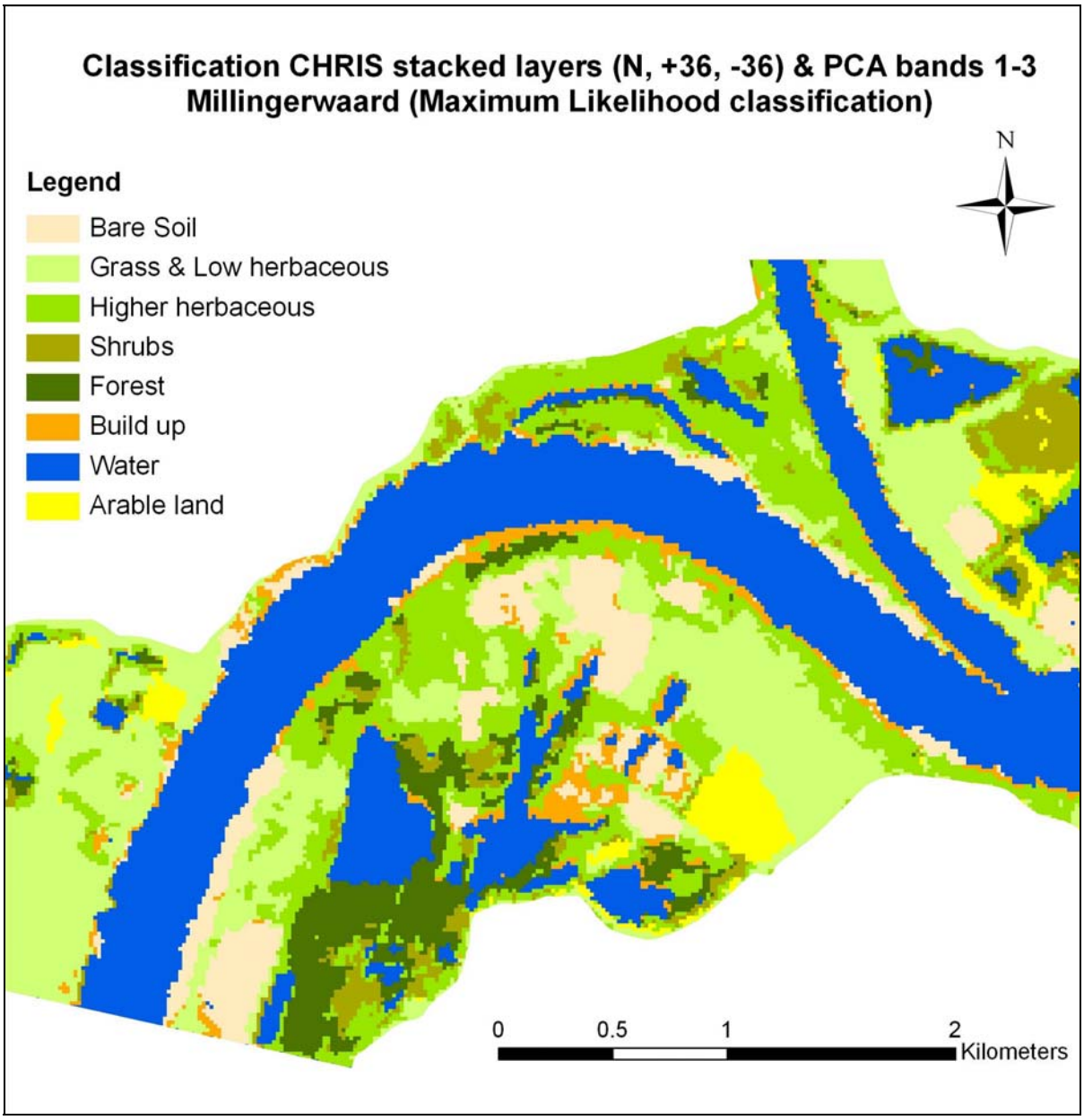

Ground truth	Bare soil	Grass & low herbaceous	Higher herbaceous	Shrubs	Forest	Arable land	Water	Build up	Total
Bare soil	7	2	2		1		1	4	17
Grass & low herbaceous		21	6	3	2	2	4	1	39
Higher herbaceous		5	3	2	1				11
Shrubs			2	8	1	1			12
Forest		1	5	4	13	1	2		26
Arable land		1	1	2	1	13		1	19
Water			3				19	1	23
Build up	5	1			1		2	4	13
Total	12	31	22	19	20	17	28	11	160

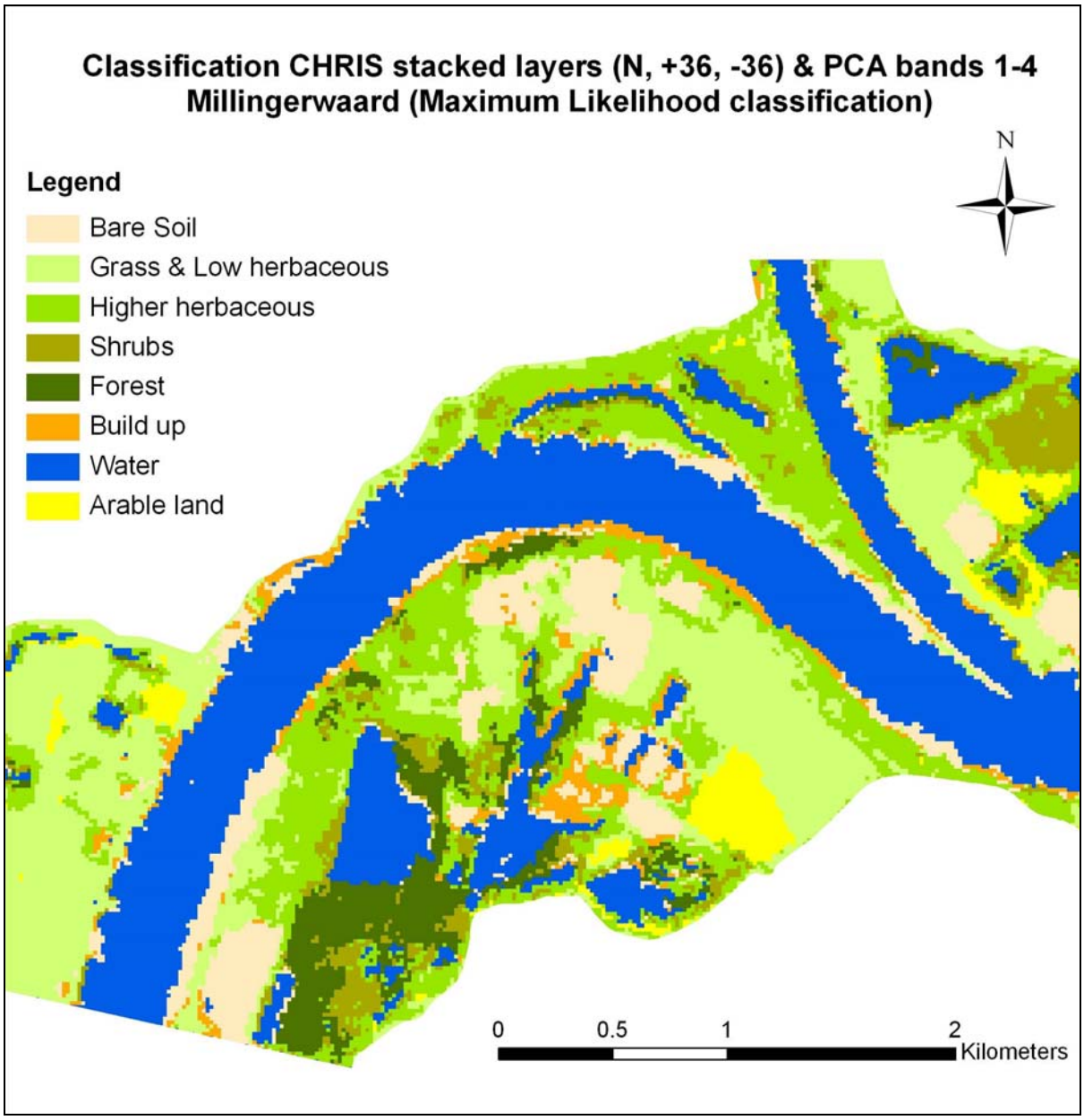

Ground truth	Bare soil	Grass & low herbaceous	Higher herbaceous	Shrubs	Forest	Arable land	Water	Build up	Total
Bare soil	9	2	1	1	1			3	17
Grass & low herbaceous		23	5	2	2	2	4	1	39
Higher herbaceous		4	6	1					11
Shrubs		1	1	8	1	1			12
Forest		1	9	4	9	1	2		26
Arable land		1	1	2	1	13	1		19
Water			2	1			19	1	23
Build up	6	1			1		2	3	13
Total	15	33	25	19	15	17	28	8	160

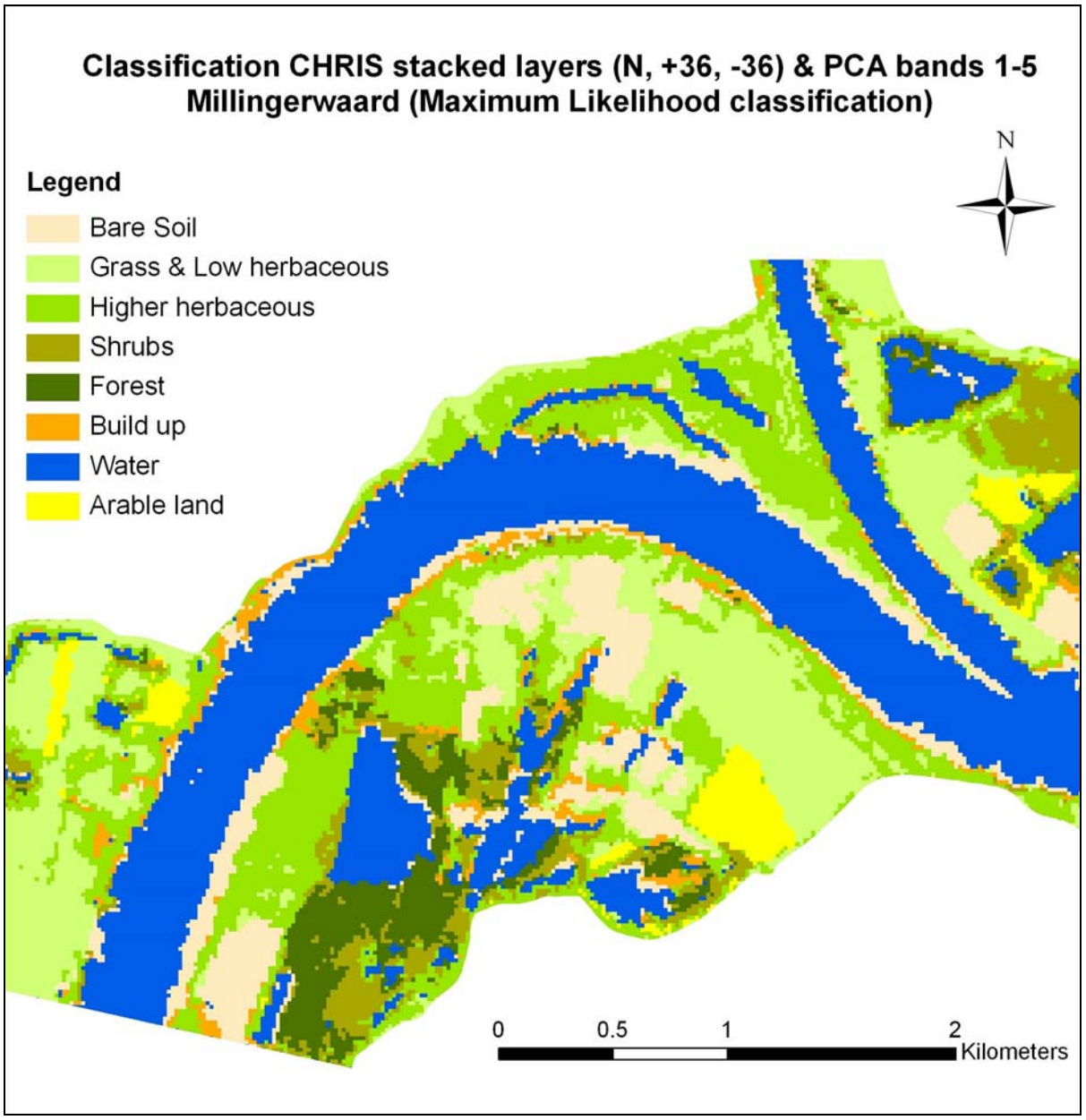

Ground truth	Bare soil	Grass & low herbaceous	Higher herbaceous	Shrubs	Forest	Arable land	Water	Build up	Total
Bare soil	9		2	1	1			4	17
Grass & low herbaceous	1	24	4	3	3	1	3		39
Higher herbaceous		4	6	1					11
Shrubs		1	2	7	1	1			12
Forest		1	6	3	13		2	1	26
Arable land	1	1	2	2	1	12			19
Water			2				20	1	23
Build up	8	1	1		1			2	13
Total	19	32	25	17	20	14	25	8	160

Appendix X: LAI results for the forest class, modelled as 3D medium with the model FLIGHT

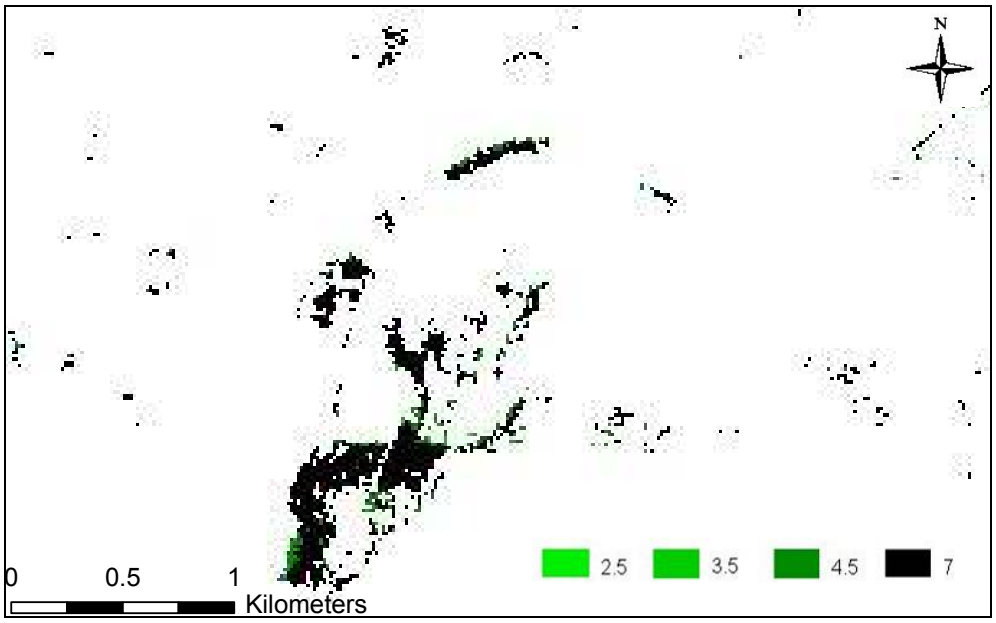

LAI map of the forest class, modelled as 3D medium, in Millingerwaard for the nadir direction.

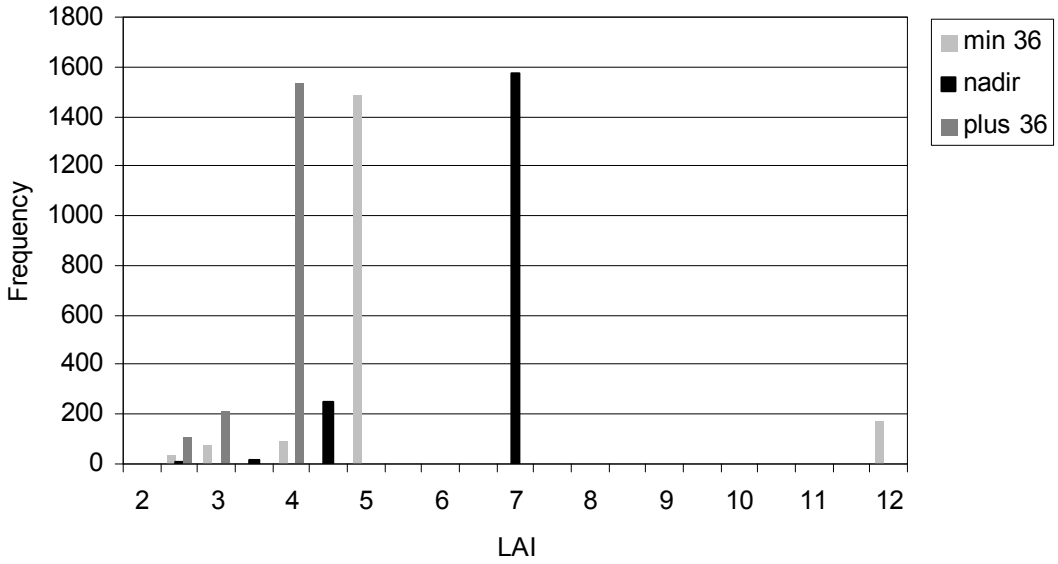

Histogram of LAI for the forest class, modelled as 3D medium, in Millingerwaard for the nadir, backward scattering and forward scattering direction.

Appendix XI: LAI results for the Gelderse Poort in the nadir and forward scattering direction obtained with the model FLIGHT

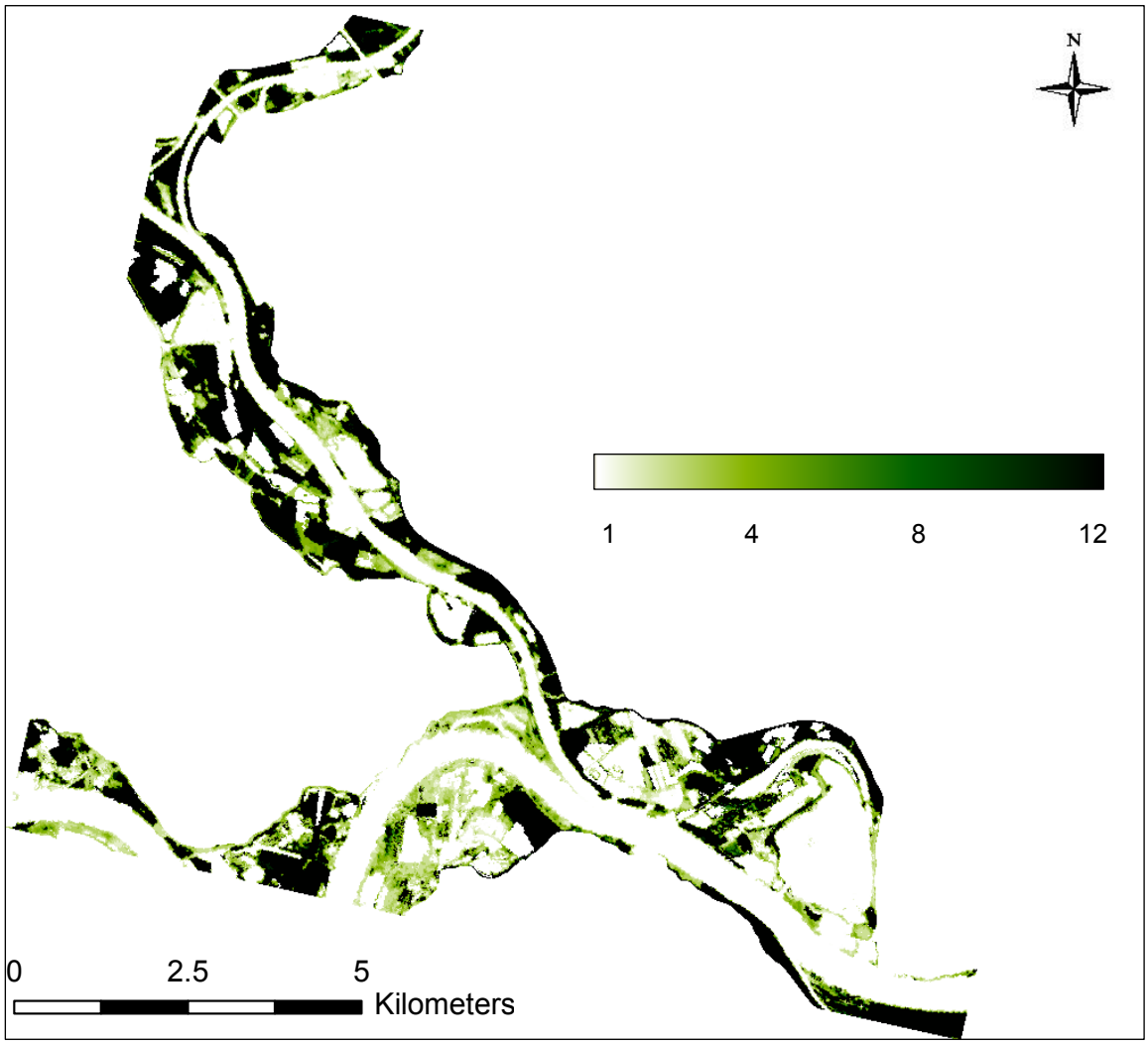

LAI map of the Gelderse Poort for the nadir direction.

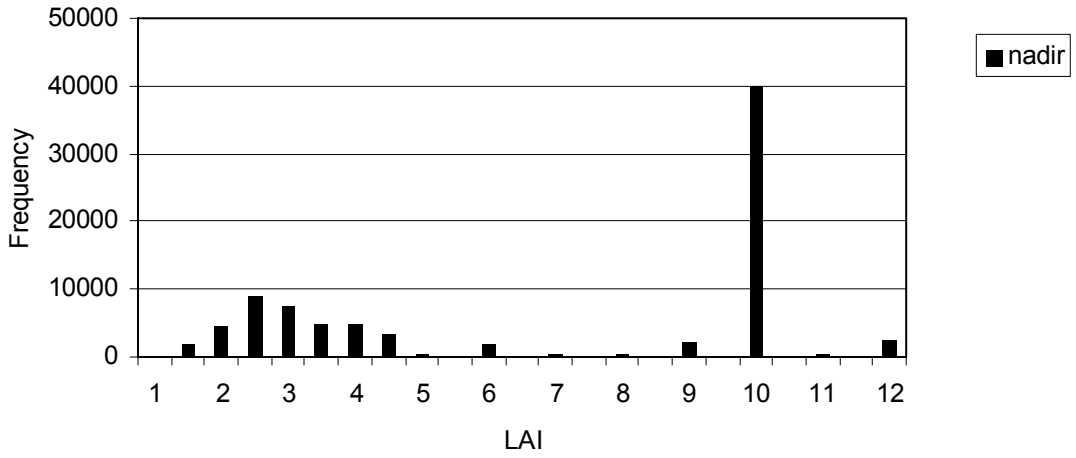

Histogram LAI Gelderse Poort for the nadir direction.

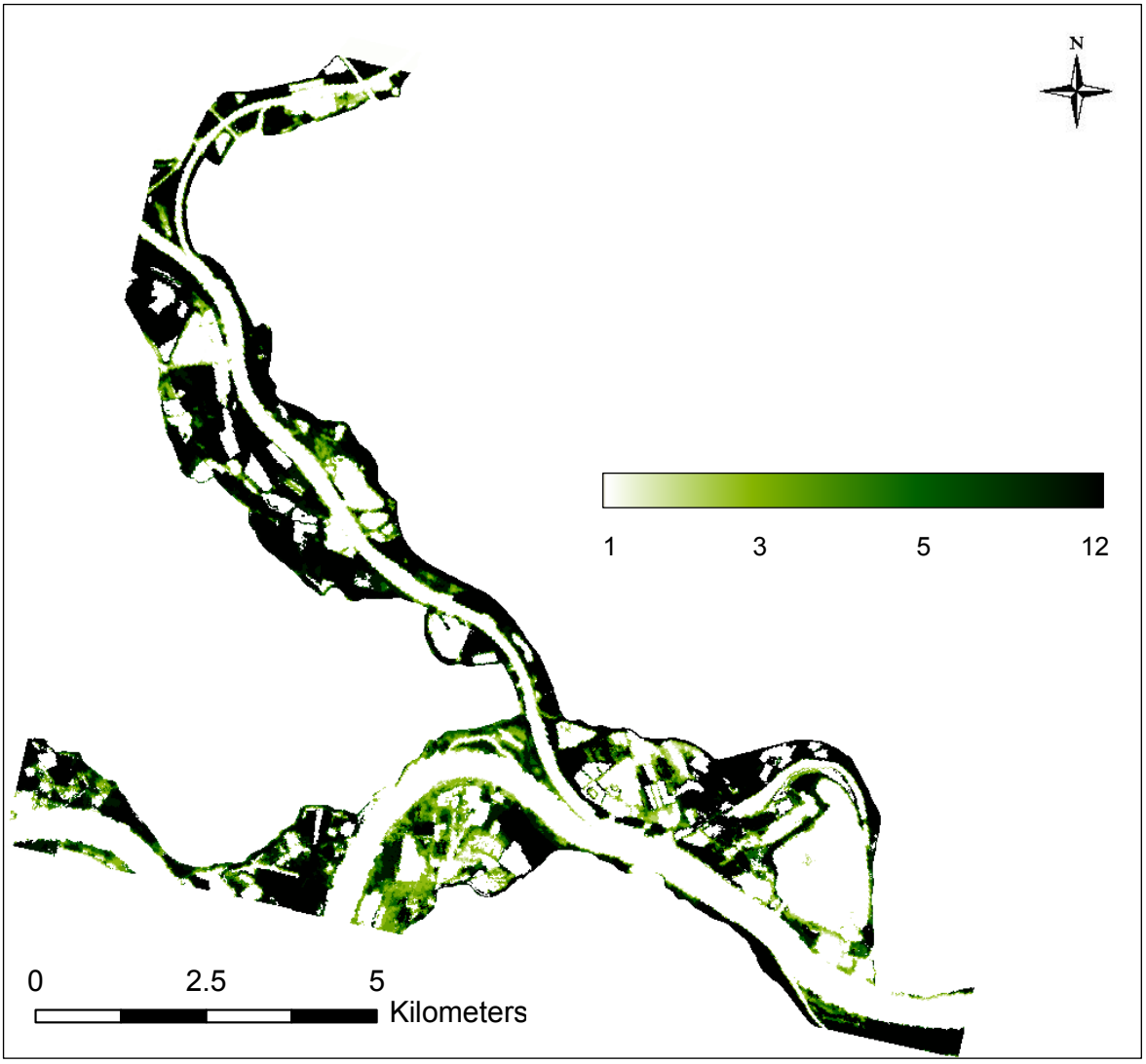

LAI map of the Gelderse Poort for the forward scattering direction.

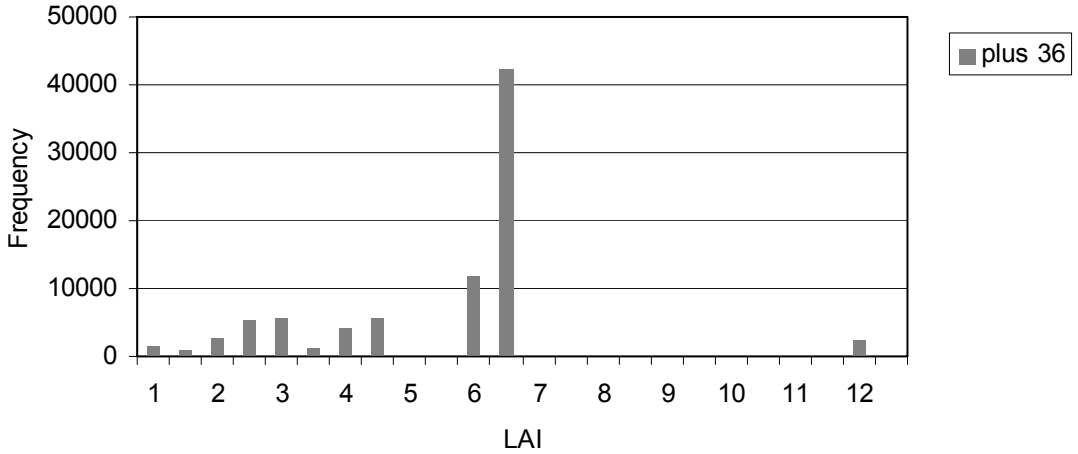

Histogram LAI Gelderse Poort for the forward scattering direction.

Appendix XII: fCover results for the Gelderse Poort in the nadir and forward scattering direction obtained with the model FLIGHT

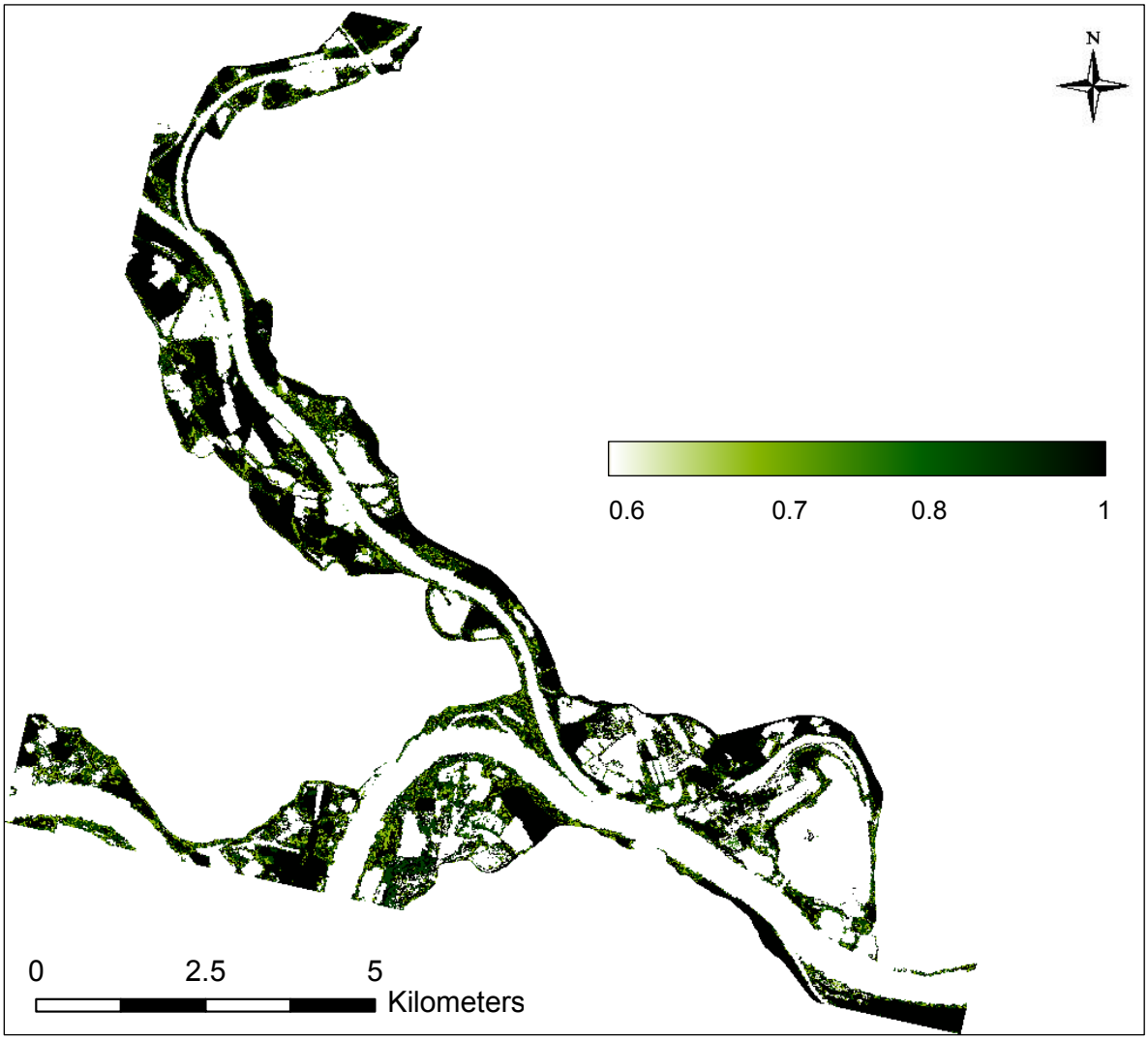

fCover map of the Gelderse Poort for the nadir direction.

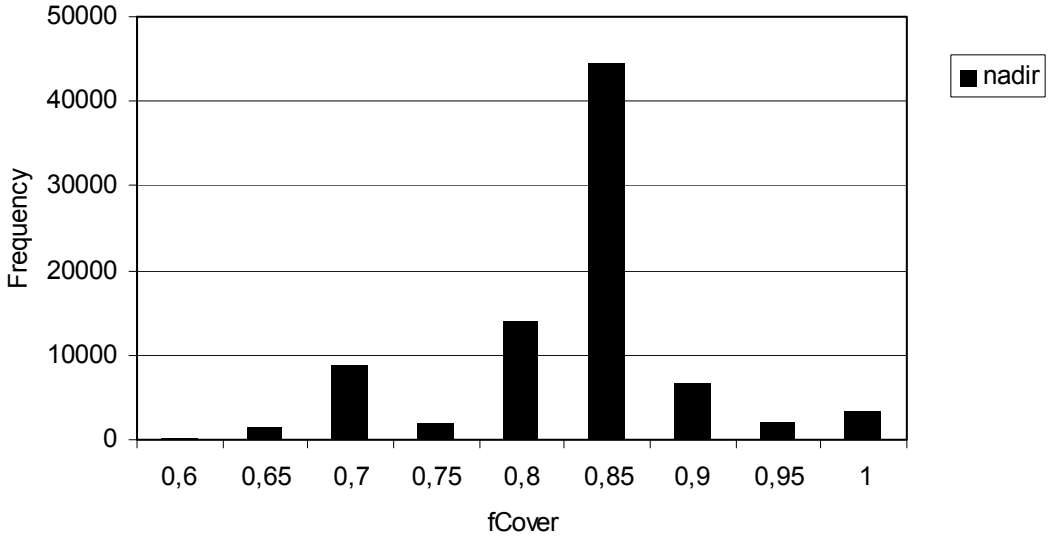

Histogram fCover Gelderse Poort for the nadir direction.

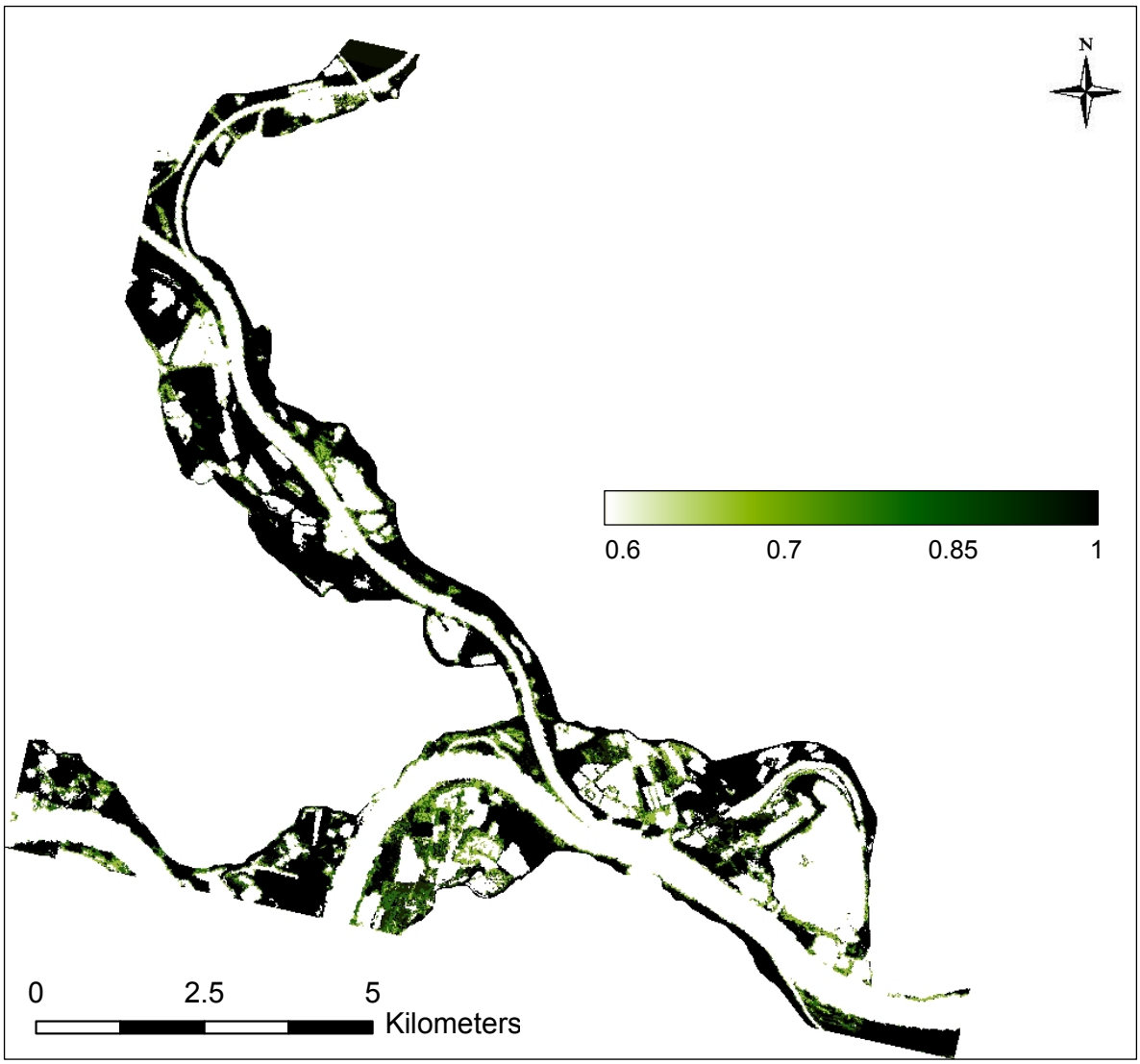

fCover map of the Gelderse Poort for the forward scattering direction.

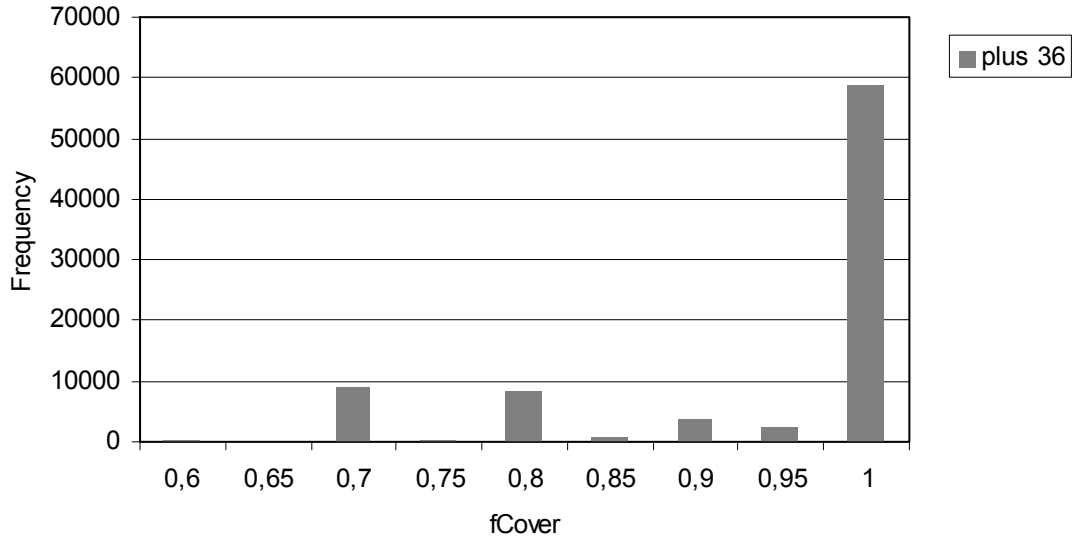

Histogram fCover Gelderse Poort for the forward scattering direction.

Appendix XIII: Scatter plots validation LAI with field data from 2005

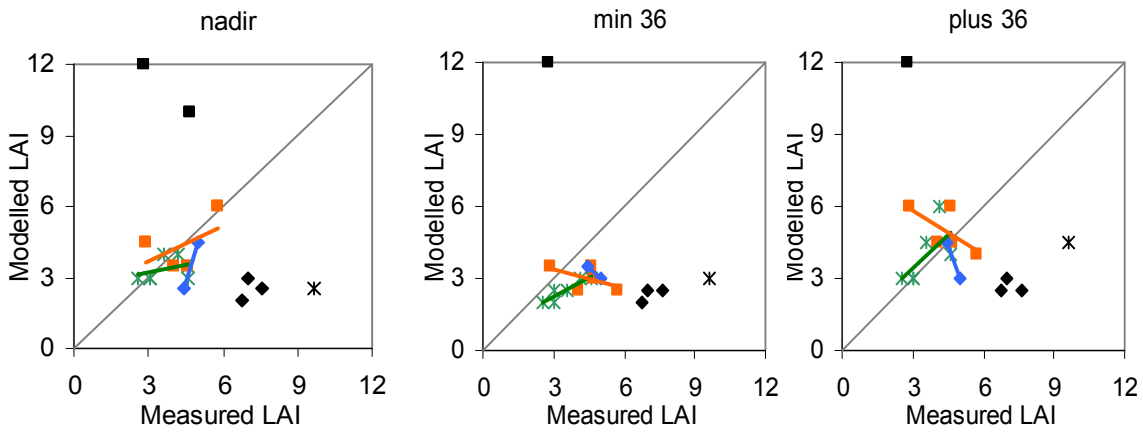

Nadir:
F: y = 3.4483x – 12.845; R^2 = 1
S: y = 0.5049x + 2.1988; R^2 = 0.2635
H: y = 0.2277x + 2.5252; R^2 = 0.1517

Min 36
F: y = -0.8621x + 7.3362; R^2 = 1
S: y = -0.263x + 4.1539; R^2 = 0.3077
H: y = 0.3952x + 1.0556; R^2 = 0.6205

Plus 36
F: y = -2.5862x + 16.009; R^2 = 1
S: y = -0.6012x + 7.6383; R^2 = 0.4595
H: y = 0.9453x + 0.5455; R^2 = 0.4733

herbaceous
outliers herbaceous
shrubs
outliers shrubs
forest
outliers forest
x = y
Lineair (herbaceous)
Lineair (shrubs)
Lineair (forest)

These scatter plots show the correlation between the modelled LAI for the 3 viewing angles and the measured LAI that was obtained with the hemispherical camera + TRAC for 19 validation points in 2005. The results are presented separately for the 3 modelled vegetation structure types. The linear regression functions and R^2 values are written underneath the graphs. F means forest, S means shrubs, H means herbaceous.

Appendix XIV: Scatter plots validation fCover with field data from 2004

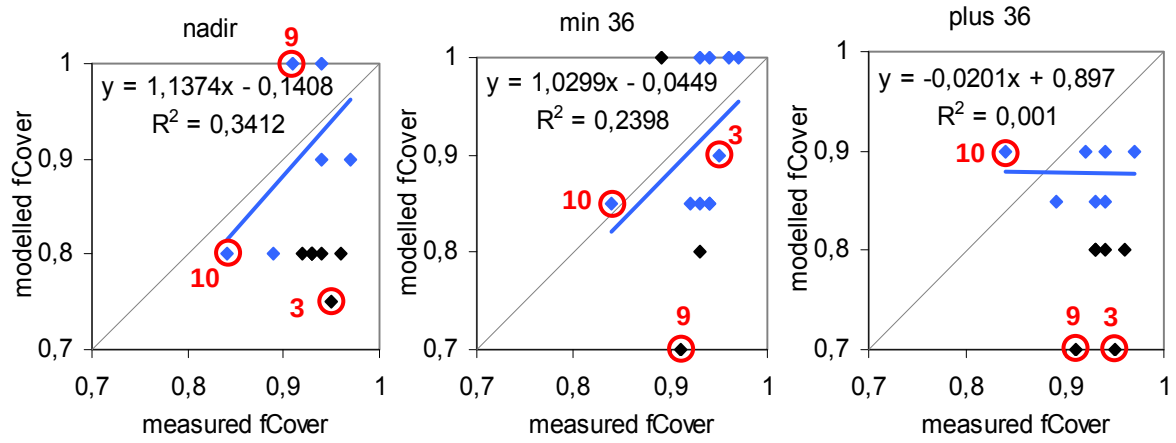

These scatter plots show the correlation between the modelled fCover for the 3 viewing angles and the measured fCover that was obtained with the hemispherical camera for 13 validation points in 2004. The linear regression functions and R^2s are plotted in the graphs.

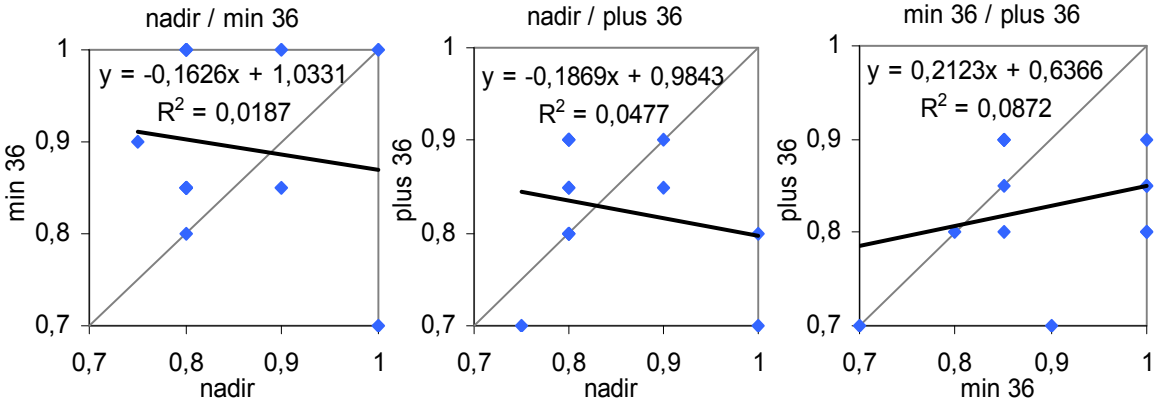

These scatter plots show the cross validation results of the modelled fCover for the 3 viewing angles and the measured fCover that was obtained with the hemispherical camera for 13 validation points in 2004.